

MAIDO MERISALU

Nanostructured Coatings for  
Car and Aerospace Industries





**MAIDO MERISALU**

Nanostructured Coatings for  
Car and Aerospace Industries



UNIVERSITY OF TARTU

Press

The study was carried out in Institute of Chemistry and Institute of Physics, Faculty of Science and Technology, University of Tartu, Estonia.

The dissertation was admitted on November 3rd, 2022, in partial fulfilment of the requirements for the degree of Doctor in Philosophy in materials science, and allowed for defence by the Scientific Council on Materials Science of the Faculty of Science and Technology of the University of Tartu.

Supervisor: Emer. Prof. Väino Sammelselg, Institute of Physics, University of Tartu

Opponents: Dr. Marianna Kemell, Department of Chemistry, University of Helsinki and Dr. Arvo Mere, Department of Materials and Environmental Technology, Tallinn University of Technology

Commencement: December 8th, 2022 at University of Tartu, Tartu, Estonia

This work has been partially supported by the Graduate School of Doctoral Studies in Estonia: “Functional materials and technologies” (project 1.2.0401.09-0079), the Estonian Ministry of Education and Research by granting the projects IUT2–24, TLTFY14054T, PSG448, PRG4, SLTFY16134T and by the EU through the European Regional Development Fund under project TK141 (2014-2020.4.01.15-00). The atomic oxygen testing was performed in the framework of the “Announcement of opportunity for atomic oxygen in the ESTEC Materials and Electrical Components Laboratory/ESA-TECQE-AO-013375),” through a collaboration with Picosun Oy.



European Union  
European Regional  
Development Fund



Investing  
in your future

ISSN 2228-0928 (print)  
ISBN 978-9916-27-082-0 (print)  
ISSN 2806-2574 (pdf)  
ISBN 978-9916-27-083-7 (pdf)

Copyright: Maido Merisalu, 2022

University of Tartu Press  
[www.tyk.ee](http://www.tyk.ee)

# CONTENTS

LIST OF PUBLICATIONS .....	7
ABBREVIATIONS .....	9
1. INTRODUCTION.....	10
2. LITERATURE OVERVIEW .....	12
2.1. Aluminum alloys.....	12
2.2. Corrosion of aluminum alloys .....	13
2.3. Anodizing .....	14
2.4. Atomic layer deposition .....	16
2.5. Methods of corrosion testing .....	18
2.6. Physical characterization techniques.....	21
3. RESEARCH OBJECTIVES AND STATEMENTS .....	25
4. MATERIALS AND METHODS .....	27
4.1. Coating preparation .....	27
4.1.1. Standard pre-treatment .....	27
4.1.2. Electrochemical treatments.....	27
4.1.3. Atomic layer deposition.....	28
4.2. Corrosion testing.....	29
4.2.1. Immersion test.....	29
4.2.2. Salt spray test .....	29
4.2.3. Electrochemical tests.....	29
4.2.4. ATOX test.....	30
4.3. Physical characterization .....	30
5. RESULTS AND DISCUSSION.....	32
5.1. Ultra-Thin Ceramic Coatings.....	32
5.1.1. Properties of films grown by ALD.....	32
5.1.2. Dependence of Corrosion Resistance on Coating Material .....	34
5.1.3. Dependence of Corrosion Resistance on Coating Thickness.....	37
5.1.4. Condition of Al-alloy Surface and the Performance of Coatings.....	38
5.2. Electrochemical surface engineering.....	43
5.2.1. Effect of the LET process on the surface of AA2024-T3 .....	44
5.2.2. Performance of coatings on substrates pre-treated by LET .....	47
5.2.3. Effect of potentiodynamic anodizing on the surface of AA2024-T3.....	50
5.2.4. Sealing and coating of AAO with nanolaminate by ALD .....	51
5.3. Nanostructured Coatings .....	55
5.3.1. Effect of potentiostatic anodizing on AA2024-T3 .....	56
5.3.2. Impregnation of AAO with different materials grown by ALD.....	58

5.3.3. Linear sweep voltammetry study of nanostructured coatings.....	59
5.3.4. Hardness of nanostructured coatings.....	61
5.3.5. EIS study of nanostructured coating.....	63
5.3.6. Salt spray testing of nanostructured coatings.....	65
5.3.7. STEM study of nanostructured coating.....	66
5.3.8. ATOX testing of nanostructured coating.....	68
5.3.9. Radiation behavior of the nanostructured coating.....	70
5.3.10. Practical implementation of nano-coatings.....	71
5.3.11. Optimizing the ALD process for preparing coatings on Al alloys.....	73
5.3.12. Benefits of nanostructured coating in the space industry.....	74
CONCLUSIONS.....	76
SUMMARY IN ESTONIAN.....	79
ACKNOWLEDGEMENTS.....	82
REFERENCES.....	83
PUBLICATIONS.....	89
CURRICULUM VITAE.....	174
ELULOOKIRJELDUS.....	176

## LIST OF PUBLICATIONS

- I. V. Sammelselg, L. Aarik, M. Merisalu, Patent: Method of preparing corrosion resistant coatings. Publication number: WO 2014102758 A1. Priority date: Dec 31, 2012. [WO2014102758A1 - Method of preparing corrosion resistant coatings - Google Patents](#). Other applications: EP, US, JP.
- II. M. Merisalu, L. Aarik, J. Kozlova, H. Mändar, A. Tarre, V. Sammelselg, Effective corrosion protection of aluminum alloy AA2024-T3 with novel thin nanostructured oxide coating. *Surface & Coatings Technology* 411 (2021) 126993. <https://doi.org/10.1016/j.surfcoat.2021.126993>.
- III. M. Merisalu, L. Aarik, J. Kozlova, H. Mändar, A. Tarre, H. M. Piirsoo, V. Sammelselg, Al alloy protection via ultra-thin ceramic coatings and different surface pretreatments. *Surface & Coatings Technology* 435 (2022) 128240. <https://doi.org/10.1016/j.surfcoat.2022.128240>.
- IV. M. Merisalu, L. Aarik, H. M. Piirsoo, J. Kozlova, A. Tarre, R. Zabels, J. Wessing, A. Brieva, V. Sammelselg, Nanostructured Coating for Aluminum Alloys Used in Aerospace Applications. *Journal of the Electrochemical Society* 169 (2022) 071503. <https://iopscience.iop.org/article/10.1149/1945-7111/ac7bb2>.

## AUTHOR'S CONTRIBUTION

The study involves the output of numerous individuals. The reason lies in the complex nature of the coating preparation and characterization, which requires the expertise of scientists from different fields. The results of this study are a group effort and the author's contribution to each paper is given below.

- I. Participation in the preparation of the patent. Designing and carrying out chemical and electrochemical pre-treatments of the Al-alloy samples. Corrosion testing of the coated and uncoated metal substrates. Characterization of studied substrates via photography and optical microscopy. Participation in SEM-FIB-EDX studies.
- II. Preparation of the initial draft of the manuscript. Designing and carrying out chemical and electrochemical pre-treatments of the Al-alloy samples. Corrosion testing of the coated and uncoated metal substrates. Characterization of the studies substrates via photographing, OM, SEM, SEM-FIB and EDX. Participation in STEM and XRD studies.
- III. Preparation of the initial draft of the manuscript. Designing and carrying out chemical and electrochemical pre-treatments of the Al-alloy samples. Corrosion testing of the coated and uncoated metal substrates. Characterization of the studies substrates via photographing, OM, SEM, SEM-FIB and EDX. Participation in nanoindentation, STEM and XRR studies.

IV. Preparation of the initial draft of the manuscript. Designing and carrying out chemical and electrochemical pre-treatments of the Al-alloy samples. Corrosion testing of the coated and uncoated metal substrates. Characterization of the studies substrates via photographing, OM, SEM, SEM-FIB and EDX. Participation in nanoindentation, STEM, XRR and ATOX studies.

#### AUTHOR'S OTHER PUBLICATIONS RELATED TO THE TOPIC

- a) M. Merisalu, T. Kahro, J. Kozlova, A. Niilisk, A. Nikolajev, M. Marandi, A. Floren, H. Alles, V. Sammelselg, Graphene-polypyrrole thin hybrid corrosion resistant coatings for copper. *Synthetic metals* 200 (2015) 16–23.  
<https://doi.org/10.1016/j.synthmet.2014.12.024>.
- b) I. Iakubivskiy, P. Janhunen, J. Praks, V. Allik, K. Bussov, B. Clayhills, J. Dalbins, T. Eenmäe, H. Ehrpais, J. Envall, S. Haslam, E. Ilbis, N. Jovanovic, E. Kilpua, J. Kivastik, J. Laks, P. Laufer, M. Merisalu, M. Meskanen, R. Märk, A. Nath, P. Niemelä, M. Noorma, M. R. Mughal, S. Nyman, M. Pajusalu, M. Palmroth, A. S. Paul, T. Peltola, M. Plans, J. Polkko, Q. S. Islam, A. Reinart, B. Riwanto, V. Sammelselg, J. Sate, I. Sünter, M. Tajmar, E. Tanskanen, H. Teras, P. Toivanen, R. Vainio, M. Väänänen, A. Slavinskis, Coulomb drag propulsion experiments of Estcube-2 and FORESAIL-1. *Acta Astronautica* 177 (2020) 771–783.  
<https://doi.org/10.1016/j.actaastro.2019.11.030>.
- c) J. Dalbins, K. Allaje, I. Iakubivskiy, J. Kivastik, R. O. Komarovskis, M. Plans, I. Sünter, H. Teras, H. Ehrpais, E. Ilbis, M. Noorma, A. Slavinskis, M. Merisalu, P. Janhunen, ESTCube-2: The Experience of Developing a Highly Integrated CubeSat Platform. Conference: 2022 IEEE Aerospace Conference (AERO).  
<http://dx.doi.org/10.1109/AERO53065.2022.9843521>.



## ABBREVIATIONS

Al-alloy / the alloy / Al-Cu alloy	AA2024-T3
ALD	Atomic layer deposition / atomic layer deposited
ATOX	Atomic oxygen
CV	Cyclic voltammetry
$E_{cor}$	Corrosion potential
EDX / EDS	Energy dispersive X-ray spectrometer/spectroscopy
EIS	Electrochemical impedance spectroscopy
$E_{oc}$	Open circuit potential
$E_{pit}$	Pitting potential
FIB	Focused ion beam
HR	High resolution
IMP	Intermetallic particle
$I$	Current (A)
$j$	Current density (A/cm <sup>2</sup> )
$I_{max}$	Current at highest anodic potential (A)
$j_{max}$	Current density at highest anodic potential (A/cm <sup>2</sup> )
Laminate/nanolaminate	A coating prepared by ALD that contains layers of Al <sub>2</sub> O <sub>3</sub> and TiO <sub>2</sub>
LET	Low potential electrochemical treatment
LSV	Linear sweep voltammetry
OM	Optical microscopy / optical microscope
SCE	Saturated calomel electrode
SEM	Scanning electron microscopy / scanning electron microscope
STEM	Scanning transmission electron microscopy / scanning transmission electron microscope
TEM	Transmission electron microscopy / transmission electron microscope
XPS	Photoelectron spectroscopy / -spectrometer
WD-XRF	Wavelength dispersive X-ray fluorescence spectroscopy / -spectrometer
XRR	X-ray reflectometry
NSS	Neutral salt spray test

# 1. INTRODUCTION

Aluminum alloys such as AA2024-T3 in the Al 2000 series are favored for the fabrication of automobile and aircraft components owing to their light weight and superior mechanical properties [1–5]. In terms of corrosion resistance, phase structure, and elemental composition, the aforementioned alloy is comparable to AA2219-T851, which has been utilized in the space industry to fabricate structural components for remotely operated vehicles, satellites, and the International Space Station [6, 7]. In these applications, the use of lightweight materials minimizes fuel consumption as well as energy stored in batteries, which directly increases the vehicle's operating time, reduces greenhouse gas emissions, and minimizes the carbon footprint from the use of fossil-based fuels. The reduction of greenhouse gas emissions is particularly important because it applies to both hydrogen and fossil fuels, both of which contribute to global warming in various ways. Carbon dioxide and water vapor are both potent greenhouse gases produced by the combustion of hydrogen and fossil fuels [8]. Note that the production of hydrogen through electrolysis of seawater using excess energy from other power sources is problematic owing to the deterioration of electrode performance and that the most cost-effective method is currently the steam methane reforming process, which generates significant carbon dioxide emissions [8]. In addition, methane is a potent greenhouse gas that escapes into the atmosphere during the production, processing, and transportation of natural gas [8]. Moreover, the use of aluminum alloys has additional advantages in the space industry. For instance, the low density of aluminum alloys reduces the cost of transporting satellites and other functional components into the orbit [9]. Aluminum alloys are also useful for radiation shielding because their interaction with cosmic radiation results in less harmful secondary electromagnetic radiation compared to materials with a high atomic number [10]. Finally, the superior conductivity of aluminum alloys enables them to be used for thermal regulation and mitigating the surface charging caused by cosmic radiation [11].

Aluminum alloys have a number of advantages over other materials; however, their application environments present numerous challenges [1–5]. For instance, stainless steels such as AISI 316 [5] have good corrosion resistance but a higher density, which limits their use in the construction of vehicles, where low weight is preferred to reduce fuel consumption. In contrast, carbon fiber-reinforced polymers [5] are lightweight but difficult to process, which limits their applications and increases manufacturing costs. Conversely, aluminum alloys are lightweight and easy to process, but are also vulnerable to galvanic corrosion in environments containing humidity, chloride ions, and oxygen [3]. This type of galvanic corrosion is promoted by other passive metals in electrical contact with the primary aluminum alloy component, as well as by various intermetallic particles close to the surface [12–15]. In space, however, the absence of oxygen prevents the formation of an oxide layer on newly exposed aluminum surfaces. This can cause parts that rarely move, such as scanning mechanisms, to become stuck owing to

cold welding, which can be exacerbated by fretting caused by vibrations due to the movement of antennas or during satellite launch [16]. However, at low Earth orbit, the direct flux of atomic oxygen can still cause significant damage to certain materials owing to its high reactivity and impact velocity [17, 18].

The aforementioned disadvantages of aluminum alloys can be overcome by applying functional coatings that are selected based on the component's dimensional tolerance, shape, and application. Currently, the best methods for coating substrates with a sophisticated three-dimensional shape include chemical conversion coatings [7], anodizing [19, 20], plasma electrolytic oxidation (PEO) [16, 21], and atomic layer deposition (ALD) [22–24]. Conversion coatings are the easiest to apply because the substrate only needs to be dipped in the necessary chemical, which converts the alloy's surface into a protective coating [7]. Obviously, the industrial process requires a more intricate line to ensure proper pre-treatment of substrates prior to the process and thorough cleaning of chemicals afterward. In anodizing, the conversion of the metal surface into a porous anodic aluminum oxide (AAO) is performed electrochemically, which allows for greater control over the coating's properties [21, 22]. Notably, the best chemical conversion processes and type 1 anodizing rely on solutions containing hexavalent chromium, which is toxic and carcinogenic, thereby restricting its industrial use in certain regions [25]. Therefore, there is an immediate need for processes that do not require hexavalent chromium compounds (such as **MIL-DTL-5541 Type 2**) [26]. In contrast to anodizing, the PEO process [16, 21] is carried out in alkaline solutions at higher potentials. During PEO, discharges occur at the alloy–electrolyte interface, briefly generating a high-temperature and localized plasma that causes the formed oxide layer to be partially crystalline and, consequently, harder than the AAO obtained by anodizing. ALD can produce the thinnest protective coatings, which typically have a thickness of up to 100 nm. Previous studies have demonstrated that ALD can be used to enhance the corrosion resistance of AA2024-T3 [27, 28], aluminum [29, 30], steel [31–37], copper [38], and silver [39]. Moreover, these studies also demonstrate the advantages of nanolaminates over single-material films. In addition, a comprehensive evaluation of the chemical resistance of various metal oxide films and nanolaminates [40] has been conducted.

In this study, we investigate the performance of coatings grown by ALD on AA2024-T3 as well as the possibility of using anodizing as a pre-treatment prior to ALD to create a new type of nanostructured coatings for industrial applications.

## 2. LITERATURE OVERVIEW

### 2.1. Aluminum alloys

Currently, aluminum alloys are the second most commonly used metals after steel [1–5]. Their applications range from aircraft, drones, spacecraft, and automobile components to electronic device casings. For precipitation hardening, the highly soluble alloying elements Cu, Zn, Mg, and Si are added to Al. On the basis of these alloying elements, aluminum alloys are classified into various series [Table 1].

**Table 1.** Wrought aluminum alloy designations [5]

Designation	1xxx	2xxx	3xxx	4xxx	5xxx	6xxx	7xxx
Major alloying elements (mass%)	None	Cu 0.1 – 6.8	Si 0.08 – 1.8 Mg 0.05 – 1.5 Cu 0.03 – 0.9	Si 0.6 – 21.5	Mg 0.2 – 6.2	Mg 0.2 – 3.0 Si 0.2 – 1.8	Zn 0.8 – 12

The series 2000 aluminum alloy, formerly known as duralumin, contains copper as its predominant constituent. Through the use of appropriate heat treatments, it is possible to give the alloy a strength comparable to that of steel [1–5]. For instance, AA2024-T3 and AISI 316 have ultimate tensile strengths of 448 and 550 MPa, respectively [5]. This allows the incorporation of microscopic intermetallic particles (IMP-s) into the metal during the AA2024-T3 manufacturing process, which is based on the solubility changes of solid materials at different temperatures. To achieve this, the alloy is initially heated above the solvus temperature and soaked there until a homogeneous solid solution is formed. Further, the hot alloy is rapidly cooled to room temperature via quenching, resulting in a supersaturated solid solution. Finally, the alloy is either cold-worked, naturally aged at room temperature, or precipitation-hardened at elevated temperatures. Intermetallic particles formed during this process significantly increase the alloy's hardness by making dislocation movement more difficult.

**Table 2.** AA2024-T3 composition in mass% [5]

Al	Cu	Mg	Mn	Fe	Si	Zn	Cr
Balance	3.8–4.9	1.2–1.8	0.3–0.9	0.5 max	0.5 max	0.25 max	0.1 max

The composition of AA2024-T3, one of the most popular Al-Cu-Mg alloys used in aircraft construction, is shown in Table 2. The AA2024-T3 components are fabricated from a 493 °C solution, annealed at 413 °C, cooled to room temperature, and then artificially aged at 180 °C [1, 5]. Earlier studies of AA2024-T3 have demonstrated that the alloy's microstructure is dominated by microscale

Al<sub>2</sub>CuMg and nanoscale Al<sub>20</sub>Mn<sub>3</sub>Cu<sub>2</sub> particles, as well as a significant amount of other types of IMP-s containing Al, Cu, Fe, and Mn (e.g. Al<sub>7</sub>Cu<sub>2</sub>Fe, Al<sub>3</sub>Fe, and Al<sub>3</sub>Mn) [12]. However, the study of the alloy with high-resolution techniques by Boag et al., also revealed that the intermetallic particles were frequently clustered closely together or fused, rendering them indistinguishable when measured with conventional EDX [12]. Moreover, phases such as Al<sub>2</sub>Cu, Al<sub>10</sub>(Cu,Mg), (Al,Cu)<sub>93</sub>(Fe,Mn)<sub>5</sub>(Mg,Si)<sub>2</sub>, Al<sub>20</sub>(Cu,Fe,Mn)<sub>5</sub>Si(Al<sub>8</sub>Fe<sub>2</sub>Si), Al<sub>3</sub>(Cu,Fe,Mn), and Al<sub>7</sub>Cu<sub>2</sub>Fe were also identified in the study.

## 2.2. Corrosion of aluminum alloys

Corrosion is the process by which the useful properties of a material degrade over time owing to environmental factors [1, 3]. Aluminum is chemically very active. Accordingly, it should have low corrosion resistance. However, exposure to oxygen results in the formation of a thin oxide layer on the metal, which renders it chemically inert in air. In addition, the formed metal oxide film is dense and adherent, preventing further aluminum oxidation by blocking oxygen from reaching the underlying substrate. However, the stability and protective properties of the natural oxide layer depend on the environment's humidity, salinity, and pH as well as the composition of the aluminum alloy. For instance, alloying elements reduce the corrosion resistance of the natural oxide layer, and exposure to water slowly converts the oxide layer into aluminum hydroxide, particularly at high temperatures.

Galvanic coupling, which is caused by electrical contact with a more passive metal or the presence of near-surface intermetallic particles (IMP-s) in an environment containing water, chloride, and dissolved oxygen [12–15], drastically accelerates the corrosion of aluminum alloys. For example, if an aluminum alloy frame is connected with steel bolts, the aluminum frame will experience accelerated corrosion at the interface between the two metals. However, in the case of IMP-s, the corrosion process is more complex, affecting high-strength alloys such as AA2024-T3. In the case of AA2024-T3, various IMP-s (e.g. Al<sub>7</sub>Cu<sub>2</sub>Fe, Al<sub>3</sub>Fe, Al<sub>3</sub>Mn, and Al<sub>20</sub>Mn<sub>3</sub>Cu<sub>2</sub>) are more passive than the surrounding matrix of aluminum, which is largely depleted of alloying elements [12]. The number of alloying elements in the surrounding aluminum matrix is ultimately determined by thermal treatment procedures such as quenching and artificial aging; however, the matrix behaves similarly to pure aluminum in terms of localized galvanic corrosion. In particular, the aforementioned IMP-s become cathodic and accelerate galvanic corrosion of the surrounding anodic aluminum (Fig. 1a). Nonetheless, the most abundant micrometric Al<sub>2</sub>CuMg IMP-s in AA2024-T3 cause pitting in a more complicated manner [13]. As a result of the localized galvanic coupling of cathodic Cu with Mg and Al within the IMP, the IMP undergoes drastic changes in the initial stage. This results in the rapid corrosion of Mg and Al at the IMP (Fig. 1b), which enriches the latter in Cu (Fig. 1c). Consequently, the IMP becomes cathodic, causing galvanic corrosion of the surrounding Al matrix.

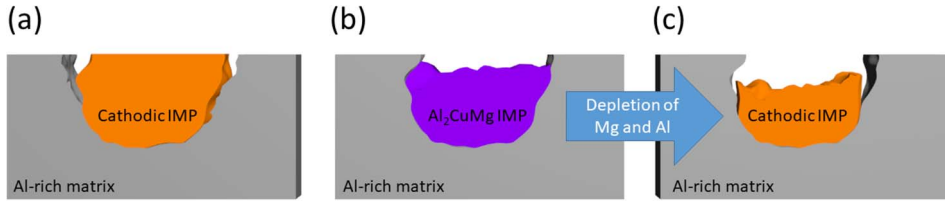


**Fig. 1.** Schematics of pitting corrosion of Al-Cu alloys caused by near-surface IMP-s. Cathodic IMP-s cause the corrosion of the surrounding matrix (a). Al<sub>2</sub>CuMg IMP-s are first depleted of Mg and Al (b), which leads to the enrichment of Cu (c). This causes the site to become cathodic and cause corrosion of the surrounding Al-rich matrix.

### 2.3. Anodizing

Although aluminum alloys have been the primary structural material for commercial and military aircraft for more than 70 years, the majority of the final product consists of the surface finish [1, 3]. Anodizing is one of the most common techniques used to improve the corrosion and wear resistance of alloys [19, 20]. In this electrochemical process, the metal's surface is converted into AAO at the expense of the substrate material (Fig. 2). Fig. 3 depicts a typical anodizing setup, in which the metal substrate serves as the anode and the stainless-steel bath as the cathode. The bath is filled with an appropriate electrolyte (e.g. sulfuric acid), and an optional surrounding bath can be used to maintain the desired temperature. Both electrodes are connected to a direct current power supply, which is used to apply the desired electrical parameters for the anodizing process (e.g., voltage limitation and/or current density). The properties of the resulting AAO layer depend on the electrical parameters, temperature, time, and electrolyte used in the anodizing process. For instance, growing a thicker oxide layer requires increased process time, voltages, and current densities. Utilizing lower electrolyte temperatures during the anodization process permits the production of a denser AAO.

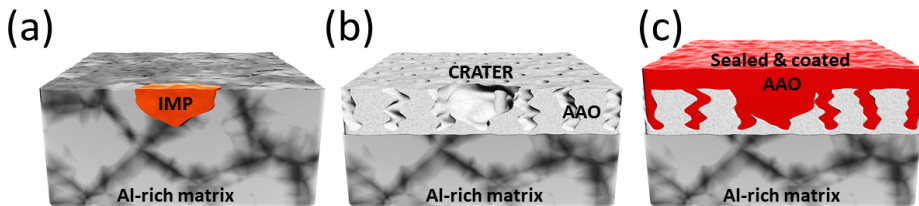


**Fig. 2.** Schematics of a metal substrate's surface before (a) and after anodizing (b). Finally, the pores in the anodic oxide layer are sealed (c) using paint or other methods to enhance the metal's corrosion resistance and/or aesthetic appearance.

Throughout the last century, numerous electrolytes were tested for anodizing; however, only a handful are widely used today, and three of them define distinct anodizing types [20]. Type I anodizing with chromic acid electrolyte has been

utilized for a long time because the obtained anodic oxide layer provides excellent corrosion resistance relative to coating thickness. However, the carcinogenic and toxic nature of chromium (VI) compounds has led to their ban in EU and other industrialized nations [25]. Consequently, alternative anodizing electrolytes, such as sulfuric acid and its mixture with boric acid, have gained popularity. Sulfuric acid is utilized in types II and III anodizing processes, with the primary distinctions between the two types being the anodizing temperature and electrical parameters. Type II anodizing is mostly used for obtaining thinner and porous decorative or protective coatings while type III anodizing is performed at lower temperatures ( $< 10\text{ }^{\circ}\text{C}$ ) and higher current densities, resulting in denser and harder oxide layers as a result of the decreased mean pore diameter. Therefore, these hard coatings are useful in engineering applications such as the automotive and aerospace industries. Given that the obtained AAO is naturally porous, it is primarily necessary to seal the pores to achieve the desired properties in the final product. Various paints and lacquers, for instance, are used to seal the pores in the AAO obtained by type II anodizing, resulting in an aesthetically pleasing appearance and enhanced resistance to wear and corrosion. However, the AAO obtained by anodizing type III can be successfully sealed for certain applications using a hydrothermal treatment in which aluminum oxide is partially converted into aluminum hydroxide [19]. The latter occupies more space than aluminum oxide and therefore seals the nano-scaled pores in the AAO.

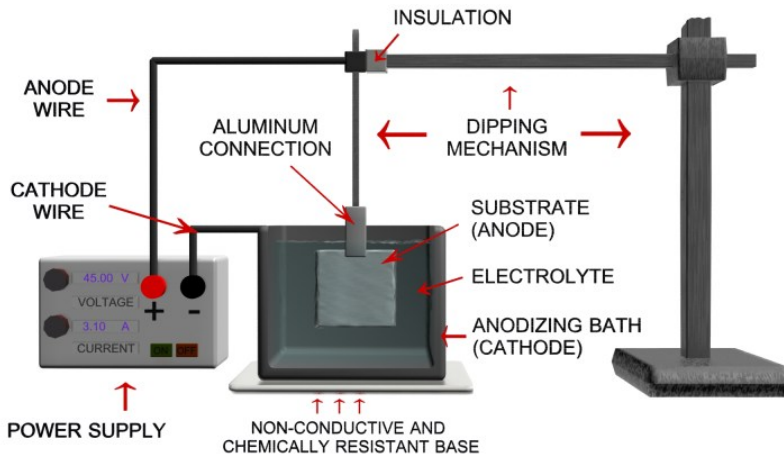


**Fig. 3.** Schematic of a typical 2-electrode system used for anodizing.

## 2.4. Atomic layer deposition

Atomic layer deposition (ALD) is a technique for growing thin films of a variety of materials (precursors) in the gas phase [22–24]. Notably, some precursors are initially in a solid or liquid phase and require additional heating to become gaseous for ALD. Traditionally, the ALD process is carried out in a specially designed ALD reactor and requires at least two distinct precursors, which typically enter the reaction chamber one at a time, along with an inert carrier gas (e.g.  $N_2$ ). In each complete ALD cycle, these precursors react on the substrate surface via self-limiting surface reactions owing to the molecules' adsorption limitation, and form a thin and up-to-the-monomolecular layer of the desired material on the surface. This enables the application of uniformly thick thin films of materials even on substrates with complex three-dimensional shapes, giving ALD a competitive advantage over alternative coating preparation techniques. The thickness of the grown material is determined by the number of ALD cycles, while its crystallinity is determined by the temperature of the substrate. Using lower temperatures results in amorphous films while higher temperatures can be used to achieve different crystal phase structures. For example,  $TiO_2$  produced by ALD can be amorphous, anatase, or rutile, depending on the deposition temperatures [23, 24]. Fig. 4 depicts a typical ALD cycle for the deposition of  $TiO_2$ , in which two liquid precursors ( $TiCl_4$  and  $H_2O$ ) and four sub-cycles are utilized:

1.  $TiCl_4$  vapors enter the chamber and react with the  $OH^-$  groups adsorbing on the substrate's surface prior to their entry.
2. The chamber is purged with a carrier gas ( $N_2$ ) to remove excess  $TiCl_4$  and  $HCl$  byproducts of the gas phase reaction.
3.  $H_2O$  vapors enter the chamber and react with the previously  $TiCl_4$ -modified substrate surface. Consequently, a thin layer of solid  $TiO_2$  and the gas phase reaction by-product  $HCl$  is produced.
4. A carrier gas is used to purge the chamber of excess  $H_2O$  and  $HCl$ .

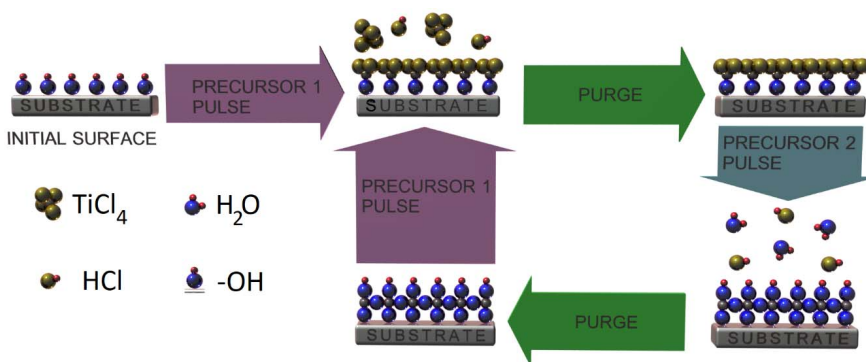


**Fig. 4.** Schematics of the atomic layer deposition of  $TiO_2$  from  $TiCl_4$  (precursor 1) and  $H_2O$  (precursor 2).



The ability to use ALD for the preparation of thin chemically inert films on even arbitrarily shaped objects makes the technique appropriate for the fabrication of ultrathin corrosion protection coatings on precision components [27–40]. Matero et al., [31] studied the behavior of  $\text{Al}_2\text{O}_3$ ,  $\text{TiO}_2$ ,  $\text{Al}_2\text{O}_3/\text{TiO}_2$  nanolaminate, and  $\text{Ta}_2\text{O}_5$  films in 1999, when they first investigated the concept of utilizing ALD to create corrosion-resistant coatings. The slow dissolution of the  $\text{Al}_2\text{O}_3$  films in an aqueous NaCl solution could account for the initial high resistivity of the  $\text{Al}_2\text{O}_3$  films during immersion corrosion testing, which decreased over the course of a few weeks. Conversely,  $\text{TiO}_2$  films were found to be chemically resistant, as it took 80%  $\text{H}_2\text{SO}_4$  at 110 °C and a 2 nm/h etching rate to remove the films from a glass substrate. However, it was also discovered that  $\text{TiO}_2$  films cannot provide adequate corrosion protection owing to the low quality of films grown at low temperatures (e.g., 150 °C) or the crystallinity of films made at 200 °C or higher, which introduces grain boundaries that act as weak sites in the coating. The  $\text{Al}_2\text{O}_3/\text{TiO}_2$  nanolaminate examined in this study combined the diffusion barrier effectiveness of  $\text{Al}_2\text{O}_3$  with the chemical resistance of  $\text{TiO}_2$ . This resulted in a coating that performed well in corrosion tests, as 12 weeks of immersion in an aqueous NaCl solution revealed no signs of corrosion. In addition, the number of nanolaminate layers did not significantly affect the Bode plot of electrochemical impedance spectroscopy (EIS) studies. The use of ALD for preparing protective coatings on AA2024-T3 was later investigated [27, 28]. Potts et al., [28] demonstrated with 10–50 nm  $\text{Al}_2\text{O}_3$  films grown by ALD that thicker coatings and the use of plasma ALD rather than thermal ALD can provide superior corrosion protection. Moreover, Marin et al., [27] discussed the behavior of nanolaminates on AA2024-T3, demonstrating that the use of nanolaminates can reduce the current densities measured during a polarization scan in a linear sweep voltammetry (LSV) test by multiple orders of magnitude. At potentials slightly more anodic than the corrosion potential, however, the current density increased drastically. This demonstrates that the best nanolaminates on their own can significantly improve the corrosion resistance of Al alloys, but cannot provide complete protection. Marin et al., also demonstrated a novel method for preparing ALD-based coatings by combining it with other techniques in the same study [27]. In particular, the combination of sol-gel coatings with a top layer of  $\text{Al}_2\text{O}_3$  applied by ALD produced a hybrid coating that is significantly more corrosion-resistant than either of these coatings individually. Marin et al., also studied a hybrid coating in which the first layer was created by physical vapor deposition (PVD) and the top layer by atomic layer deposition (ALD) [33, 41]. In this case, the function of ALD is to fill nanometric defects in the first hard layer produced by PVD, which significantly improves the corrosion resistance of the coatings.

## 2.5. Methods of corrosion testing

The objective of corrosion testing is to predict the real-world performance of materials and protective coatings. Product development frequently necessitates corrosion testing to determine the most cost-effective means of mitigating corrosion over a specified period of time. Overall, the corrosion tests can be categorized as a) laboratory tests, b) piloting or prototyping tests, and c) field tests [42]. In the development of novel coatings and materials, laboratory tests are of utmost importance because they enable rapid evaluation of the performance of tested substrates and adjustment of the preparation parameters (Fig. 5). These laboratory tests are frequently conducted under conditions that are harsher than the actual application environment in terms of temperature, humidity, salinity, and other properties. This allows the corrosion process to be accelerated, thereby reducing the overall testing duration and cost. The greatest risk associated with laboratory tests is that accelerating the corrosion process can produce results that are too different from the actual application. This can be mitigated by conducting a series of corrosion tests that allow for the investigation of various aspects of corrosion. The immersion (Fig. 5a), neutral salt spray (NSS) (Fig. 5b), various electrochemical (Fig. 5c), and atomic oxygen (ATOX) tests are among the most important laboratory tests (Fig. 5d). Before and after the test, the tested substrates are also characterized by weighing, photographing, and using cutting-edge physical characterization techniques such as scanning electron microscopy.

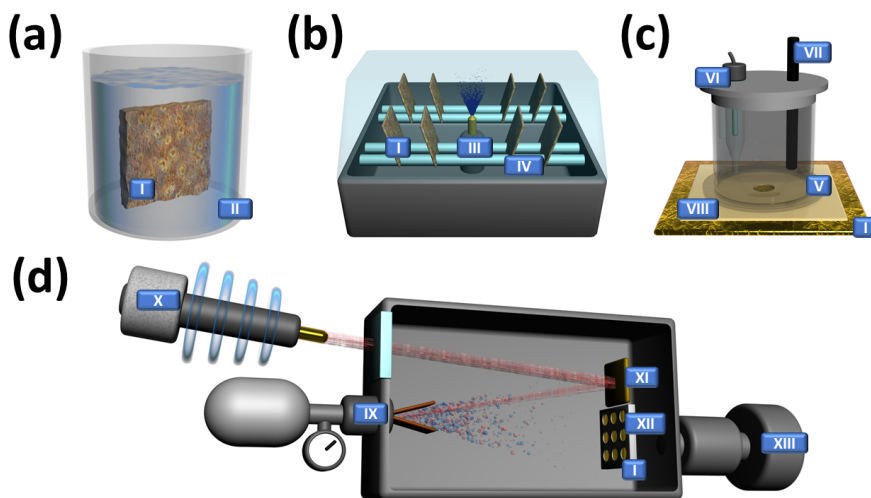


**Fig. 5.** Illustration of setups used for various corrosion tests: immersion (a), salt spray (b), electrochemical (c), and ATOX (d) tests.

**Immersion tests** (Fig. 5a) are conducted by completely or partially immersing the tested substrate (Fig. 5a, I) in a solution (Fig. 5a, II) that simulates some of the conditions of the actual application environment. Additionally, the substrate

can be immersed and dried multiple times to achieve more realistic results. In these tests, room-temperature liquids ranging from distilled water, synthetic saliva, and seawater to harsh chemicals that can be alkaline, acidic, or oxidizing in nature are typically used. Immersion tests are widely used owing to their simplicity, low cost, and the ability to obtain reliable results in a matter of months.

**Salt spray tests** (Fig. 5b) are conducted in a special cabinet with a protective coating for inner walls, filled with a saltwater fog, and maintained at a high temperature (Fig. 5b, III). In this test, the tested substrates (Fig. 5b, I) are placed on specially designed racks (Fig. 5b, IV). The conventional neutral salt spray test (EVS-EN ISO 9227), for instance, is conducted with a 5% NaCl solution at 35 °C and pH of 6.5–7.2 for 8–3000 h. Salt spray testing is favored by industries for product or material specifications, as well as for research and development or quality control, due to the ability to precisely control the testing conditions. In comparison to immersion tests, salt spray tests are more expensive due to the need for a stationary system that requires significant laboratory space, electricity, and a prepared salt solution for long-term operation. Frequently, salt spray tests are also performed with other solutions that are more corrosive (e.g., by lowering the pH to 3.1–3.3 by adding acetic acid), which allows for reduction of the test time and evaluation of the performance of materials and coatings that are normally resistant to corrosion under ambient conditions.

**Atomic oxygen tests** are used to simulate the conditions of low Earth orbit by exposing the tested substrate to a flux of atomic oxygen in a specially designed facility [43]. These tests utilize a higher flux of atomic oxygen than in space, which allows for a significant acceleration of the corrosion testing process and the simulation of years of exposure to the actual application environment at a reasonable cost and timeframe. In order to produce atomic oxygen, the testing chamber (Fig. 5d) employs an oxygen source (Fig. 5d, IX) that is irradiated with a CO<sub>2</sub> laser beam (Fig. 5d, X). Using mirrors (Fig. 5d, XI) and internal chamber design features, the flux of atomic oxygen can be directed towards the samples (Fig. 5d, I), which are held in a specially designed holder (Fig. 5d, XII). The testing system also includes a vacuum pump and a residual gas analyzer (Fig. 5d, XIII), allowing for the monitoring of the timing of atomic oxygen pulses and the composition of extracted gases. When atomic oxygen reacts with the tested substrates, the latter can be utilized to obtain additional information regarding the gas phase corrosion products that may be produced.

**Electrochemical tests** are the quickest way to determine the corrosion behavior of materials and coatings, making them ideal for screening a large number of candidates for a specific application. The electrochemical corrosion tests are conducted in a cell filled with a corrosive electrolyte and constructed specifically for the purpose (Fig. 5c). This cell consists of a chemically inert casing, reference [e.g. saturated calomel electrode (SCE)], counter (graphite rod or Pt wire), and working electrodes, which is the substrate being studied. The electrochemical experiments are controlled by a potentiostat, which is connected to the three electrodes. To achieve reproducible and comparable results, the working electrode's

surface area must be constant. In some setups, this is accomplished with electrochemical masks (e.g., dielectric adhesive tape with a 1 cm<sup>2</sup> opening), which are most suitable for flat and smooth substrates.

Potential measurement, polarization scans such as linear sweep voltammetry (Fig. 6a), and electrochemical impedance spectroscopy are some of the most common electrochemical tests (Fig. 6b, c). The measurement of potential against the reference electrode is particularly useful for comparing different conductive materials to determine if their combination could result in galvanic corrosion. In synthetic seawater, for instance, a potential difference greater than 0.2 V is considered hazardous. Linear sweep voltammetry can provide additional information about the corrosion behavior of materials and protective coatings. In this method, an electrical potential ( $E_{\text{start}}$ ) was applied to the investigated substrate and subsequently changed over time at a predetermined rate until a limiting value is reached ( $E_{\text{end}}$ , end potential). During the potential scan, the current density is measured to characterize the processes occurring at the electrode-electrolyte interface. Higher measured current densities at anodic potentials indicate the presence of corrosion processes in corrosion studies, which focus on the reactions that occur on the metal substrate. In the case of coated substrates, a drastic increase in measured current densities can be caused by the formation of a pinhole where the coating has failed and the electrolyte is in contact with the metal substrate. If such a potential can be identified, it can be referred to as the pitting potential ( $E_{\text{pit}}$ ) and used to compare the performance of different coatings; better coatings should have no pitting potential or the pitting potential should be shifted toward high values in the anodic direction. In EIS, a small AC sinusoidal perturbation, such as 10 mV (RMS) in amplitude, is applied to an electrochemical cell and the response AC current signal is measured. In corrosion studies, measurements can be taken over a wide frequency range, which can be utilized to generate a Bode plot (Fig. 6b).

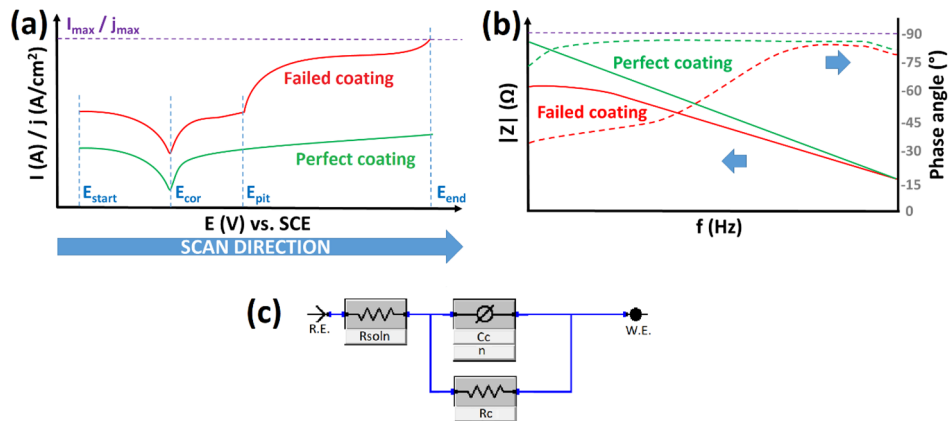


**Fig. 6.** Illustration of a polarization curve obtained by LSV (a), Bode plots obtained by EIS (b), and an ECM used for modeling dielectric coatings (c).

In the Bode plot, a linear impedance behavior over the entire frequency range and a phase angle close to  $-90^\circ$  indicates that the coating is defect-free and no corrosion is occurring. In contrast, a deviation from linear behavior at higher frequencies may indicate the failure of a protective coating. The data obtained from EIS measurements can be interpreted utilizing equivalent circuit models (ECM) such as the one depicted in Fig. 6c. For example, the latter ECM describes the electrolyte resistance ( $R_{\text{soln}}$ ) as well as the coating resistance ( $R_c$ ) and constant phase element (CPE). The CPE considers the coating capacitance and an exponent  $n$ , which is employed in the calculation. This exponent represents the deviation of a capacitor's insulator from ideal dielectric behavior, with  $n = 1$  for an ideal capacitor and  $n = 0$  for an ideal resistor [44].

**Testing in the application environment** provides with the most accurate information on the behavior of materials, protective coatings, and the efficacy of other corrosion mitigation techniques. These tests may be conducted in a number of ways, including atmospheric tests, prototypes, and field tests. In atmospheric tests, samples are placed on specially designed racks or holders and exposed to the environment for the duration of time specified. In terrestrial applications, such tests are frequently conducted near the ocean, where the air contains more chlorides and humidity. Alternately, similar tests have also frequently been conducted on space stations, where samples are placed in a specially designed holder and exposed to corrosive atomic oxygen. The subsequent step is to conduct tests with a physical prototype in which the tested materials are integrated into a highly complex system that operates in the application environment. This makes it possible to study the corrosion of materials under more realistic conditions, where multiple factors can influence the behavior of the tested substrate's deterioration. The field test is a scaled-up version of the prototype testing, in which the tested components are integrated into multiple systems in their actual application. This permits the investigation of the behavior of materials under a broader range of application conditions and the identification of potential issues that were not detectable in previous tests.

## 2.6. Physical characterization techniques

The corrosion behavior of materials and the protective performance of coatings are determined by characterizing the tested substrates prior to and after corrosion tests using various techniques, such as cutting-edge physical characterization methods [45, 46]. First, the substrates are characterized using nondestructive testing techniques and sample preparation procedures. Such techniques typically include weighing, photography, optical microscopy, and infrared spectroscopy. These studies can then be followed by destructive or sample-specific techniques. The techniques described below include scanning electron microscopy (SEM), energy dispersive X-ray microanalysis (EDX), cross-sectioning, and transmission electron microscopy (TEM).

**Scanning electron microscopy (SEM)** uses a beam of accelerated electrons to study the substrate and obtain information on its surface morphology, elemental composition, and elemental distribution. In the microscope, an electron gun is used to emit electrons, which are then accelerated to the appropriate energy (e.g. 1–30 kV) by applying the required voltage, causing the negatively charged electrons to move toward the anode. The operator sets the accelerating voltage based on the purpose of the experiment (e.g. elemental analysis or imaging). The accelerated electrons pass through a system of lenses and scanning mechanisms that manipulate the electron beam using electric and magnetic fields. The electron beam is then directed toward the substrate under study, where the interaction of electrons produces signals such as secondary electrons, backscattered electrons, and characteristic X-rays. The first two signals are used to analyze the surface morphology and compositional variations of the substrate's near-surface region. In contrast, characteristic X-rays are used for elemental analysis. The electron beam itself does not damage metals or protective coatings in terms of destructiveness. For SEM studies, however, the substrates must be clean, dry, and of the proper size, which inevitably introduces a destructive factor into the characterization process. In corrosion studies, the SEM is particularly useful for observing changes in surface morphology owing to its interaction with the environment, which aids in identifying the type of corrosion and employing the most effective corrosion mitigation techniques. The damage caused to materials by atomic oxygen in low Earth orbit, for instance, is initially observable only at high magnifications [18]. In the corrosion studies of AA2024-T3, Boag et al., [13] examined the progression of corrosion using SEM at IMP-s as an example.

**X-ray microanalysis** in SEM utilizes the characteristic X-rays produced by the interaction of accelerated electrons with the studied substrate to examine the elemental composition of the sample in a number of ways. By irradiating a single point with an electron beam, it is possible to measure the elemental composition of a material locally, with the accuracy dependent on the material's thickness and heterogeneity (in the case of thin films, lamellas, or nanostructured materials), the atomic number of the material components, and the energy of the exciting primary electrons. With a conventional energy dispersive X-ray spectrometer, it is also simple to collect the produced characteristic X-rays as the instrument scans across the surface. Using this method, the average elemental composition of a studied material can be determined if it is sufficiently homogeneous. Alternately, the method may be utilized to map the distribution of elements on an imaged area. Some scanning electron microscopes permit the use of this function in real time while examining a sample. To improve the signal-to-noise ratio and contrast of the resulting image, the measurement is performed over a longer time period for publication purposes. In corrosion studies, X-ray microanalysis techniques can be used to detect the presence of corrosion products (such as oxidized metal) and map their distribution on a studied surface, providing additional information on the complex corrosion mechanisms.

**Cross-sectioning** a material mechanically or with a focused ion beam (FIB) permits the examination of its interior. Both of these methods are destructive by

definition. For mechanical cross-sectioning, the sample is frequently submerged in epoxy, which provides extra support during the cutting and polishing process. Cross-sectioning with a focused ion beam requires the integration of an ion gun into an advanced scanning electron microscope. Prior to FIB milling, a mask is frequently applied to the surface of the substrate to protect the delicate surface features during the cross-sectioning and polishing processes; this is yet another irreversible sample modification procedure. Such a mask can be a thin layer of metal or carbon, which is applied via magnetron sputtering or evaporation prior to the SEM-FIB process or by the localized deposition within the microscope if it has the required subsystems and software. For the deposition of Pt in a SEM system, vapors of a compound (such as a metal-organic compound of Pt) are injected close to the surface of the substrate via a thin syringe needle. Simultaneously, an electron beam followed by an ion beam is used to irradiate the vapors at the site of interest, resulting in the decomposition of the compound and the deposition of a metal (e.g., Pt) on the treated area. This permits the creation of microscopic layers of masks within the SEM-FIB system on the substrate. Cross-sectioning can be utilized in corrosion research to examine the progression of corrosion within a material as well as the alteration of the thickness and internal structure of functional coatings.

**Transmission electron microscopy (TEM)** uses accelerated electrons to study a thin layer of material to gain information on its internal microscopic structure and elemental composition [46]. Comparable to SEM, the top of a TEM contains an electron gun, an anode, lenses, and a scanning mechanism. This is followed by a substrate holder and a set of additional lenses for focusing the image on the screen. It is possible to achieve atomic resolution in both imaging and analysis with the best analytical transmission electron microscopes. A lamella is created using a dual-beam SEM-FIB system before a nanocoating can be examined with TEM. Modern lamella preparation entails a) selecting a site with SEM, b) depositing protective masks (e.g. Pt), c) cutting out the lamella with FIB, d) extracting the lamella with a high-precision probe, e) attaching the lamella to a TEM holder, and f) polishing the lamella to reduce its thickness and ensure a high-quality region for TEM studies. Classical lamella preparation, which involves a) physically cutting out a slice of the material, b) milling it mechanically as thin as possible, and c) utilizing a final treatment of chemical etching or ion milling to render the lamella transparent to electrons, is still widely used. For the study of thin protective coatings, FIB is preferred because it permits the production of high-quality lamellas with an intact coating substrate interface. The preparation of lamellas with FIB is also relatively quick, and a negligible amount of the substrate is lost in the process. Inside a material, variations in density or the presence of cavities can be visualized using both bright-field and dark-field imaging. In bright field imaging, only electrons that pass directly through the investigated substrate are detected. In contrast, dark field imaging detects only electrons that scatter at a greater angle after passing through the substrate. Analytical TEM systems can also be used in a scanning mode in conjunction with EDX, in which a finely focused electron beam is used to scan across the area of

the studied sample. Owing to the nanometric thickness of the lamella, it is possible to perform elemental analysis with high precision. This is because the interaction volume between electrons and the substrate is very small. Consequently, the distribution of elements in a studied area can be mapped with nearly atomic resolution, which is especially useful for distinguishing fine interfaces and transitions in materials and coatings. Some scanning transmission electron microscopes are also outfitted with an annual dark field detector, which enables a more efficient collection of scattered electrons, as well as the acquisition of bright field scanning transmission electron microscope (STEM) images and elemental analysis via EDX. If the microscope is equipped with a transmitted electron energy loss spectrometer, it is also possible to analyze low atomic number elements as well as their chemical state with sub-nanometric localization [46].

**Nanoindentation** enables the study of the mechanical properties of a material by poking it with a probe with a sharp and shaped tip [47]. In nanoindentation studies, the probe is pressed into the substrate with a defined force, causing the substrate to deform and the probe to penetrate the material to a particular depth. The shape of the damage caused by indentation and the probe's penetration depth at specific loads can then be used to determine the mechanical properties of a material. The continuous stiffness measurement (CSM) technique can be used to investigate the hardness and Young's modulus of a material [48]. In this method, a sinusoidal component is added to the load, with the oscillating component being approximately one order of magnitude smaller than the maximum load applied. The roughness of a material, which has an effect on the probe-surface interface area and consequently influences the calculated hardness and Young's modulus values, is typically the most significant obstacle when using nanoindentation to study real substrates. This issue can be mitigated in part by collecting more data points through measurements [49].



### 3. RESEARCH OBJECTIVES AND STATEMENTS

This study's primary objective was to investigate the feasibility of enhancing the corrosion resistance of aluminum alloys with thin ceramic coatings that have minimal effect on the total weight and dimensions of the coated substrate. Moreover, it is desired that these coatings can be applied to substrates with complex three-dimensional shapes, such as pores and cavities with internal surface features. Atomic layer deposition (ALD), which has been used in the past to apply thin (10–400 nm) chemically resistant films to substrates to improve their corrosion resistance, may be used to create such coatings. However, the performance of ALD-based coatings is limited, primarily owing to residual porosity, poor adhesion, or limited mechanical durability. In contrast, anodizing can be used to transform the top layer of an aluminum alloy into aluminum oxide, which is then sealed to increase its corrosion and wear resistance. This method is suitable for preparing coatings ranging in thickness from tens of micrometers to a few millimeters; however, its application to aluminum alloys with a high copper content is problematic.

To achieve the research objective, the behavior of thin ceramic coatings produced by ALD on AA2024-T3 aluminum alloy was extensively studied, which is particularly susceptible to corrosion owing to intermetallic particles near the surface. Additionally, the feasibility of using ALD to seal anodized substrates with a novel micrometric nanostructured coating that could be used in industrial applications was investigated.

The following statements are presented for the defense:

1. ALD coatings can increase the corrosion resistance of AA 2024-T3; however, the protective performance of the coatings is dependent on the coating's composition, thickness, and surface condition of the substrate. In the latter instance, near-surface micrometric copper-rich intermetallic particles (such as  $\text{Al}_2\text{CuMg}$ ) are critical as these sites are susceptible to localized galvanic corrosion.
2. Potentiodynamic electrochemical pre-treatment of AA 2024-T3 can be utilized to remove near-surface copper-rich intermetallic particles and tune the thickness of the created AAO layer, thereby enhancing the overall performance of coatings grown by ALD. By using low potentials for electrochemical treatment, which primarily removes near-surface intermetallic particles without forming a thick AAO layer, the thinnest coating is possible with this method. Using higher potentials in the potentiodynamic pre-treatment process generates a sub-micrometric or micrometric AAO layer that can be sealed and coated by ALD to produce a new type of nanostructured coating with superior corrosion resistance.

3. A simple potentiostatic electrochemical pre-treatment can be used before ALD to create a nanostructured coating for industrial applications. In the ALD process, the corrosion resistance, electrical conductivity, and hardness of the nanostructured coating can be modified by depositing suitable materials into the pores of the AAO and on its surface.
4.  $\text{Al}_2\text{O}_3/\text{TiO}_2$  nanolaminate can be used to protect materials from energetic atomic oxygen-induced corrosion.

## 4. MATERIALS AND METHODS

### 4.1. Coating preparation

#### 4.1.1. Standard pre-treatment

The studies were conducted using aluminum alloy AA2024-T3 alclad plates (GoodFellow) with dimensions  $20 \times 20 \text{ mm}^2$  (small) and  $40 \times 110 \text{ mm}^2$  (large). Using machine milling, the Al cladding was mechanically removed from the original 3 mm sheet, resulting in a final thickness of  $2.6 \pm 0.2 \text{ mm}$ . The standard composition of the alloy [5] is listed in Table 2. Prior to experiments, the plates were polished with abrasive paper to achieve a surface finish that was repeatable (P240,  $\text{Al}_2\text{O}_3$  grains, Mirka). To study the scalability of the technology for the preparation of nanostructured coatings for industrial applications on arbitrarily shaped high-precision components, Al alloy substrates were prepared for satellites ESTCube-2 and WISA Woodsat. On the former satellite, an Al-Mg alloy plate containing 2.9% Mg was machine-milled into a cover panel. The components for WISA Woodsat were 3D printed utilizing an industrial metal 3D printer (M290, EOS GmbH) and EOS Aluminum AlSi10Mg (EOS GmbH). Prior to coating, all loose particles and organic contamination were removed using a standard pre-treatment, which consisted of first rinsing with deionized water and then applying three solvents in an ultrasonic bath: 3 min in toluene (purity 99.5%, Reahim), 3 min in acetone (purity 99.5%, Sigma-Aldrich), and 3 min in isopropanol (purity 99.5%, Sigma-Aldrich). To remove impurities and near-surface metal oxides, the 3D-printed substrates underwent an additional chemical treatment involving a) immersion in 10% NaOH solution (purity 98%–100%, Sigma-Aldrich) for 1 min, b) rinsing with deionized water, c) immersion in concentrated  $\text{HNO}_3$  (purity 65%, Sigma-Aldrich) for 1 min, and d) rinsing with deionized water. The latter treatment was required because mechanical polishing was inapplicable to these high-precision components.

#### 4.1.2. Electrochemical treatments

The potentiodynamic electrochemical treatment of small substrates was performed in accordance with our patent [50] using a three-electrode potentiostat Reference 600 (Gamry). The effect of the potentiodynamic electrochemical treatments on the Al alloy and on the performance of coatings made by ALD is discussed in more detail in studies I [51] and II [52]. The substrates were anodized using a PS 8360-10 DT 1 kW (Elektro-Automatik GmbH) DC power supply in a two-electrode setup. The electrolytes used for anodizing at room temperature ( $22 \pm 2 \text{ }^\circ\text{C}$ ) were 15% (w/v)  $\text{H}_2\text{SO}_4$  (Honeywell, Fluka 95–97%), denoted as SA, and a mixture of 5% (w/v)  $\text{H}_2\text{SO}_4$  and 1% (w/v)  $\text{H}_3\text{BO}_3$  (Honeywell, Fluka 99.5%), denoted as BSA. The total surface area, including both sides and all edges of the substrate as well as the section of the Al alloy contact wire that was in contact with the electrolyte during the anodizing process, was approximately 10 and

100 cm<sup>2</sup> for the small and large substrates, respectively. Using a three-electrode system for the electrochemical treatment of the small substrates enabled us to gain additional insight into the process, including the elimination of IMP-s and the formation of the AAO layer.

The low potential electrochemical treatment (LET) process described in study II [52] was carried out by cycling the potential 15 times between 0 and 0.5 V at a scan rate of 1 mV/s. The substrates were then ultrasonically treated for 15 min in a fresh 15% H<sub>2</sub>SO<sub>4</sub> solution. The substrates were then rinsed with deionized water and sonicated in deionized water for an additional 15 min. Finally, the samples were then dried using airflow.

In study I [51], the potentiodynamic anodizing procedure was performed in two steps by cycling the potential between 0 and 2 V five times at a scan rate of 10 mV/s. The potential was then cycled 50 times between 0 and 10 V vs. SCE at a scan rate of 300 mV/s. Unless otherwise specified, all potential values in this study are provided relative to the SCE potential. Large substrates were anodized in a two-electrode setup under conditions comparable to those used for small substrates.

For potentiostatic anodizing of smaller and larger substrates in study III [53], a two-electrode setup with a stainless-steel bath as the cathode and alloy substrates as the anode that were connected to a power supply PS 8360-10 DT 1kw was utilized (Elektro-Automatik GmbH). SA was the anodizing electrolyte, which was maintained at  $1 \pm 0.5$  °C by surrounding the anodizing bath in stainless steel with an external ice bath. Additionally, potentiostatic anodizing at a limiting current density of 12.5 mA/cm<sup>2</sup> was performed at 10 or 20 V for 30 min to produce oxide films of varying thicknesses.

### 4.1.3. Atomic layer deposition

Al<sub>2</sub>O<sub>3</sub>, TiO<sub>2</sub>, Al<sub>2</sub>O<sub>3</sub>-TiO<sub>2</sub> mixture, and Al<sub>2</sub>O<sub>3</sub>/TiO<sub>2</sub> nanolaminate coatings were deposited at 125 °C in a low-pressure flow-type reactor [54] and an industrial ALD reactor R200 (Picosun Oy) [55] on small and large Al alloy substrates with different pre-treatments. Si substrates were added to each ALD process in order to conduct comparative research. For the deposition of the oxides, water was used as the oxygen source, in addition to Al(CH<sub>3</sub>)<sub>3</sub> (TMA; purity 98%, Strem Chemicals) and TiCl<sub>4</sub> (purity 99.9%, Aldrich) as the metal precursors. The target thicknesses of the deposited materials for systematic studies were predominantly 50 nm. For nanolaminate coatings, a series of thicknesses of 50, 100, 110, 250, and 500 nm were prepared. The bottom layer of the nanolaminate consisted of 20 nm Al<sub>2</sub>O<sub>3</sub>, followed by 10 nm TiO<sub>2</sub> and 10 nm Al<sub>2</sub>O<sub>3</sub> layers until the desired thickness was achieved. The TiO<sub>2</sub>-Al<sub>2</sub>O<sub>3</sub> mixture with a thickness of 50 nm was grown using 250 ALD supercycles. Each succeeding supercycle included one complete ALD cycle for the deposition of an Al<sub>2</sub>O<sub>3</sub> sublayer and two complete ALD cycles for the deposition of a TiO<sub>2</sub> sublayer. This was done to compensate for titania's slower growth rate per full growth cycle compared to the growth rate of alumina [56].

## 4.2. Corrosion testing

The corrosion behavior of coated and uncoated Al alloy substrates was studied using immersion, neutral salt spray testing, linear sweep voltammetry, electrochemical impedance spectroscopy, and exposure to atomic oxygen.

### 4.2.1. Immersion test

During systematic studies, immersion tests were conducted in a 0.5 M NaCl (prepared from NaCl, Sigma Aldrich; purity 99.5%) aqueous solution for the majority of smaller substrates and one larger substrate. These experiments were conducted in laboratory glass bottles with airtight seals. The duration of immersion tests in systematic studies with small substrates was 1000 h. The immersion test for the large substrate with nanostructured coating lasted 7152 h (298 days). The substrates were photographed before, during, and after the experiments.

### 4.2.2. Salt spray test

Neutral salt spray tests were performed up to 1000 h at 35 °C according to EVS-EN ISO 9227:2012 at  $35 \pm 2$  °C using a 5 g/l NaCl (SaliCORR® Sodium Chloride) solution having pH of 6.5–7.2 in a commercial testing chamber ClimaCORR CC 400-FL AKES (VLM). The substrates were photographed before and after the experiments. After the tests, the substrates were also rinsed with deionized water prior to photographing to remove salt from the surface of the samples.

### 4.2.3. Electrochemical tests

LSV and EIS corrosion testing was conducted in a naturally aerated 0.5 M NaCl solution (prepared from NaCl, Sigma Aldrich; purity 99.5%), using a potentiostat Reference 600 (Gamry). In the 3-electrode setup, a PTC1™ Paint Test Cell (Gamry), a saturated calomel reference electrode (Gamry), and a Pt wire were utilized. The sample served as the working electrode in these tests. The reproducible sample surface area of 1 cm<sup>2</sup>, exposed to the electrolyte, was achieved with 1 cm<sup>2</sup> (PortHoles™) Electrochemical Sample Masks (Gamry). Prior to electrochemical testing, the samples were stabilized in the electrolyte for 30 min. In LSV tests, the potential sweep began at non-destructive cathodic potentials of –1 V vs. SCE, where neither corrosion nor water electrolysis occurred, and moved at a scan rate of 1 mV/s towards anodic potentials. In systematic studies, 1 or 2 V was used as the final potential. The end potential was set to 10 V, and the scan rate was set to 300 mV/s for testing some of the best-performing coatings. The EIS measurements were performed twice during 24 h immersion in 0.5 M NaCl at open circuit potential (OCP). The first measurement was taken at the beginning

of immersion after the sample had stabilized for 30 min (designated as “0h”) and the second measurement was taken after 24 h (designated as “24h”) of immersion. The measurements were done in the frequency range of  $10^{-2} - 10^6$  Hz with an AC perturbation amplitude of 10 mV (RMS). Using the equivalent circuit models depicted in Fig. 6c, the Echem Analyst™ (Gamry) software was used to interpret the EIS data.

#### 4.2.4. ATOX test

To evaluate the performance of the nanostructured coating in space, the coated substrate was exposed to a flux of atomic oxygen at a facility in low Earth orbit (LEOX) [43], using a setup similar to that depicted in Fig. 5d. In the experiment, the atomic oxygen flux was  $2.7 \times 10^{21}$  atoms/cm<sup>2</sup>, which is equivalent to 1 year of exposure to a direct flux of atomic oxygen in low Earth orbit at an altitude of 400 km, the same as for the International Space Station.

### 4.3. Physical characterization

Initial surface characterization was accomplished by taking photographs at varying magnifications with a smartphone (S8+, Samsung) and an optical microscope Eclipse LV150 (Nikon). Utilizing a dual beam scanning electron microscope Helios Nanolab™ 600 (FEI) for high resolution imaging and energy dispersive X-ray microanalysis, additional surface characterization was performed. The FIB on that microscope was used for making cross-sections and for the preparation of lamellas for transmission electron microscopy/scanning transmission electron microscopy (TEM/STEM) studies. The X-ray microanalysis was performed with EDX analyzer INCA Energy 350 (Oxford Instruments), which was installed onto the aforementioned scanning electron microscope. HR-SEM surface and cross-sectional analyses were performed at a 10 kV accelerating voltage for the primary electrons. For the SEM-EDX studies, an accelerating voltage of 5–30 kV was used. TEM/STEM studies of prepared coatings were conducted with a probe-corrected analytical transmission electron microscope Titan 200 (FEI) that was equipped with a ChemiSTEM 4 SuperX SDD EDX system (FEI/Bruker). This STEM-EDX system enabled the generation of high-resolution high-angle annular dark-field (HAADF) images and element maps by employing primary electrons with energies up to 200 keV. The quality of the Al alloy AA2024-T3 used in this study was determined by wavelength dispersive X-ray fluorescence spectroscopy (WD-XRF), using an AZX 400 WDXRF spectrometer (Rigaku) and X-ray diffraction analysis (XRD), using an X-ray diffractometer SmartLab™ (Rigaku) in symmetrical  $\theta$ - $2\theta$  Bragg-Brentano geometry. The diffractometer uses Cu K <sub>$\alpha$</sub>  radiation from a rotating anode generator working at 45 kV and 180 mA. The same diffractometer was also used to measure X-ray reflection (XRR) in order to determine the density and thickness of the atomic layer deposited films on Si

substrates. The thickness and density of films were refined by the program GlobalFit (Rigaku<sup>TM</sup>). The hardness (H) and Young's modulus (E) were studied by nanoindentation. The coated and bare Si substrates were investigated utilizing a Hysitron TI 980 nanoindenter (Bruker) in a continuous stiffness measurement mode. A maximum load of 1 mN was applied with a Berkovich tip and the average hardness and Young's modulus values were obtained as the mean of 15 individual measurements made in different locations on the sample surface and calculated for the indentation depth of 20 nm, which is the reference depth. The bare and coated Al alloy substrates were studied at the Institute of Solid-State Physics, University of Latvia, with a Nano Indenter G200 (Agilent Technologies) in the continuous stiffness measurement mode. The plots were generated by averaging the results of 20 nanoindentation tests conducted on each sample. Hardness and Young's modulus values were determined at their maximum values in the corresponding plots.

## 5. RESULTS AND DISCUSSION

The development of a thin ceramic coating for the corrosion protection of aluminum alloys was the subject of systematic research. These studies were initially conducted in studies I [51] and II [52] using AA 2024-T3 substrates that were only cleaned and polished prior to ALD coating with various coating types. To enhance the performance of the coatings, potentiodynamic pre-treatment at higher and lower potentials was investigated in studies I [51] and II [52], respectively. Finally, a potentiostatic pre-treatment was investigated in study III [53] to facilitate industrial applications of the process.

### 5.1. Ultra-Thin Ceramic Coatings

The performance of ALD coatings is dependent on the a) properties of the grown films, b) coating material, c) coating thickness, and d) substrate surface condition prior to coating, as shown in studies I [51] and II [52]. The findings of these studies are discussed in detail below.

#### 5.1.1. Properties of films grown by ALD

Table 3 summarizes the XRD, WD-XRF, and XRR data obtained in paper II [52] for  $\text{TiO}_2$ ,  $\text{Al}_2\text{O}_3$ ,  $\text{Al}_2\text{O}_3$ - $\text{TiO}_2$  mixture, and  $\text{Al}_2\text{O}_3/\text{TiO}_2$  nanolaminate films grown by ALD on Si substrates. According to XRD studies, all of the previously mentioned films grown on Si substrates were amorphous. This was anticipated, given that the coatings were grown at 125 °C. WD-XRF analyses of the grown films revealed that both  $\text{TiO}_2$  and the  $\text{Al}_2\text{O}_3$ - $\text{TiO}_2$  mixture contained Cl, with the highest concentration ( $3.7 \pm 0.2$  mass%) found in the mixture film. Notably, the Cl content of the mixture film was also greater than that of  $\text{TiO}_2$  ( $2.8 \pm 0.2$  mass%). The Cl originated from the precursor  $\text{TiCl}_4$  used in the low-temperature ALD process to produce  $\text{TiO}_2$  [57, 58]. The measured thickness of the films,  $d$ , was close to the desired thickness of 50 nm. Accordingly, the density values,  $\rho$ , measured by XRR were  $3.0 \text{ g/cm}^3$  for  $\text{Al}_2\text{O}_3$ ,  $3.7 \text{ g/cm}^3$  for  $\text{TiO}_2$ , and  $3.2 \text{ g/cm}^3$  for the  $\text{Al}_2\text{O}_3$ - $\text{TiO}_2$  mixture. Additionally, the layer density of  $\text{Al}_2\text{O}_3$  and  $\text{TiO}_2$  in the nanolaminate was comparable to that of single-layer films.



**Table 3.** Data obtained by XRD, XRR, nanoindentation, and WD-XRF for TiO<sub>2</sub>, Al<sub>2</sub>O<sub>3</sub>, Al<sub>2</sub>O<sub>3</sub>-TiO<sub>2</sub> mixture, and Al<sub>2</sub>O<sub>3</sub>/TiO<sub>2</sub> nanolaminate films grown by ALD on Si substrates [52].

Film prepared by ALD	Crystalline structure	Elemental composition* in mass%, ( $\pm 0.1$ mass% for Al, Ti and O, $\pm 0.2$ mass% for Cl)				$d$ , nm ( $\pm 1$ )	$\rho$ , g/cm <sup>3</sup> ( $\pm 0.1$ )	$H^{**}$ , GPa ( $\pm 0.4$ )	$E^{***}$ , GPa ( $\pm 1$ )
		Al	Ti	O	Cl				
Al <sub>2</sub> O <sub>3</sub>	Amorphous	52.8	0.0	47.1	0.0	49	3.0	9.2	148
TiO <sub>2</sub>	Amorphous	0.0	63.3	33.9	2.8	56	3.7	7.7	136
Al <sub>2</sub> O <sub>3</sub> -TiO <sub>2</sub> mixture	Amorphous	20.3	38.9	37.1	3.7	52	3.2	8.4	140
Layer 1 – Al <sub>2</sub> O <sub>3</sub>	Amorphous					22	2.9		
Layer 2 – TiO <sub>2</sub>						12	3.7		
Layer 3 – Al <sub>2</sub> O <sub>3</sub>						11	2.9		
Layer 4 (top) – TiO <sub>2</sub>						12	3.6		
Al <sub>2</sub> O <sub>3</sub> /TiO <sub>2</sub> laminate in sum						57	–		

\* Measured by XRF using the thin film program and known composition, density and structure of the films as well as the substrate;

\*\* Hardness of the Si substrate is 12.8 GPa;

\*\*\* Young's modulus of the Si substrate is 146 GPa.

The results of nanoindentation studies are depicted in Fig. 7 and Table 3, where the hardness and Young's modulus of the coatings are calculated as the mean values of 15 individual measurements at 20 nm displacement positions in different locations of the samples. The coatings with the highest hardness and Young's modulus values were Al<sub>2</sub>O<sub>3</sub> and nanolaminate, which behaved similarly. In contrast, the TiO<sub>2</sub> film had the lowest values for hardness and Young's modulus. Finally, the nanolaminate exhibited significantly higher hardness and Young's modulus values than the Al<sub>2</sub>O<sub>3</sub>-TiO<sub>2</sub> mixture film, which was unexpected given that both films contained the same elements. This demonstrates that the mechanical properties of multi-component nanometric films also depend significantly on their internal structure. In nanoindentation studies, coatings were applied to Si substrates, which have a higher hardness (12.8 GPa) than every ALD-grown film studied. This is significant because the studied films had a target thickness of ~50 nm, and the values were obtained at a displacement position of 20 nm, which is significantly higher than the recommended indentation depth of 10% of the coating. Therefore, the Si substrate had an effect on the measured hardness and Young's modulus values. However, the results can still be used to describe the tendencies of the mechanical characteristics of the coating series.

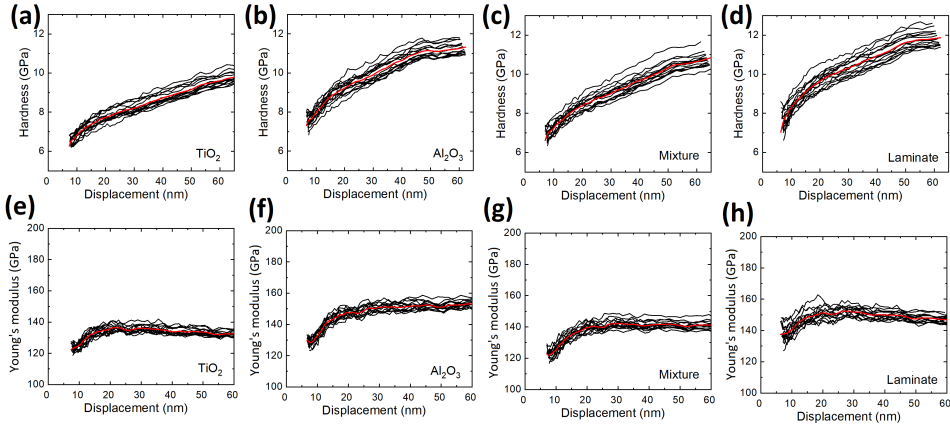


**Fig. 7.** Nanoindentation curves of hardness (a–d) and Young’s modulus (e–h) versus the tip displacement in TiO<sub>2</sub> (a,e), Al<sub>2</sub>O<sub>3</sub> (b,f), Al<sub>2</sub>O<sub>3</sub>-TiO<sub>2</sub> mixture (c,g) and Al<sub>2</sub>O<sub>3</sub>/TiO<sub>2</sub> nanolaminate (d,h) coatings deposited onto Si substrates [52].

### 5.1.2. Dependence of Corrosion Resistance on Coating Material

Table 4 is a summary of the data obtained in study II [52] from LSV and EIS experiments conducted on substrates mechanically polished and coated by ALD with various types of ceramic materials. The LSV experiments were utilized to calculate a pitting potential and measure the current density at the beginning and end of the polarization scan. This was also used to calculate the short-period coating efficiency,  $CE$ , using the following equation (Eq. 1):

$$CE = 1 - (j_{1V}/j_{max}), \quad (1).$$

Because all of the coatings were unstable, EIS was only used to determine the impedance at 10 mHz after 30 min and 24 h immersion in saltwater.

**Table 4.** Data obtained via LSV and EIS experiments for the substrates mechanically polished following coating with ALD by TiO<sub>2</sub>, Al<sub>2</sub>O<sub>3</sub>, the Al<sub>2</sub>O<sub>3</sub>-TiO<sub>2</sub> mixture, and the Al<sub>2</sub>O<sub>3</sub>/TiO<sub>2</sub> nanolaminate [52].

Coating	Pitting potential	Current density at -1 V	Current density at 1 V	Impedance at 10 mHz after 30 min	Impedance at 10 mHz after 24 h	Coating efficiency
	$E_{pit}$ (V)	$j_{-1V}$ (A/cm <sup>2</sup> )	$j_{1V}$ (A/cm <sup>2</sup> )	$ Z_1 $ (Ω)	$ Z_2 $ (Ω)	$CE$ (Eq. 1)
no coating	-0.59	$1.0 \times 10^{-5}$	0.196	–	–	–
TiO <sub>2</sub>	-0.57	$3.5 \times 10^{-6}$	0.142	$9.1 \times 10^3$	$8.7 \times 10^4$	0.28
Al <sub>2</sub> O <sub>3</sub>	-0.55	$1.2 \times 10^{-8}$	0.150	$1.0 \times 10^8$	$8.4 \times 10^5$	0.23
Al <sub>2</sub> O <sub>3</sub> -TiO <sub>2</sub> mixture	-0.56	$1.7 \times 10^{-7}$	0.154	$6.8 \times 10^5$	$2.3 \times 10^5$	0.21
Al <sub>2</sub> O <sub>3</sub> /TiO <sub>2</sub> nanolaminate	-0.51	$3.3 \times 10^{-7}$	0.128	$7.2 \times 10^7$	$2.5 \times 10^6$	0.35

In polarization scans and immersion tests, the corrosion resistance of AA2024-T3 was only marginally enhanced by an ALD-applied **TiO<sub>2</sub> coating**. For example, in polarization scans, the measured current values for samples coated with TiO<sub>2</sub> (Fig. 8, curve 2) are lower compared to the uncoated substrate (Fig. 8, curve 1). This indicates that the coating inhibits corrosion processes occurring on the surface of the substrate. However, at anodic potentials greater than the corrosion potential, the current increased rapidly, indicating coating deterioration and increasing metal exposure. In EIS experiments, the TiO<sub>2</sub> coating exhibited the lowest impedance, which increased slightly during the 24h saltwater immersion (Table 4). The lowest impedance can be explained by the semi-conductive nature of amorphous TiO<sub>2</sub>. The increase in impedance during immersion may be owing to corrosion occurring in the saltwater, which covers the surface of the substrate with a thin layer of dielectric corrosion products.

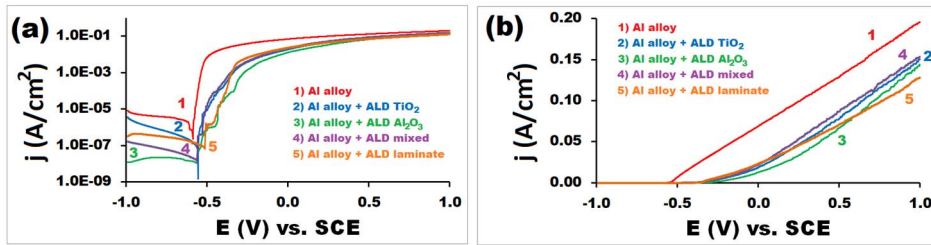


**Fig. 8.** Linear sweep voltammetry corrosion tests for Al alloy substrates that were **polished (1)** and coated by ALD with **TiO<sub>2</sub> (2)**, **Al<sub>2</sub>O<sub>3</sub> (3)**, **Al<sub>2</sub>O<sub>3</sub>/TiO<sub>2</sub> mixture (4)** and **Al<sub>2</sub>O<sub>3</sub>/TiO<sub>2</sub> laminate (5)**. The current value is presented in logarithmic (a) and non-logarithmic (b) scale [52].

At the highest anodic potential of 1 V vs. SCE, however, the measured current value was still significantly less than that of the uncoated substrate (Table 4), indicating that the TiO<sub>2</sub> coating still protected the metal substrate to some degree. The fact that the corrosion potential and pitting potential were in the same region suggests that the coating had weak spots or pathways that allowed corrosive species in the electrolyte to reach the metal substrate.

This claim was also supported by the immersion tests, which revealed that a substantial portion of the coating remained intact after a 1000 h test; however, it contained numerous localized corrosion sites (Fig. 9, b). Furthermore, the results are in good agreement with previous studies, in which it was shown that a TiO<sub>2</sub> coating produced by ALD is chemically resistant but not an effective diffusion barrier [31].

The ALD-applied **Al<sub>2</sub>O<sub>3</sub> coating** on the alloy performed poorly in the immersion test, where the coating was completely destroyed within 1000 h (Fig. 9, c). This is likely due to at least a portion of aluminum oxide being converted into aluminum hydroxide [31]. Similar coating deterioration was observed in the EIS study, where the dielectric coating's impedance decreased after 24 h of immersion in saltwater (Table 4). However, in relatively fast polarization

scans,  $\text{Al}_2\text{O}_3$  exhibited better diffusion barrier properties than  $\text{TiO}_2$  as current values did not increase as rapidly at anodic potentials greater than the corrosion potential (Fig. 8, curves 2, 3). The lack of a well-defined region between corrosion potential and pitting potential indicates the presence of few and/or small pathways in the coating that allow chloride ions to reach the metal. This gradually delaminates the coating at anodic potentials greater than the corrosion potential, resulting in the rapid degradation of the whole coating.

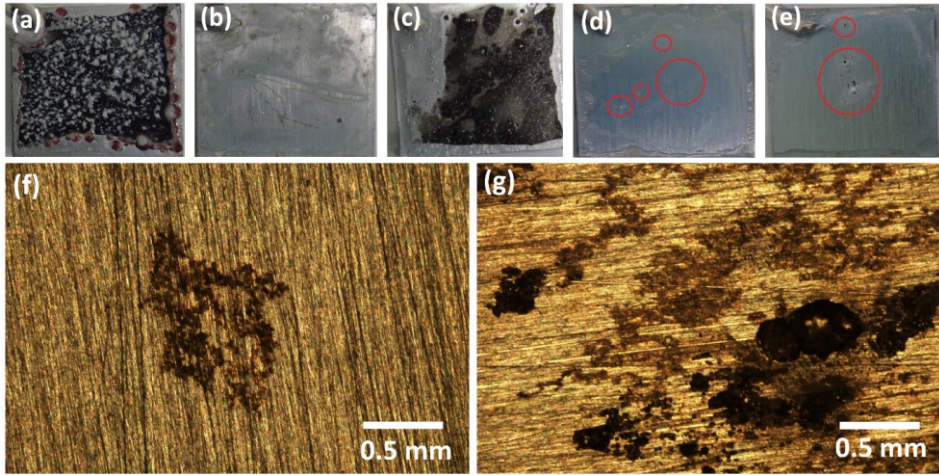


**Fig. 9.** Photographs taken after 1000 h immersion in saltwater of the aluminum alloy substrates that were prior to testing polished (a) and coated by ALD with  $\text{TiO}_2$  (b),  $\text{Al}_2\text{O}_3$  (c),  $\text{Al}_2\text{O}_3$ - $\text{TiO}_2$  mixture (d), and a laminate of  $\text{Al}_2\text{O}_3/\text{TiO}_2$  (e). The sites where mixture (d) and nanolaminate (e) coatings failed are marked with red circles and shown at greater magnification on optical microscopy images f and g, respectively [52].

**$\text{TiO}_2$ - $\text{Al}_2\text{O}_3$  mixture and  $\text{TiO}_2/\text{Al}_2\text{O}_3$  nanolaminate** provided the Al-alloy with the best corrosion resistance of all the coatings tested, with the nanolaminate slightly outperforming the mixture. This is in agreement with previous studies [31, 36, 39] that demonstrate that combining the diffusion barrier properties of dielectric  $\text{Al}_2\text{O}_3$  with the chemical resistance of  $\text{TiO}_2$  results in coatings with superior performance. In any case, it appeared that both laminate and mixture coatings could withstand a 1000 h immersion in saltwater without the  $\text{Al}_2\text{O}_3$  in the coating converting into aluminum hydroxide. Conversely, the difference in their performance could be attributed to individual defects. During the 24-h immersion, the impedance at 10 mHz decreased slightly with both coatings, indicating that corrosion is progressing (Table 4). In immersion tests, the mixture coating based on the photographs (Fig. 9, d, e) appeared to be superior; however, a more detailed microscopy study revealed a large number of microscopic sites where the mixture coating began to degrade (Fig. 9, f). In contrast, the laminate had only a few larger flaws where the coating delaminated gradually (Fig. 9, g). This was in good agreement with the polarization scans depicted in Fig. 8, curve 4, where pitting potential and corrosion potential overlapped in the case of the

mixture coating. This indicated the existence of multiple chloride ion pathways to the metal substrate. However, in the case of the laminate coating, the current did not increase as rapidly at anodic potentials greater than the corrosion potential, indicating that the laminate (Fig. 8, curve 5) had only a few small chloride ion pathways, exhibiting similar behavior to the single layer Al<sub>2</sub>O<sub>3</sub> coating (Fig. 8, curve 3).

### 5.1.3. Dependence of Corrosion Resistance on Coating Thickness

The findings of study I [51] indicate that the thickness of the laminate coating affected its protective properties. As observed from the polarization scans depicted in fig. 10, thicker coatings exhibited lower current values at anodic potentials, similar to the findings published by Díaz, et al., and Marin et al., [35, 36]. The coating with the best performance was the 500 nm laminate (Fig. 10, curve 500), which was distinct from the other coatings.

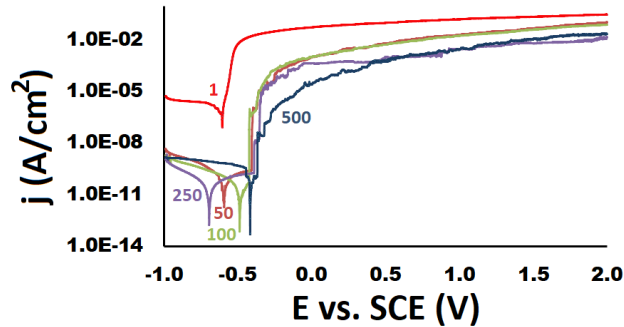


**Fig. 10.** Corrosion testing by linear sweep voltammetry of AA2024-T3 substrates that were polished (1), coated by 50 nm (50), 100 nm (100), 250 nm (250), and 500 nm (500) Al<sub>2</sub>O<sub>3</sub>/TiO<sub>2</sub> laminates. Note that these are deposition target thicknesses based on the estimated growth speed values of Al<sub>2</sub>O<sub>3</sub> and TiO<sub>2</sub> deposited onto Si substrates, and the real thickness of the alloy may differ by up to 30% (in a higher direction) [51].

However, pitting occurred on all coatings between -0.5 and -0.4 V, indicating that even the thickest coatings had initial defects or pathways connecting to the metal substrate, where the laminate began degrading at anodic potentials. This is in contrast to the findings of Marin et al., [36], who found that the use of thicker coatings could significantly shift the pitting potential in the anodic direction. In our case, coating degradation was slowest for 250–500 nm coatings, which can be explained by fewer initial defects/paths and a mechanically more durable layer, which does not peel off as easily as a 50 nm coating when the underlying metal substrate has corroded (Fig. 11). In any case, 250 to 500 nm laminates are too thick to apply by ALD for industrial applications, and the presence of initial defects suggests that merely increasing the thickness of the coating provides AA2024-T3 substrates with only a modest improvement in corrosion resistance.

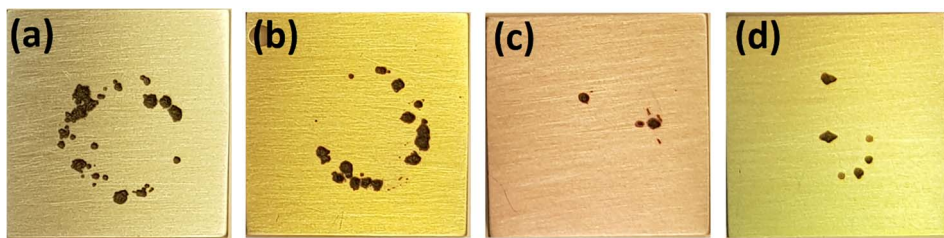


**Fig. 11.** Photos of polished AA2024-T3 plates ( $20 \times 20 \text{ mm}^2$ ) coated by ALD laminate with the thickness of 50 (a), 100 (b), 250 (c), and 500 nm (d), and following tested by linear sweep voltammetry up to +2 V vs. SCE (see Fig. 5b). The circular tested area in the middle of the samples was  $1 \text{ cm}^2$ . Approximately 20% of the coating failed in the testing area on samples with 50 and 100 nm laminates, while on samples with 250 and 500 nm laminates less than 5% of the coating was destroyed [51].

#### 5.1.4. Condition of Al-alloy Surface and the Performance of Coatings

The surface condition of metal substrates influences the performance of ALD-applied coatings in multiple ways. In our early research, we discovered that even a thin layer of contamination can result in localized corrosion. To demonstrate this, we applied a thin layer of graphite with a pencil on the aluminum alloy substrate prior to coating it with  $\text{TiO}_2$  by ALD (Fig. 12). After an LSV test in salt-water, optical microscopy studies revealed the most severe corrosion at contaminated sites (Fig. 12 b, c).

To maximize the performance of coatings, it is crucial that metal substrates be thoroughly cleaned of various contaminants. To achieve this, the substrates were first polished to reduce the number of difficult-to-clean protrusions and cavities.  $\text{Al}_2\text{O}_3$  sandpaper was used to polish the surface to minimize the risk of implanting new materials that a) are not suitable for ALD coating or b) could introduce a galvanic couple with the surrounding surface. Potential  $\text{Al}_2\text{O}_3$  particles from the sandpaper satisfy both criteria because they are dielectric, thereby preventing galvanic coupling. During the ALD process,  $\text{Al}_2\text{O}_3$  particles should behave similarly to the natural aluminum oxide on the metal. After polishing, any potential semi-loose particles were removed by polishing slowly by hand with a heavy-duty plastic mesh scouring pad. Initially, we also attempted to use a rotating plastic brush ( $\sim 600 \text{ rpm}$ ) for final polishing; however, this resulted in brush wear and the introduction of additional surface contaminants. The final cleaning was performed with the standard cleaning procedure using deionized water, toluene, acetone, and isopropanol to remove salts and various organic compounds that could have been introduced during the manufacturing or surface treatment process. In any case, the immersion test results depicted in Fig. 9 confirmed that the surface had been properly cleaned; however, the cause of coating failure at specific locations remained unknown.

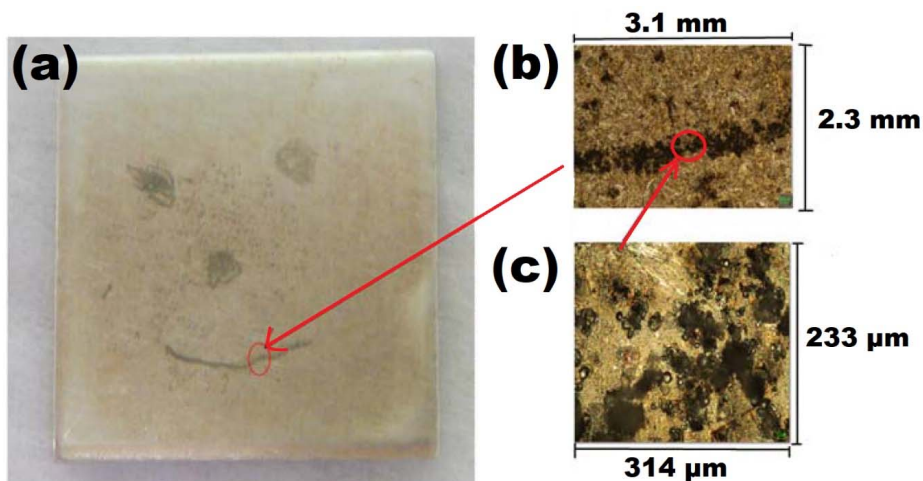


**Fig. 12.** Photo (a) and optical microscopy images (b, c) of a  $20 \times 20$  mm Al alloy substrate that has been contaminated with a graphite pencil prior to coating with  $\text{TiO}_2$  by ALD (a). The photo and microscopy studies were done after a corrosion test by LSV in saltwater, where the potential scan ended at 0.5V.

We hypothesized that the failure of the coating could also be due to the inhomogeneous nature of the Al-alloy, which consists of an Al-rich matrix and intermetallic particles (IMP-s) of varying size, shape, and composition [12]. Specifically, some of these IMP-s would be exposed at the metal's surface, putting ALD-deposited coatings in direct contact with the Al-rich matrix and IMP-s of various compositions. To investigate the effect of IMP-s on the corrosion behavior of coated substrates, an immersion test was conducted with a  $110 \times 40$  mm<sup>2</sup> Al-alloy substrate coated by ALD with an  $\text{Al}_2\text{O}_3/\text{TiO}_2$  laminate (Fig. 13). First sites of corrosion appeared already after 24 h of immersion in 0.5 M NaCl (Fig. 13a). To monitor the progression of corrosion, these locations were subsequently mapped by EDX and photographed by SEM over the subsequent days. The substrates were removed from the immersion solution, rinsed with deionized water, and dried prior to SEM analysis. Subsequently, the substrates were reintroduced to the corrosive medium after SEM analysis. In these studies, we found that the coating failed at an abnormally large cluster of IMP-s, where the damage increased gradually over time. EDX mapping of elements revealed the presence of a larger Cu-Fe-Mn IMP in the center of the coating failure region. In addition, the site appeared to contain less Mg, which is typically present in the largest  $\text{Al}_2\text{CuMg}$  intermetallic particles. We believe that Mg might have been depleted in that site due to rapid localized galvanic corrosion [13–15] when the coating failed. Accordingly, the corrosion products could have dissipated in the solution or been removed by rinsing.  $\text{Mg}(\text{OH})_2$  is slightly soluble in water, and its quantity would have been negligible because it is produced only at the individual near-surface IMP-s where the coating fails. Moreover, the size of the Cu-rich IMP-s in the agglomeration (Fig. 13, center) is comparable to that of the conventional

$\text{Al}_2\text{CuMg}$  IMP-s (Fig 13, bottom right corner). Although we have learned that the failure of an ALD-produced laminate coating is in some way related to IMP-s, we have not yet determined the precise cause of the initial defect that exposed the metal substrate to the corrosive medium.

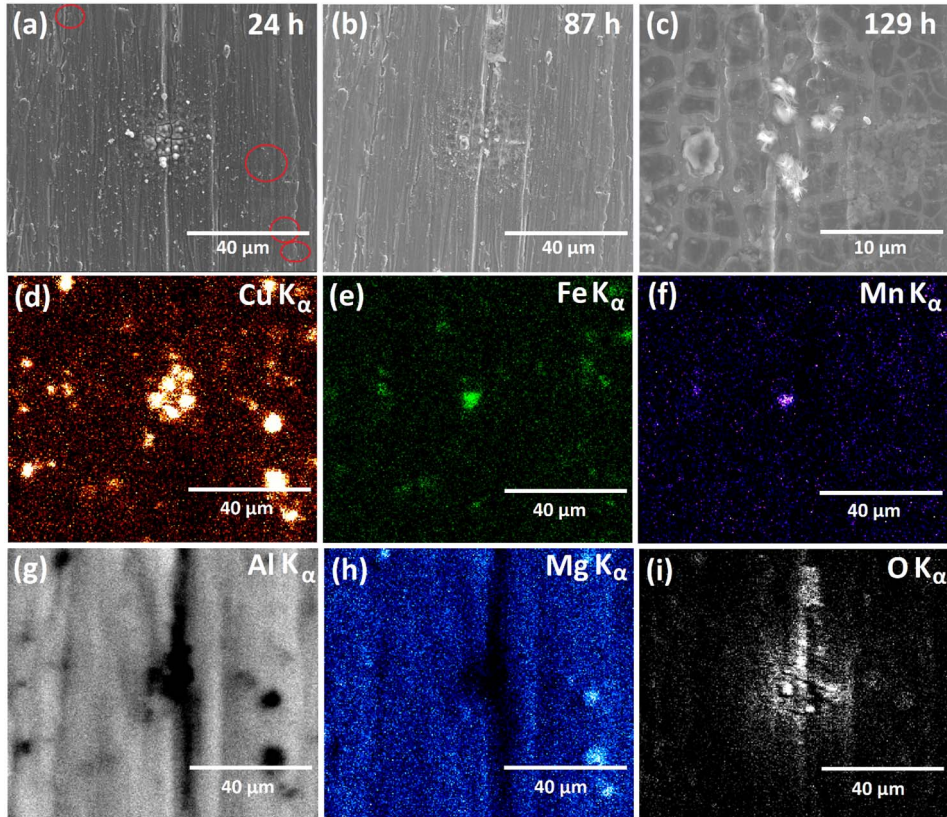


**Fig. 13.** SEM image (a–c) of the evolution of a pit during 24–129 h immersion on a polished Al alloy sample with a 100 nm nanolaminate coating. EDX mappings of the same region after 87 h immersion show the distribution of (d) Cu, (e) Fe, (f) Mn, (g) Al, (h) Mg, and (i) O. Possible near-surface  $\text{Al}_2\text{CuMg}$  IMP-s are marked with circles in the SEM image (a) [51].



To gain a better understanding of the failure of the laminate at IMP-s, we decided to thoroughly examine the coating | metal interface using SEM-FIB and EDX on substrates that had been freshly polished prior to ALD coating and on substrates that had been cleaned and polished in the open air for a couple of weeks prior to ALD coating. As shown in Fig. 14, the Al-alloy is coated by ALD shortly after polishing and cleaning, resulting in a uniform laminate. Surface and cross-sectional analyses confirm that the coating is defect-free and adheres well to the IMP and surrounding matrix.

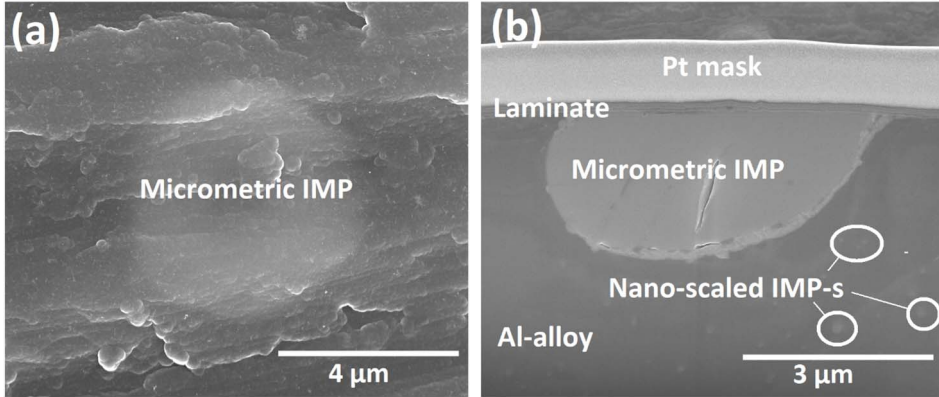


**Fig. 14.** Secondary electron image of the surface (a) and FIB-made cross-section (b) of a region on AA2024-T3 that has an  $\text{Al}_2\text{CuMg}$  IMP which is uniformly coated with the laminate by ALD [52].

In contrast, HR-SEM-FIB and EDX studies revealed that Al-alloy plates stored for a month in open air prior to ALD coating were far more interesting. As shown in Fig. 15, the IMP-s are surrounded by circular features, and the top portion of the IMP has been altered. EDX analyses (Table 5) of the cross-section revealed that the features surrounding the IMP (Fig. 15, site III) are likely to be corrosion products owing to their higher oxygen and chloride content. Moreover, the top part of the IMP (Fig. 15, site IV) also had a higher content of oxygen and chloride in comparison to the bottom part of the IMP (Fig. 15, site II). Furthermore, Cu content was comparable in the upper and lower portions.

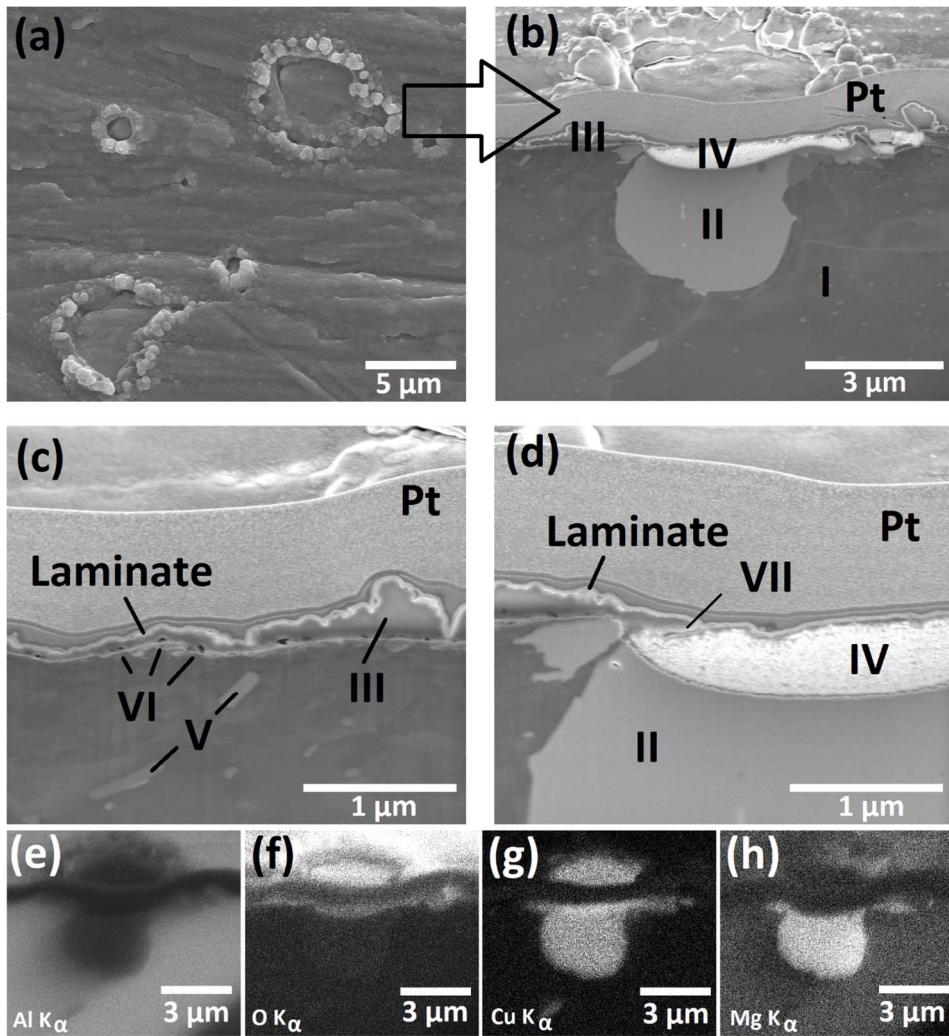


**Fig. 15.** HR-SEM-FIB and SEM-EDX studies of near-surface IMP-s: top view (a), FIB-made cross-section of an entire IMP (b), FIB-made cross-section of a corrosion product area (c), FIB-made cross-section of the interface of the IMP's inner part (II) and oxidized part (IV) (d). The element maps of Al (e), O (f), Cu (g), and Mg (h) as well as a local analysis at sites I, II, III, and IV were taken from the area of image b [52].

**Table 5.** Local elemental analysis results for the sites of interest shown in Fig. 15b [52].

Sites of interest	Elements, mass% ( $\pm 0.1$ mass% for Al, and Cu, and $\pm 0.2$ mass% for other elements)								
	Al	Cu	Mg	O	Cl	Fe	Mn	C	Ti
I	92.2	4.8	0.9	1.5	0.0	0.0	0.5	0.0	0
II	37.0	50.0	10.0	2.3	0.0	0.0	0.0	0.3	0.2
III	66.3	6.8	1.1	16.7	0.3	0.0	0.3	3.9	2.6
IV	28.7	52.4	3.8	9.4	0.7	0.5	0.0	2.8	0.7

Evidently, the cross-sectional studies indicate that the metal-coating interface can vary across the metal substrate. On an Al-rich matrix, for instance, the first layer of the laminate ( $\text{Al}_2\text{O}_3$ ) is in direct contact with the natural aluminum oxide layer, ensuring exceptional adhesion. On Cu IMP-s, however, there is a thin layer of oxidized IMP content that is softer than the surrounding natural aluminum oxide layer, which can weaken the adhesion of the coating locally. In addition, the presence of contaminants in the form of semi-loose particles or a thin film would also weaken the coating's adhesion locally. Semi-loose particles may even disperse and take with them a portion of the protective coating. In the case of slightly corroded surfaces, as depicted in Fig. 15, a similar problem with poor adhesion is probably present. In the latter instance, there is a layer of fluffy corrosion products on top of and surrounding the IMP, resulting in poor adhesion of the coating over a large area. We suspect that ALD coatings fail owing to the presence of abnormally large clusters of IMP-s, which would result in poor adhesion over a large area. Such areas would be significantly more susceptible to mechanical damage owing to the thin ceramic coating's brittleness under mechanical stress, which would allow corrosive species to reach the metal substrates. In our experiments, the samples were handled with extreme care, and any mechanical damage to the surface was prevented. In practical applications, it would be difficult to avoid mechanical interactions with the coated area, which could easily damage the coating in areas where it is not properly adhered to the substrate.

## 5.2. Electrochemical surface engineering

The studies presented in 5.1 suggest that possible contaminants, corrosion products, and near-surface intermetallic particles may weaken the performance of ALD coatings applied to AA2024-T3. Accordingly, in studies I [51] and II [52], investigations concerning potentiodynamic electrochemical pre-treatment of metal substrates are reported to selectively “pluck out” near-surface intermetallic particles from the Al alloy and create an ideal surface for ALD coating. Particularly, two processes were investigated to achieve greater control over coating thickness. In study II [52], a low-potential electrochemical treatment process was used to selectively remove near-surface intermetallic particles without forming an AAO

layer to produce the thinnest coatings. In study I [51], higher anodic potentials were used to create thicker coatings, which resulted in an AAO layer that could then be sealed by ALD with a ceramic material.

### 5.2.1. Effect of the LET process on the surface of AA2024-T3

The polarization curves measured during the LET process (Fig. 16) reveal notable reactions in the  $\sim 50$  mV vs. SCE potential region, which are likely due to the removal of Cu-rich IMP-s close to the surface [59].

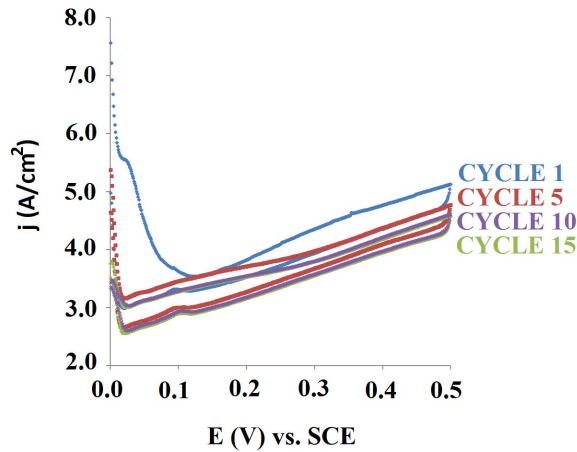


**Fig. 16.** Polarization curves indicating the low-potential electrochemical treatment of AA2024-T3 in sulfuric acid in a three-electrode setup [52].

The efficiency of the LET process for removing near-surface IMP-s was initially evaluated by mapping the distribution of elements using SEM-EDX prior to (Fig. 17a–c) and subsequent to (Fig. 17d–f) the treatment. These studies demonstrated that the initial surface had numerous characteristic sites with a size of 1–10 microns that contained both Cu (Fig. 17b) and Mg (Fig. 17c). Accordingly, these sites contain the greatest number of micrometric  $\text{Al}_2\text{CuMg}$  IMP-s [12]. However, after the LET process, no more Cu (Fig. 17e) and Mg (Fig. 17f) were detected on the surface. Furthermore, after the LET treatment, craters appeared on the surface of the alloy (Fig. 17d, f, red circles), which were likely left behind after the successful removal of large  $\text{Al}_2\text{CuMg}$  IMP-s.

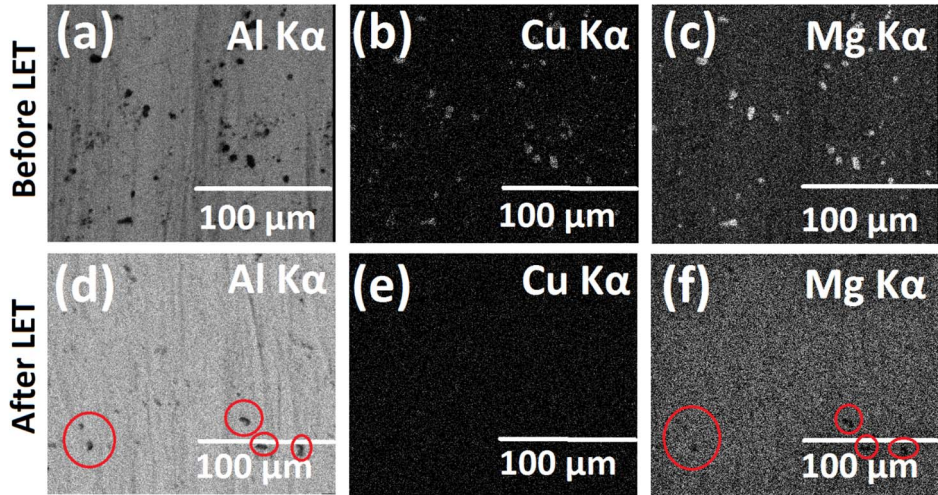


**Fig. 17.** Distribution of Al, Cu, and Mg mapped by SEM-EDX on polished (a–c) and LET-processed (d–f) Al-alloy substrates [52].

The effect of the LET process on the surface of the Al alloy was further studied using HR-SEM (Fig. 18). The surface contains numerous craters that originated from the successful removal of near-surface IMP-s, as depicted by the secondary electron image in Fig. 18a, which is in good agreement with previously measured elemental maps in Fig. 17. Furthermore, the surface also appears very clean and still contains surface features from polishing, which confirms that the LET process only affects the very top layer of the material and does not significantly affect the dimensions of a substrate. A detailed examination of the craters at higher magnification reveals that their depth, shape, and size varied. There were both wide and shallow craters and craters that penetrated deeper into the substrate. Occasionally, some deeper craters contained remnants of the original IMP (Fig. 18b). A high magnification image of the surface (Fig. 18c) reveals a nano-scaled pattern, with pores/holes having a diameter between 2 and 200 nm. This intricate pattern was investigated further by FIB sectioning and HR-SEM analysis (Fig. 18d). This indicates that the LET process did not produce a significant AAO layer on the Al alloy.

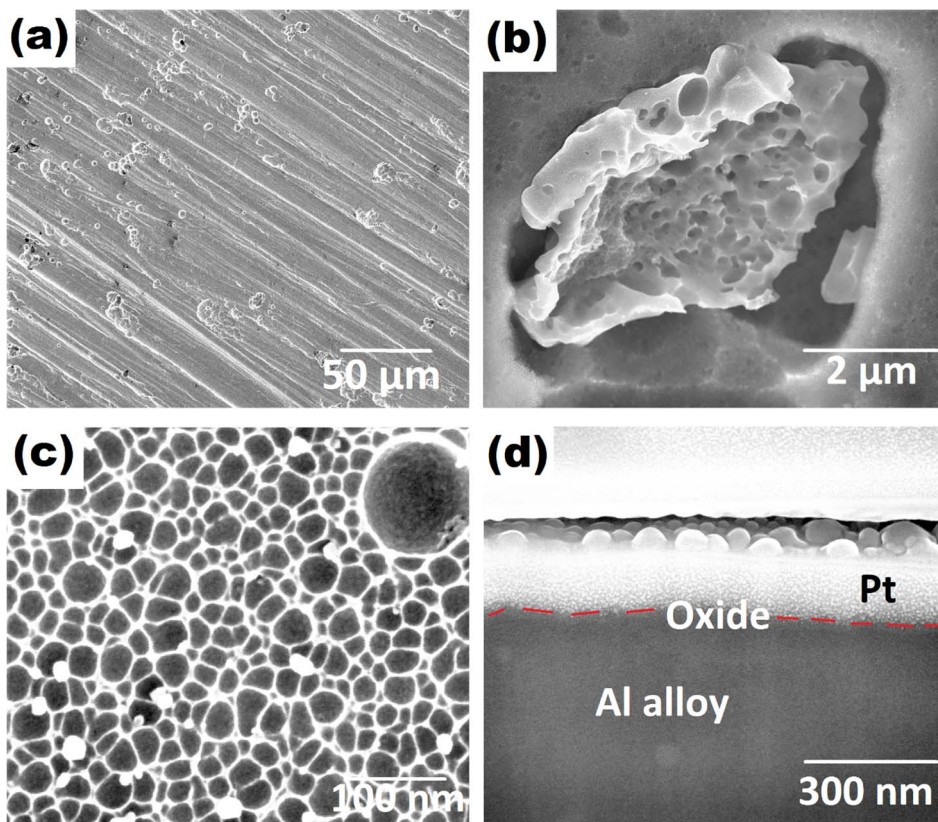


**Fig. 18.** HR-SEM-FIB studies of the LET processed Al alloy, depicting the surface condition after the electrochemical treatment (a), a partially removed intermetallic particle (b), the nanostructure of the surface and the nanoparticles on it (c) and the thin supposed oxide layer (d, red dashed line), separating the alloy and the Pt protection layer used for making the FIB cross-section [52].

To gain a deeper understanding of the fine structure depicted in Fig. 18c, a lamella was created using SEM-FIB for further HR-STEM research. As shown in Fig. 19, the thickness of the oxide layer on the metal substrate ranges from approximately 5 to 10 nm. In addition, the HR-STEM study was conducted at a location that likely corresponds to one of the brighter walls depicted in Fig. 18c. These walls appear to be composed primarily of aluminum that has been oxidized and is at least twice as thick as the surrounding metal oxide layer. Surprisingly, the area beneath the wall contained more Cu and less Al than the surrounding alloy. This Cu appeared to be a component of the alloy and was not added during or after the LET process.

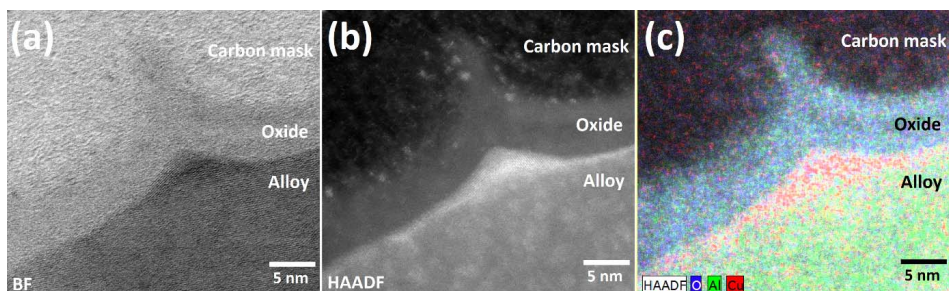


**Fig. 19.** Cross-section lamella STEM images of LET processed Al alloy surface area depicting one of the bright walls seen in Fig. 18c: STEM bright field image (a), STEM-HAADF image (b), and STEM-HAADF image with O (blue), Al (green) and Cu (red) maps' overlay obtained by STEM-EDX in the same region [52].

Consequently, the nanostructure observed in Fig. 18c may have resulted from uneven etching during the LET process. In particular, AA2024-T3 has a complex microstructure, where the uneven distribution of elements results in an uneven etching on a nanometric scale, which is seen in STEM studies (Figs. 19, 20).

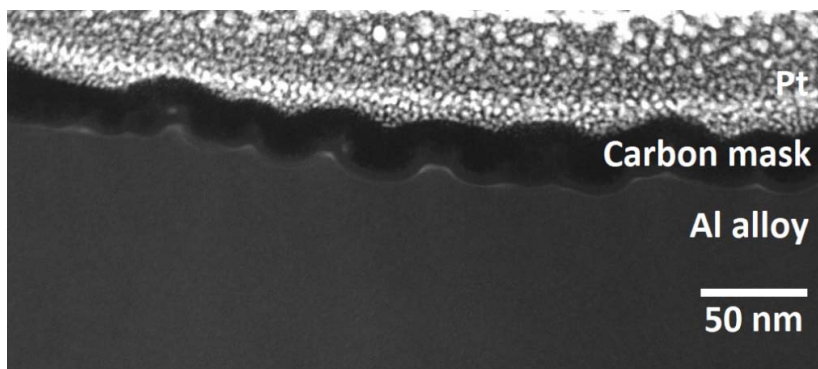


**Fig. 20.** Overview STEM-HAADF image of the LET processed surface of the Al-alloy.

### 5.2.2. Performance of coatings on substrates pre-treated by LET

The studies of substrates following the LET process suggest that the treatment successfully eliminated the potential issues (near-surface IMP-s and possible surface contaminations) that were hypothesized to hinder the performance of ALD coatings. Therefore, substrates treated with LET were coated with ALD and evaluated in 0.5M NaCl by immersion, LSV, and EIS (Table 6, Figs. 21, 22).

**Table 6.** Data of the LSV and EIS experiments for only the LET substrate and the LET plus TiO<sub>2</sub>, Al<sub>2</sub>O<sub>3</sub>, the Al<sub>2</sub>O<sub>3</sub>-TiO<sub>2</sub> mixture, and Al<sub>2</sub>O<sub>3</sub>/TiO<sub>2</sub> nanolaminate-coated samples [52].

Surface pretreatment and coating	Corrosion potential	Current density at -1 V	Current density at 1 V	Impedance at 10 mHz after 30 min	Impedance at 10 mHz after 24 h	Coating efficiency
	$E_{cor}$ , V	$j_{start}$ , A/cm <sup>2</sup>	$j_{max}$ , A/cm <sup>2</sup>	$ Z_1 $ , $\Omega$	$ Z_2 $ , $\Omega$	CE (Eq. 1)
LET	-0.55	$8.7 \times 10^{-6}$	0.10	-	-	0.49
LET+TiO <sub>2</sub>	-0.56	$2.5 \times 10^{-7}$	0.13	$1.4 \times 10^4$	$1.4 \times 10^4$	0.36
LET+Al <sub>2</sub> O <sub>3</sub>	-0.47	$4.3 \times 10^{-8}$	0.06	$4.5 \times 10^6$	$2.0 \times 10^5$	0.69
LET + Al <sub>2</sub> O <sub>3</sub> -TiO <sub>2</sub> mixture	-0.47	$1.1 \times 10^{-7}$	0.15	$1.9 \times 10^6$	$9.9 \times 10^5$	0.25
LET + Al <sub>2</sub> O <sub>3</sub> /TiO <sub>2</sub> nanolaminate	-0.41	$3.3 \times 10^{-7}$	0.04	$5.2 \times 10^7$	$1.1 \times 10^7$	0.81

LSV studies (Fig. 21) of ALD-coated substrates reveal that the use of LET pre-treatment in addition to the standard pre-treatment results in lower measured current densities in the scanned potential range compared to substrates that received only the standard pre-treatment (Fig. 21, curves 2–5). We also measured lower current densities for the bare substrate with LET- pre-treatment (Fig. 21, curve 1). However, among the coated substrates, only a negligible improvement was observed for TiO<sub>2</sub> (Fig. 21, curve 2) and Al<sub>2</sub>O<sub>3</sub>-TiO<sub>2</sub> mixture (Fig. 21, curve 4) coatings when LET was added to the standard pre-treatment. In the case of the latter two coatings, the polarization scan measured slightly lower current densities for LET-treated substrates. In contrast to the aforementioned coatings, Al<sub>2</sub>O<sub>3</sub> (Fig. 21, curve 3) and Al<sub>2</sub>O<sub>3</sub>/TiO<sub>2</sub> nanolaminate (Fig. 21, curve 5) coatings indicated a much greater improvement using the LET process, as the measured current densities in the LSV test were significantly lower compared to substrates that only had a standard pre-treatment and the same coating (Fig. 8, curves 3, 5). Nonetheless, the LSV studies demonstrated that the substrate with LET pre-treatment and nanolaminate coating (Fig. 21, curve 5) does not display a significant passive region at anodic potentials. Nonetheless, the latter substrate demonstrates the best performance and has the highest CE value of 0.8 (Table 6), which is the closest to a perfect coating where CE equals 1.

Fig. 22 depicts photographs of uncoated and coated substrates with LET pre-treatment following a 1000 h immersion test. These tests demonstrated that the LET procedure had no effect on the corrosion resistance of the alloy (Fig. 22a). A similar behavior was observed for ALD-grown TiO<sub>2</sub> (Fig. 22b) and Al<sub>2</sub>O<sub>3</sub> (Fig. 22c) coatings on substrates. In contrast, the LET process marginally



improved the performance of the  $\text{Al}_2\text{O}_3$ - $\text{TiO}_2$  mixture coating (Fig. 22d), which after the 1000h immersion test had only a few barely visible corrosion sites in the substrate's center. Nevertheless, the LET process significantly improved the performance of the nanolaminate coating (Fig. 22e), which was also the best in the immersion test, as it exhibited no corrosion sites after 1000 h of immersion. After 1800 h of immersion in 0.5M NaCl, the latter substrate exhibited the first signs of corrosion (Fig. 22f).

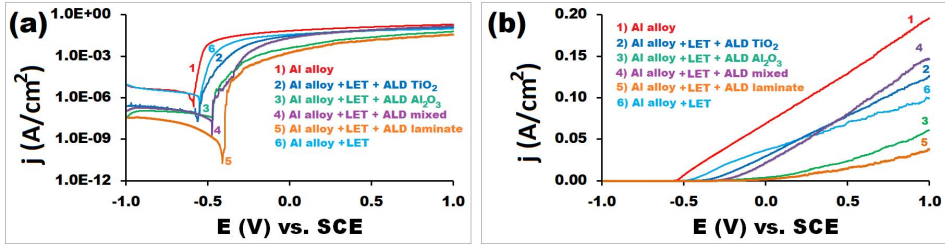


**Fig. 21.** Polarization curves (a, b) for differently pretreated/coated sample surfaces: just polished, curve 1, LET plus ALD with  $\text{TiO}_2$ , curve 2,  $\text{Al}_2\text{O}_3$ , curve 3, the  $\text{Al}_2\text{O}_3$ - $\text{TiO}_2$  mixture, curve 4, the  $\text{Al}_2\text{O}_3$ / $\text{TiO}_2$  nanolaminate, curve 5, and just LET curve 6 [52].

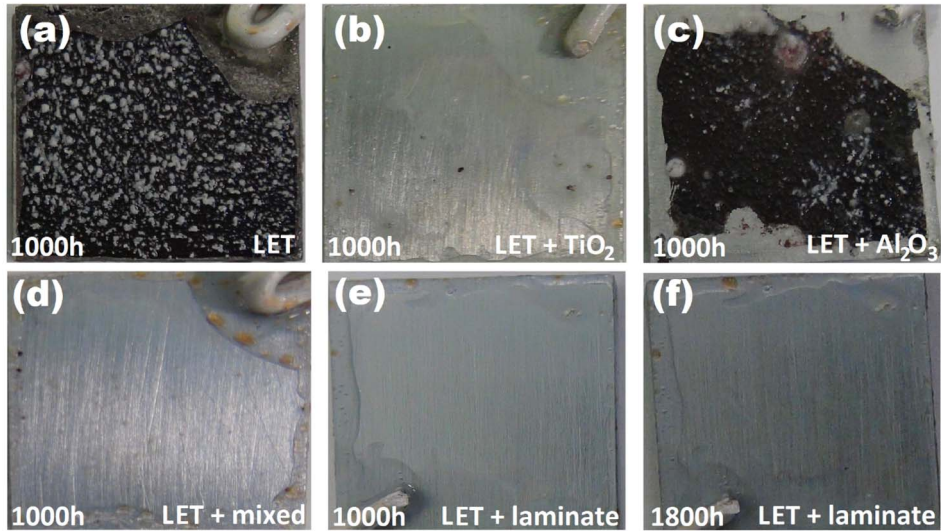


**Fig. 22.** Photographs of the  $20 \times 20 \text{ mm}^2$  samples after a 1000 h immersion test that had just LET (a) and LET plus ALD with  $\text{TiO}_2$  (b),  $\text{Al}_2\text{O}_3$  (c), the  $\text{Al}_2\text{O}_3$ - $\text{TiO}_2$  mixture (d), and the  $\text{Al}_2\text{O}_3$ / $\text{TiO}_2$  nanolaminate (e), and the latter after an additional 800 h immersion test (f) [52].

### 5.2.3. Effect of potentiodynamic anodizing on the surface of AA2024-T3

The potentiodynamic anodizing of the Al alloy was investigated in study I [49], and was performed using a potentiostat in BSA (Fig. 23a, b) and SA (Fig. 23c, d) electrolytes. As seen in Figs. 23a, c, the first notable process occurs at  $\sim 50$  mV, which is similar to the LET process (Fig. 16) and can be attributed to the removal of Cu-rich IMP-s [59]. The greatest change to the surface occurs during the first cycle (Figs. 23a, c, curve 1), when most of the Cu near the surface is possibly removed. In subsequent cycles, the measured current densities also decrease gradually, suggesting gradual oxidation of the metal surface and successful elimination of IMP-s (Figs. 23a, c, curve 2–4). Notably, SA (Fig. 23c) appears to be more effective than BSA at removing IMP-s (Fig. 23a). In the second stage (Figs. 23b, d), cycling was performed up to 10V vs. SCE, which caused the greatest change during the initial cycle (Figs. 16b, d, curve 1). Owing to the formation of the AAO layer, the measured current densities gradually decreased over the subsequent cycles (Fig. 16b, d, curve 2–50).

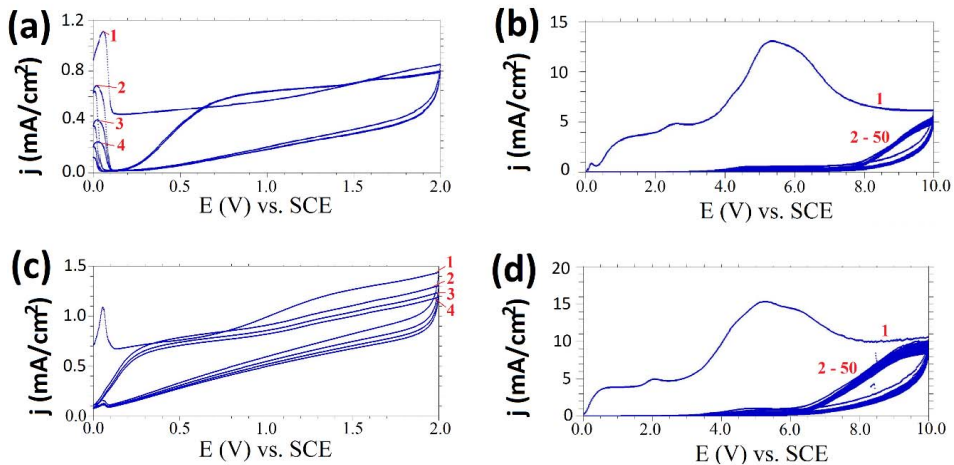


**Fig. 23.** Polarization curves indicating the alloy anodizing with (a, b) BSA and (c, d) SA in the (a, c) first and (b, d) second steps [51].

The SEM analyses of the anodized substrates in BSA (Fig. 24a–c) and SA (Fig. 24d–f) reveals the effect of the electrochemical treatment on the surface of the alloy. Both electrolytes created micrometric craters on the surface, which can be attributed to the removal of the most abundant  $\text{Al}_2\text{CuMg}$  IMP-s, as revealed by a low-magnification image of the surface. This is consistent with the polarization curves measured during the anodizing process (Fig. 23) and the LET process studies (Figs. 16–18). The HR-SEM studies of the surface at greater magnifications revealed a nano-scaled structure with  $< 20$  nm holes or pores (Fig. 24b, e). The latter SEM images also depict cylindrical holes that were likely left behind

after the successful removal of  $\text{Al}_{20}\text{Mn}_3\text{Cu}_2$  IMP-s [12]. Additional research was conducted by creating a cross-section with FIB and analyzing it with HR-SEM (Fig. 24c, f). Prior to preparing the FIB cross-sections, the pores in the AAO were filled with  $\text{TiO}_2$  using ALD to achieve a higher contrast for better visualization. The  $\text{TiO}_2$  deposited within the pores appears darker than the AAO that surrounds it (Fig. 24c, f). Studies of cross-sections revealed that the thickness of the obtained AAO layer was  $\leq 0.5 \mu\text{m}$  and  $\leq 2 \mu\text{m}$  for BSA (Fig. 24c) and SA (Fig. 24f), respectively. Furthermore, the AAO obtained with BSA (Fig. 24c) appears to be denser than the AAO produced with SA (Fig. 24f). A similar behavior was previously observed by Du et al. [60]. Furthermore, the difference in thickness may be attributable to the presence of sulfuric acid in the anodizing electrolytes [61].

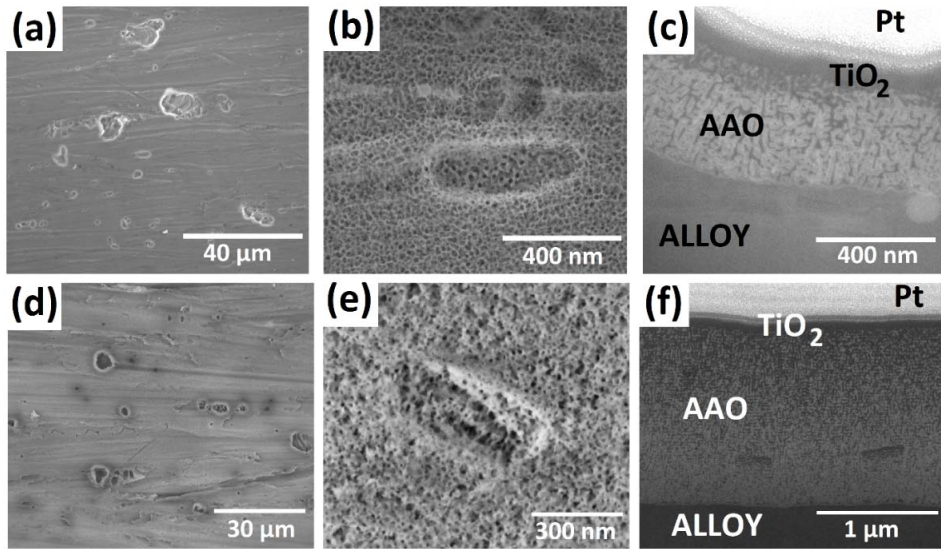


**Fig. 24.** SEM images of the surfaces of the samples anodized with (a–c) BSA and (d–f) SA, showing the removal of (a, d) micrometric and (b, e) nano-scale surface inclusions; (c, f) FIB cross-sections of the corresponding samples after sealing the AAO pores with  $\text{TiO}_2$  [51].

#### 5.2.4. Sealing and coating of AAO with nanolaminate by ALD

Nanolaminate  $\text{Al}_2\text{O}_3/\text{TiO}_2$  was grown by ALD on Al alloy substrates anodized in BSA and SA. This resulted in a novel coating in which the AAO was coated with another ceramic material and then sealed (Fig. 25). Specifically, the bottom portion of the new coating is composed of the AAO matrix that has been sealed with  $\text{Al}_2\text{O}_3$  via ALD. The pores in the AAO had a diameter of  $< 20 \text{ nm}$ , and the first layer of the nanolaminate,  $\text{Al}_2\text{O}_3$ , had a thickness of  $\sim 18 \text{ nm}$ , making this possible. In an ideal situation, a  $20 \text{ nm}$  pore can be sealed by ALD by growing only  $10 \text{ nm}$  of a material, as the deposition of the material occurs simultaneously on all of the pore walls, causing the pore diameter to decrease by  $2 \text{ nm}$  for every  $1 \text{ nm}$  of material grown by ALD.

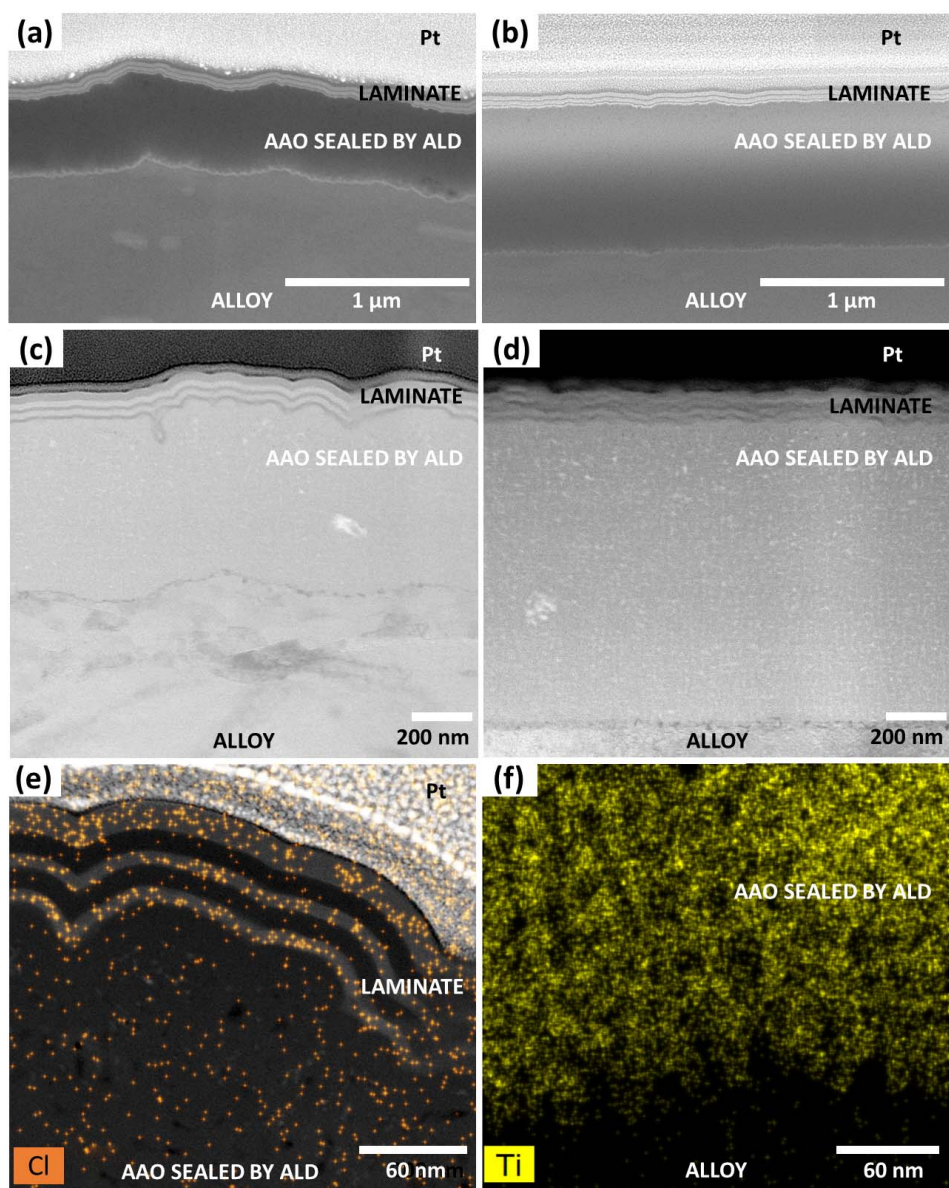


**Fig. 25.** Cross-sectional images of the novel nanostructured coatings: (a, b) HR-SEM secondary electron images of the coatings prepared with anodizing in BSA and SA, respectively, (c, d) STEM-BF images of the same, (e) STEM-HAADF image with Cl map overlay of the coating prepared with anodizing in BSA, and (f) STEM-EDX map of Ti of the lower part of the AAO sealed with titania by the help of ALD, similar to that shown in Fig. 24c [51].

Note that the pores of the AAO are not visible in the STEM images shown in Fig. 25a–d because the AAO and  $\text{Al}_2\text{O}_3$  grown by ALD have the same composition and density. Because the first layer of  $\text{Al}_2\text{O}_3/\text{TiO}_2$  nanolaminate grown by ALD is sufficient to seal the AAO, subsequent layers only serve to coat the surface of the substrate (Fig. 25a–d). Consequently, no Cl from the  $\text{TiCl}_4$  precursor enters the AAO during the process of sealing (Fig. 25e). When preparing such coatings, it is necessary to demonstrate that ALD effectively seals the pores' bottoms. To map the distribution of Ti at the bottom of the pores of the AAO layer, an additional HR-STEM study was performed on an anodized substrate that was sealed with  $\text{TiO}_2$  (Fig. 25f). This study demonstrates a higher concentration of Ti until the alloy | AAO interface, indicating that  $\text{TiO}_2$  was indeed deposited into the bottom of the pores and that the pores did not become clogged early in the ALD process, which would have prevented further deposition of  $\text{TiO}_2$  into the pores.

The coating obtained by combining potentiodynamic anodizing and nanolaminate grown by ALD greatly improved the corrosion resistance of AA2024-T3 (Fig. 26). Particularly, the measured polarization curves for coated substrates are several orders of magnitude lower than those for bare substrates (Fig. 26a, curves 2, 3). In addition, when the coated substrates were exposed to an anodic potential of 10 V, no pitting was observed (Fig. 26, curves 2, 3). Comparing the polarization curves of coated substrates in Fig. 26b reveals that the coating obtained by anodizing in BSA has a slightly higher current density at 10 V than the substrate anodized in SA prior to ALD coating. Regardless, both coated substrates exposed to 10 V in the LSV experiment indicated no visible damage. By applying Eq. 1, the calculated short-term coating efficiency for both coatings is 1, the same as for a dielectric and defect-free ideal coating.

The long-term corrosion resistance of the coating made by anodizing in BSA and coating with the nanolaminate by ALD was tested by 7152 h (~298 days) immersion in 0.5 M NaCl aqueous solution. As seen in photographs taken prior to (Fig. 26c) and following (Fig. 26d) the corrosion test, the coated substrate remained essentially undamaged. In contrast, a bare substrate experienced severe corrosion after a 1000 h immersion test (Fig. 9a). Note that the coated substrate suffered some corrosion damage at the holes and edges as a result of the substrates being handled during the coating preparation process. In particular, the holes were used during the anodizing process to suspend the substrate in the anodizing solution using an aluminum wire that also served as an electrical connection. Consequently, the formation of AAO would have been inhibited at the wire-substrate interface. In addition, the edges of the plate may have been damaged or contaminated during the preparation of substrates for ALD coating in the industrial reactor.

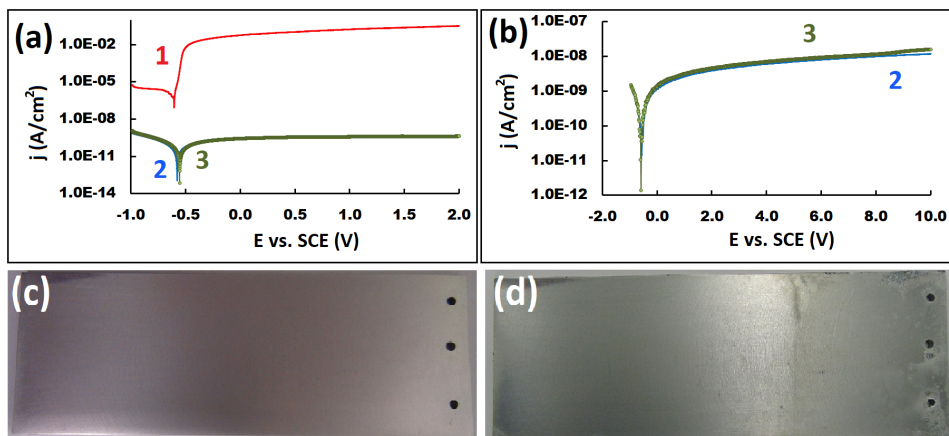


**Fig. 26.** Corrosion tests using LSV: (a, b) a polished sample (curve 1), a sample anodized in SA and coated with the nanolaminate (curve 2), and a sample anodized in BSA and coated with the nanolaminate (curve 3) (a) in a narrower potential range near the corrosion potential region and (b) in a broader potential range; (c, d) photographs of a large sample anodized in BSA and coated with the nanolaminate (c) before and (d) after the 7152 h (298 days) immersion in 0.5 M NaCl solution [51].

The EIS analysis was conducted on coated substrates anodized in BSA and SA electrolytes and then coated with the nanolaminate using ALD (Fig. 27). EIS was designed to evaluate the stability of these coatings during a 24-h immersion in aqueous 0.5M NaCl solution. Therefore, EIS measurements were conducted at the beginning (denoted as “0h”) and at the end of 24 h immersion (denoted as “24h”) in 0.5 M NaCl at room temperature.

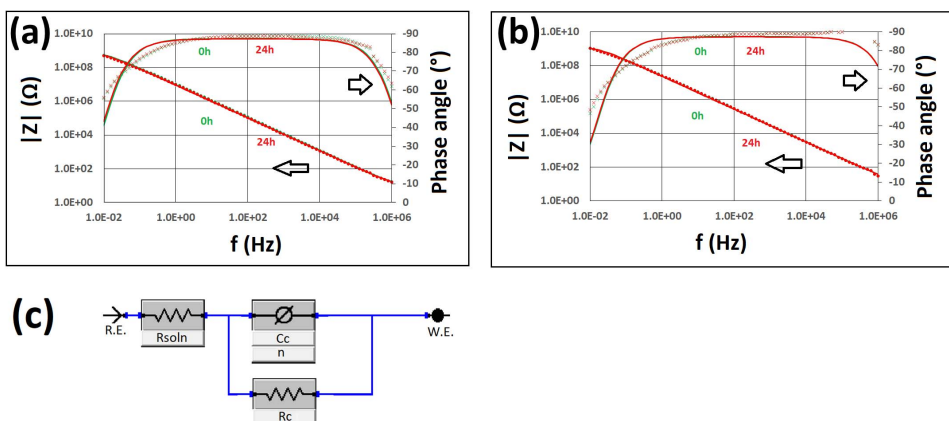


**Fig. 27.** Bode plots for Al alloy substrates anodized in BSA (a), SA (b), and then coated by ALD with 100 nm nanolaminate. The ECM (c) was utilized to model the previously mentioned plots [51].

As shown in Figs. 27a, b, the measured impedance ( $|Z|$ ) and phase angle ( $\theta$ ) curves did not change during the 24 h immersion test, indicating that the coatings remained stable and undamaged. In addition, the nearly linear behavior of the impedance curves throughout the entire frequency range of  $2 \cdot 10^{-2}$ – $10^5$  Hz also confirmed the high quality of the coating. In addition, the phase angle curve had a broad frequency range close to  $90^\circ$ . Finally, the ECM depicted in Fig. 27c was used to model the second coating's behavior of the second coating. The modeled values of  $R_c$ ,  $C_c$ , and  $n$  for the coated substrates did not change during the 24 h immersion test, which confirms that the coatings are defect-free and do not degrade during that time in an aqueous 0.5 M NaCl environment (Table 7).

**Table 7.** ECM variables (Fig. 27c) calculated for coated Al alloy substrates before and after the immersion test [51].

EMC variables	Coatings			
	BSA anodized + 100 nm ALD nanolaminate		SA anodized + 100 nm ALD nanolaminate	
Immersion time, h	0	24	0	24
$R_{soln}, \Omega \cdot \text{cm}^2$	10.0	10.0	10.0	10.0
$R_c$	$7.5 \times 10^8$	$7.4 \times 10^8$	$1.2 \times 10^9$	$1.3 \times 10^9$
$C_c, \text{F} \cdot \text{cm}^{-2} \cdot \text{s}^{n-1}$	$1.8 \times 10^{-8}$	$1.9 \times 10^{-8}$	$7.2 \times 10^{-9}$	$7.2 \times 10^{-9}$
$n$	0.97	0.97	0.97	0.97

### 5.3. Nanostructured Coatings

The studies on using potentiodynamic anodizing in study I [51] and the LET process in study II [52] for pre-treatment of AA2024-T3 indicated a notable increase in the performance of coatings grown by ALD. Furthermore, the sealing of the AAO in study I [49] with a nanolaminate by ALD produced a new type of ceramic coating that exhibited excellent corrosion resistance under anodic potentials and during prolonged immersion in saltwater. However, the potentiodynamic anodizing procedure was only applicable to small substrates, required a complex setup, and had temperature control issues. In study III [53], the next step was to examine the use of a simple two-electrode setup with an external ice bath for potentiostatic anodizing, to produce an AAO suitable for sealing by ALD. In study III [53], various materials were grown into the AAO obtained by potentiostatic anodizing to produce nanostructured coatings. These coatings were then characterized by various methods and optimized for aerospace industry applications.

### 5.3.1. Effect of potentiostatic anodizing on AA2024-T3

Fig. 28 depicts the SEM-FIB studies of substrates that received potentiostatic anodizing pre-treatments in paper III [53]. Low-magnification surface studies of the anodized substrate reveal the presence of numerous shallow craters (Fig. 28a), similar to those obtained during the LET process (Fig. 18a), indicating the successful removal of IMP-s including  $\text{Al}_2\text{CuMg}$ . The HR-SEM-FIB studies of the cross-section reveal nanoscale pores in the AAO (Fig. 28b). Prior to cross-section studies, ALD was used to deposit  $\text{TiO}_2$  into the pores of the AAO to enhance the visibility of nano-scaled pores on the second image. The AAO layer obtained with potentiostatic anodizing (Fig. 28b) at 20 V, 1 °C is less porous than the AAO obtained with potentiodynamic anodizing up to 10 V at RT (Fig. 24f). The diameter of the pores in the AAO are < 10 nm for the former AAO (Fig. 28b) and < 20 nm for the latter AAO (Fig. 24f). A detailed SEM examination of the anodized surface also revealed rare, deeper craters surrounded by cracks (Fig. 28c). These craters are likely the result of IMP-s that were partially exposed to the surface prior to anodization. Such craters were not previously observed on substrates that had been pre-treated with potentiodynamic anodizing (Fig. 24). The SEM-FIB analyses of the latter craters reveal their intricate internal structure (Fig. 28d–f), which is essential when preparing nanostructured coatings by sealing the AAO with ALD-grown materials. Specifically, the arrows in Figs. 28e and f indicate that cracks penetrate the AAO and reach the metal substrate. In addition, the metal alloy (Figs. 28e, f, site I) is gradually transformed into AAO during the anodizing procedure (Figs. 28e, f, site II). During this process, new IMP-s from deeper layers (Figs. 28e, f, site III) are exposed and then removed, which may leave cavities in the AAO layer (Figs. 28e, f, site IV). Regardless, the cross-sectional image in Fig. 28f demonstrates that ALD can effectively seal both nano-scaled pores and the bottoms of larger cracks, thereby enabling the creation of a variety of nanostructured coatings.



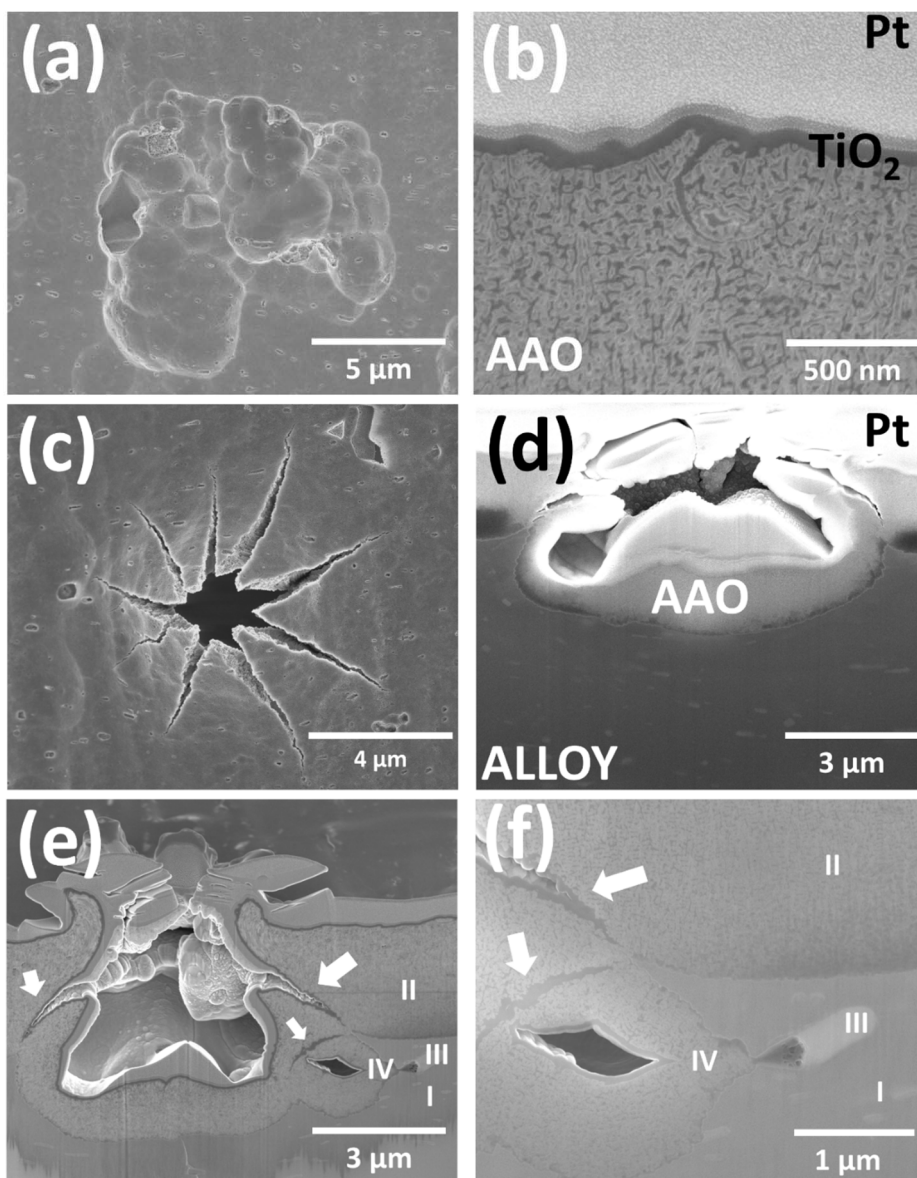


**Fig. 28.** SEM images of the AAO layer obtained by potentiostatic anodizing at 20 V, 1 °C depicting the most abundant shallow craters from the removal of micrometric IMP-s (a), FIB-made cross-section of the AAO layer sealed with TiO<sub>2</sub> for better imaging of the 3D structure of the nanopores (b), top view of a cracked crater (c), FIB-made cross-section of a cracked crater (d), cross-section of another cracked crater sealed with TiO<sub>2</sub> via ALD for the demonstration of the sealing efficiency (e); image (f) shows the right part of the image (e) with greater magnification. In (e) and (f) the regions of the metal substrate, nanoporous AAO layer and a partly removed IMP are marked as sites I, II, and III respectively. The arrows point to the cracks and site IV shows a gap left by the IMP during the anodizing process and sealed afterward with ALD [53].

### 5.3.2. Impregnation of AAO with different materials grown by ALD

In study III [53], a systematic investigation was conducted to determine the optimal material for sealing the AAO layer produced by potentiostatic anodizing at 10 V, 1 °C, and 20 V, 1 °C to produce an effective nanostructured coating. For this stage in the development of efficient coatings, we have selected potentiostatic anodizing, which is scalable for industrial applications and can be conducted with a relatively inexpensive setup, requiring only ALD post-treatment. Using appropriately chosen ALD pulse times, Al<sub>2</sub>O<sub>3</sub>, TiO<sub>2</sub>, Al<sub>2</sub>O<sub>3</sub>-TiO<sub>2</sub> mixture, and Al<sub>2</sub>O<sub>3</sub>/TiO<sub>2</sub> nanolaminate films were grown on anodized substrates using ALD in these systematic studies. The chosen target thickness for ALD-grown films was 50 nm, which was believed to be sufficient to seal the nano-sized pores in the AAO layer previously observed in Fig. 28b.

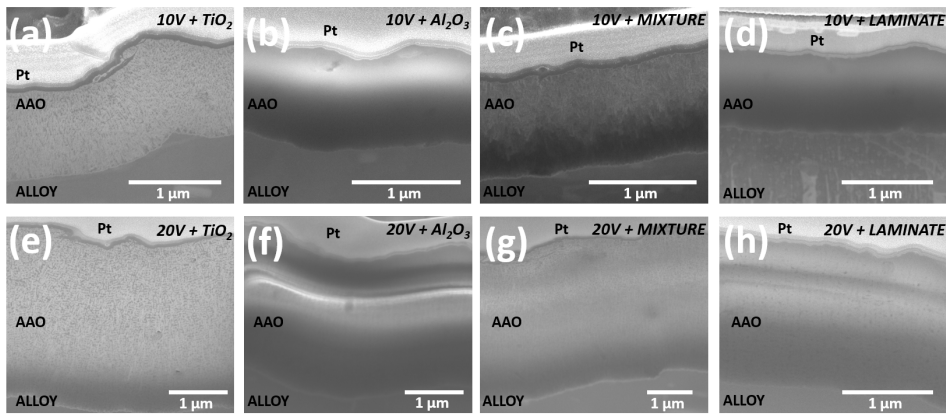


**Fig. 29.** SEM images of the FIB made cross-sections of Al-alloy substrates anodized at 10 V, 1 °C (a–d) and 20 V, 1 °C (e–h), having the AAO layer sealed by ALD with 50 nm TiO<sub>2</sub> (a,e), Al<sub>2</sub>O<sub>3</sub> (b,f), Al<sub>2</sub>O<sub>3</sub>-TiO<sub>2</sub> mixture (c,g) or Al<sub>2</sub>O<sub>3</sub>/TiO<sub>2</sub> nanolaminate (d,h) [53].

The investigation of obtained nanostructured coatings by SEM-FIB revealed that it is possible to seal the nano-scaled pores in the AAO obtained with potentiostatic anodizing at 10 V, 1 °C (Fig. 29a–d) and 20 V, 1 °C (Fig. 29e–h) by ALD with various ceramic materials including TiO<sub>2</sub> (Fig. 29a, e), Al<sub>2</sub>O<sub>3</sub> (Fig. 29b, f), Al<sub>2</sub>O<sub>3</sub>-TiO<sub>2</sub> mixture (Fig. 29c, g), and Al<sub>2</sub>O<sub>3</sub>/TiO<sub>2</sub> nanolaminate (Fig. 29d, h). The cross-section studies also revealed the thickness of the AAO, which was 1 μm at 10 V, 1 °C and over 2 μm when anodized at 20 V, 1 °C. Additionally, note that the first layer of the nanolaminate consisted of 20 nm of Al<sub>2</sub>O<sub>3</sub>. This was done to ensure that only Al<sub>2</sub>O<sub>3</sub> and not TiO<sub>2</sub> would seal the nanoscale pores in the AAO layer. Thus, TiO<sub>2</sub> would have deposited only in larger pores or cavities that were not completely sealed by the initial 20 nm Al<sub>2</sub>O<sub>3</sub> layer.

### 5.3.3. Linear sweep voltammetry study of nanostructured coatings

Fig. 30 depicts the polarization curves obtained by LSV in study III [53] for nanostructured coatings; Fig. 31 depicts photographs of tested substrates, and Table 8 provides a summary of the data. The LSV data was also used to calculate the short-period coating efficiency,  $CE$  by applying Eq. 1. These results indicate that the performance of coatings is dependent on both the anodizing potential and the material used to seal the AAO layer by ALD. In this systematic study, anodizing was conducted at 10 V, 1 °C, and 20 V, 1 °C, and the desired ALD-grown material thickness was 50 nm. As a rule, applying anodizing as a pretreatment substantially improved the performance of the coatings.

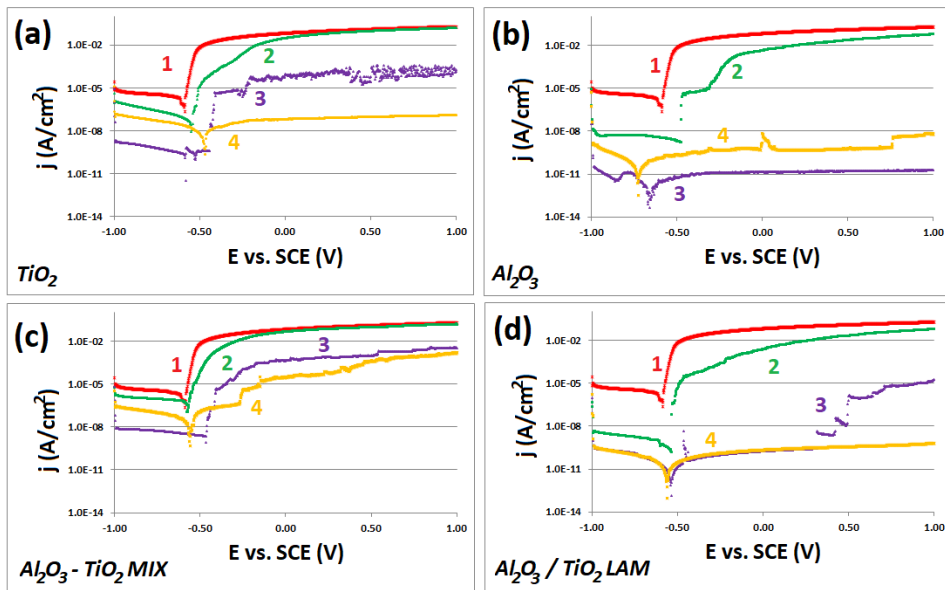


**Fig. 30.** Linear sweep voltammetry corrosion tests for Al-alloy substrates coated with 50 nm  $\text{TiO}_2$  (a),  $\text{Al}_2\text{O}_3$  (b),  $\text{Al}_2\text{O}_3$ - $\text{TiO}_2$  mixture (c), or  $\text{Al}_2\text{O}_3/\text{TiO}_2$  nanolaminate (d), demonstrating the polarization curves for the: polished sample (1), polished samples coated by ALD (2), samples that were anodized at 10 V, 1 °C, and coated by ALD (3), samples that were anodized at 20 V, 1 °C, and coated by ALD (4) [53].

$\text{TiO}_2$  nanostructured coatings, where AAO was sealed with  $\text{TiO}_2$  by ALD, exhibit the best performance when anodized at 20 V, 1 °C (Fig. 30a, curve 4). In the case of this coating, neither pitting nor visible defects were detected during the polarization scan nor on the sample surface after the test (Fig. 31i). Notably, this nanostructured coating exhibited the highest current density values at anodic potentials relative to other nanostructured coatings that did not exhibit pitting during LSV studies. This is due to the higher conductivity of amorphous  $\text{TiO}_2$  compared to the other ALD-grown films in this study. Using 10 V, 1 °C anodizing for pre-treatment and  $\text{TiO}_2$  sealing resulted in a nanostructured coating with excellent performance, as no visible defects were observed in the LSV test

(Fig. 31e). Curve 3 of the polarization curve in Fig. 30a indicates the presence of pitting corrosion on the substrate that was anodized at 10 V and 1 °C as a pre-treatment.

In the LSV experiment, Al<sub>2</sub>O<sub>3</sub>-based nanostructured coatings where AAO was sealed by ALD with Al<sub>2</sub>O<sub>3</sub> typically exhibit low current densities (Fig. 30b, curves 3, 4). Using 10 V and 1 °C as opposed to 20 V and 1 °C for pre-treatment resulted in a slightly improved performance, as no pitting was observed during the polarization scan. The low current densities measured during the LSV experiment can be generally attributed to the dielectric properties of Al<sub>2</sub>O<sub>3</sub>. Photographs taken after LSV testing on substrates anodized at 10 V, 1 °C or 20 V, 1 °C prior to Al<sub>2</sub>O<sub>3</sub> ALD sealing did not reveal any damage (Fig. 31f, j).

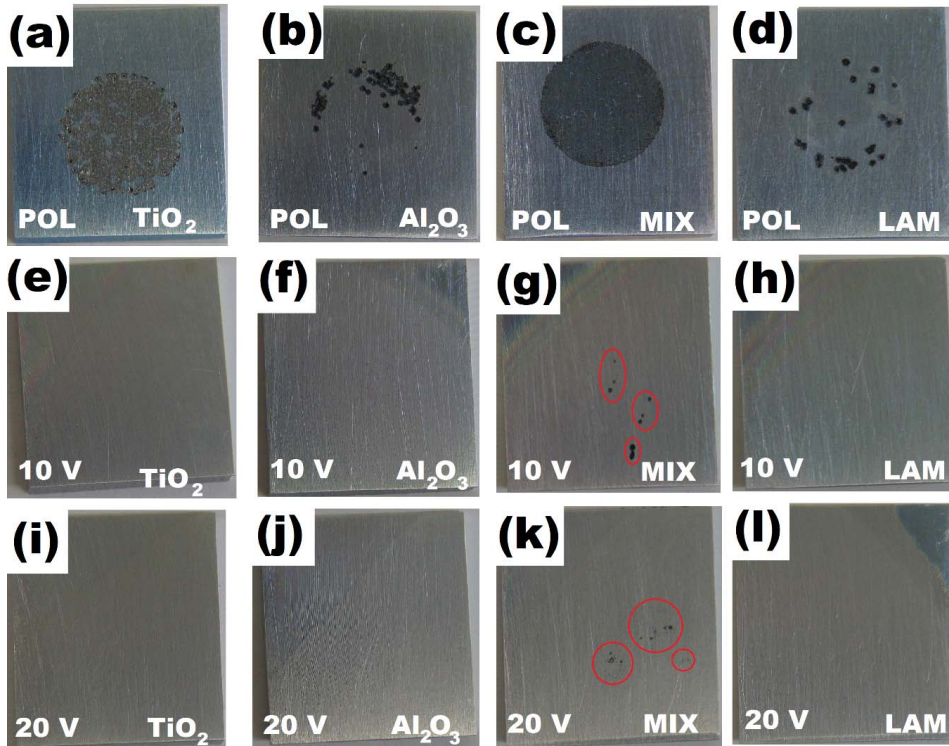


**Fig. 31.** Photos taken after linear sweep voltammetry test depicting 20 × 20 mm<sup>2</sup> Al-alloy substrates that were polished (a–d), anodized at 10 V, 1 °C (e–h), anodized at 20 V, 1 °C (i–l) and then coated by ALD with TiO<sub>2</sub> (a, e, i), Al<sub>2</sub>O<sub>3</sub> (b, f, j), Al<sub>2</sub>O<sub>3</sub>-TiO<sub>2</sub> mixture (d, g, k), and Al<sub>2</sub>O<sub>3</sub>/TiO<sub>2</sub> laminate (d, h, l). The tests were performed with circular masks, exposing 1 cm<sup>2</sup> of the substrate to the electrolyte [53].

In LSV studies,  $\text{Al}_2\text{O}_3\text{-TiO}_2$  mixture-based nanostructured coatings, where AAO was sealed by ALD with  $\text{Al}_2\text{O}_3\text{-TiO}_2$  mixture, exhibit the poorest performance (Fig. 30c, curves 3, 4). Specifically, the measured current densities increase drastically near the corrosion potential region, indicating pitting corrosion. The photographs taken after the LSV tests reveal numerous corrosion sites on both samples with nanostructured  $\text{Al}_2\text{O}_3\text{-TiO}_2$  coatings (Fig. 31g, k). However, the protection provided by the nanostructured  $\text{Al}_2\text{O}_3\text{-TiO}_2$  coating outperformed all of the polished substrates with 50 nm ALD-grown ceramic coatings.

$\text{Al}_2\text{O}_3/\text{TiO}_2$  nanolaminate-based nanostructured coatings, where AAO was sealed by ALD with  $\text{Al}_2\text{O}_3/\text{TiO}_2$  nanolaminate, exhibit generally good performance in the LSV studies, as the measured current densities at anodic potentials are among the lowest when compared to other nanostructured coatings (Fig. 30d, curves 3, 4). Particularly, anodizing at 20 V and 1 °C results in a nanostructured coating that exhibits no pitting throughout the entire potential scan range (Fig. 30d, curve 4). The photographs taken following the LSV test also demonstrate that the nanostructured coatings were unharmed (Fig. 31h, l).

### 5.3.4. Hardness of nanostructured coatings

Fig. 32 depicts the nanoindentation studies of coated and uncoated substrates of study III [53]. In the case of nanostructured coatings, nanoindentation studies were conducted on samples anodized at 10 V and 1 °C and 20 V and 1 °C prior to sealing and coating by ALD by depositing films with a desired thickness of 50 nm.

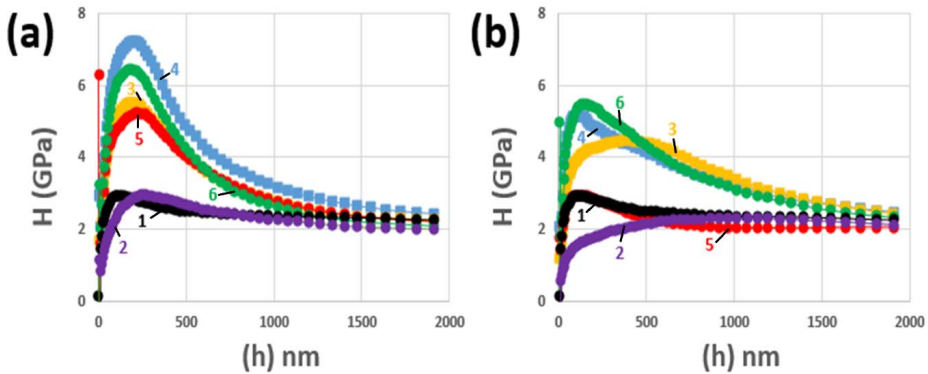


**Fig. 32.** Surface hardness (H) vs indentation depth (h) curves of anodized at 10 V, 1 °C (a) and 20 V, 1 °C (b) samples with added **curves 1** belonging to the just-polished substrate. The **curves 2** belongs to anodized samples; other curves to anodized and ALD sealed and coated samples, using 50 nm of **TiO<sub>2</sub> (curve 3)**, **Al<sub>2</sub>O<sub>3</sub> (curve 4)**, **Al<sub>2</sub>O<sub>3</sub>-TiO<sub>2</sub> mixture (curve 5)** or **Al<sub>2</sub>O<sub>3</sub>/TiO<sub>2</sub> nanolaminate (curve 6)** [53].

At 100 nm surface depth, **Al alloy** demonstrates the highest hardness value of 3 GPa (Fig. 32, curve 1). At greater displacement values, the hardness decreases gradually and approaches 2.3 GPa. The effect of cold working on the surface [1], which was milled and then polished with sandpaper, may account for the higher hardness of the near-surface region.

**AAO layer** obtained by anodizing at 10 V, 1 °C exhibited comparable hardness to the uncoated Al alloy, with a slight variation (Fig. 32a, curve 2). Particularly, the surface of the AAO layer in the 0–100 nm indentation depth range exhibited lower hardness values than the bare Al alloy. However, the AAO obtained by anodizing at 20 V and 1 °C has even lower hardness values than other substrates up to 500 nm displacement depth (Fig. 32b, curve 2). At larger displacement values, the hardness increases to 2.3 GPa, which was also measured for the uncoated aluminum alloy (Fig. 32, curve 1). As the AAO is porous by nature, the low hardness values measured at the top of the AAO layer were expected and have been observed in previous SEM-FIB studies (Fig. 28).

**TiO<sub>2</sub>-based** nanostructured coatings, where AAO was sealed with TiO<sub>2</sub> by ALD, have a significantly higher maximum hardness in the near-surface region (Fig. 32, curve 3) than the unsealed anodized substrate (Fig. 32, curve 2). The dramatic increase in hardness can be attributed to the replacement of empty pores in the AAO with a ceramic material. Notably, anodizing at 10 V, 1 °C produced a nanostructured coating with a higher maximum hardness than anodizing at 20 V, 1 °C. However, the latter exhibited increased hardness across a wide range of displacement depth.

In comparison to other substrates, **Al<sub>2</sub>O<sub>3</sub>-based** nanostructured coatings where AAO was sealed by ALD with Al<sub>2</sub>O<sub>3</sub> exhibit some of the highest hardness values (Fig. 32, curve 4). The substrate obtained by anodizing at 10 V and 1 °C had a maximum hardness of 7.2 GPa, which was measured to be higher than the previous value (Fig. 32a, curve 4).

**Al<sub>2</sub>O<sub>3</sub>-TiO<sub>2</sub> mixture-based** nanostructured coatings, where AAO was sealed by ALD with Al<sub>2</sub>O<sub>3</sub>-TiO<sub>2</sub> mixture, have the highest hardness value of 5.2 GPa when anodizing is performed at 10 V, 1 °C (Fig. 32a, curve 5). In contrast, when 20 V and 1 °C were used for anodizing, the hardness curve for the Al<sub>2</sub>O<sub>3</sub>-TiO<sub>2</sub> nanostructured coating (Fig. 32b, curve 5) behaved similarly to that of the uncoated substrate (Fig. 32, curve 1).

**Al<sub>2</sub>O<sub>3</sub>/TiO<sub>2</sub> nanolaminate-based** nanostructured coatings, in which AAO was sealed by ALD with Al<sub>2</sub>O<sub>3</sub>/TiO<sub>2</sub> nanolaminate, exhibit the same maximum hardness value and hardness curves (Fig. 32, curve 6) as the Al<sub>2</sub>O<sub>3</sub> based nanostructured coatings (Fig. 32, curve 4). The similar behavior of these two nanostructured coatings can be explained by the fact that in both instances the nano-scale pores in the AAO were sealed with the same material as the first layer of nanolaminate, which is 20 nm Al<sub>2</sub>O<sub>3</sub>.

**Table 8.** Data obtained via LSV and nanoindentation studies on bare and coated substrates with different pre-treatments and 50 nm ceramic films grown by ALD [53].

Substrate pre-treatment	ALD coating	Pitting potential $E_{pit}$ , V	Current density $j_{1V}$ , A/cm <sup>2</sup>	Coating efficiency, CE (Eq. 1)	$H_{max}$ , GPa	$Y_{max}$ , GPa
Standard	–	–0.59	0.196	–	3.0 ± 1.2	100 ± 13
Standard	TiO <sub>2</sub>	–0.53	0.157	0.20	3.3 ± 0.9	96 ± 23
Standard	Al <sub>2</sub> O <sub>3</sub>	–0.48	6.17 × 10 <sup>–2</sup>	0.68	4.1 ± 1.3	93. ± 23
Standard	Mixture*	–0.57	0.156	0.20	3.3 ± 1.4	98 ± 34
Standard	Laminate**	–0.54	6.35 × 10 <sup>–2</sup>	0.68	3.5 ± 0.8	96 ± 10
10 V anod.	–	–0.56	0.131	0.33	3.0 ± 1.3	88 ± 22
10 V anod.	TiO <sub>2</sub>	–0.45	1.45 × 10 <sup>–4</sup>	1.00	5.5 ± 1.8	102 ± 18
10 V anod.	Al <sub>2</sub> O <sub>3</sub>	N/A	1.83 × 10 <sup>–11</sup>	1.00	7.2 ± 1.8	121 ± 26
10 V anod.	Mixture*	–0.46	3.49 × 10 <sup>–3</sup>	0.98	5.2 ± 2.2	100 ± 37
10 V anod.	Laminate**	0.35	1.73 × 10 <sup>–5</sup>	1.00	6.5 ± 1.3	111 ± 17
20 V anod.	–	–0.52	0.136	0.30	2.3 ± 0.5	75 ± 11
20 V anod.	TiO <sub>2</sub>	N/A	1.33 × 10 <sup>–7</sup>	1.00	4.5 ± 1.2	95 ± 20
20 V anod.	Al <sub>2</sub> O <sub>3</sub>	0.75	6.58 × 10 <sup>–9</sup>	1.00	5.2 ± 1.6	95 ± 25
20 V anod.	Mixture*	–0.27	1.56 × 10 <sup>–3</sup>	0.99	3.0 ± 0.9	70 ± 8
20 V anod.	Laminate**	N/A	6.49 × 10 <sup>–10</sup>	1.00	5.5 ± 1.3	99 ± 19

\* Al<sub>2</sub>O<sub>3</sub>–TiO<sub>2</sub> mixture

\*\* Al<sub>2</sub>O<sub>3</sub>/TiO<sub>2</sub> nanolaminate

### 5.3.5. EIS study of nanostructured coating

The LSV (Figs. 30, 31) and nanoindentation (Fig. 32) analyses of the nanostructured coatings allowed for a reduction in the number of substrates requiring additional characterization and development. Only three recipes produced coatings that did not exhibit pitting corrosion in the LSV tests (Figs. 30, 31). In addition, the nanostructured coatings produced by anodizing at 20 V and 1 °C exhibited superior performance in general. Among the most effective corrosion-resistant coatings, the substrate anodized at 20 V and 1 °C and sealed by ALD with 50 nm nanolaminate exhibited the highest hardness (Fig. 33, curve 6). On the basis of these results presented in study III [53], EIS studies were conducted on the best-performing coating with two variations to determine its saltwater stability (Fig. 33). The nanostructured coatings were prepared by anodizing the Al alloy at 20 V and 1 °C, and then sealing the AAO layer on one sample with 50 nm nanolaminate (Fig. 33a) and on the other sample with 110 nm nanolaminate for the EIS studies (Fig. 33b). To evaluate the stability of these two coatings, EIS measurements were performed at the beginning (denoted as “0h”) and at the end of 24 h immersion (denoted as “24h”) in 0.5 M NaCl at room temperature.

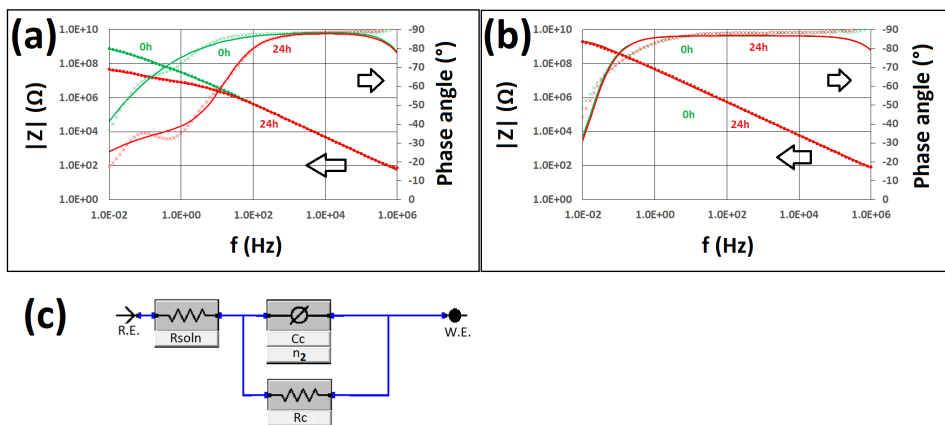


**Fig. 33.** EIS study results: Bode plots for the substrates with nanostructured coatings prepared by anodizing at 20 V, 1 °C and sealed by ALD with 50 nm (a) and 110 nm nanolaminate (b). In the Bode plots, the markers indicate experimental and modeled values. The ECM (c) was used for modeling the plot curves in b [53].

The thickness of the nanolaminate grown by ALD to seal the AAO layer has an effect on the stability of the prepared nanostructured coating, according to EIS studies (Fig. 33). Particularly, the nanostructured coating with 50 nm nanolaminate was unstable during 24 h of immersion in 0.5 M NaCl, as measured by EIS (Fig. 33a). After 24 h of immersion, the impedance ( $|Z|$ ) of the aforementioned coating had decreased at lower frequencies and no longer exhibited a linear behavior. In addition, the phase angle ( $\theta$ ) curves changed form and were only close to  $90^\circ$  for a small frequency range. The second nanostructured coating, which had been sealed with a 110 nm nanolaminate, remained stable in EIS measurements performed at the beginning and end of a 24 h saltwater immersion (Fig. 33b, Table 9). Specifically, neither the measured impedance ( $|Z|$ ) nor the phase angle ( $\theta$ ) curves changed during the 24 h immersion experiment (Fig. 33b).

**Table 9.** Calculated ECM (Fig. 33c) variables for Al alloy substrates with nanostructured coating, which was prepared by anodizing at 20 V and 1 °C and sealing with 110 nm nanolaminate (Fig. 33b) [53].

EMC variables	Coating	
	Anodized at 20 V, 1 °C and coated by 110 nm nanolaminate	
Immersion time, h	0	24
Fixed $R_{\text{soln}}$ , $\Omega \cdot \text{cm}^2$	10.0	10.0
$R_c$	$2.6 \times 10^9$	$2.4 \times 10^9$
$C_c$ , $\text{F} \cdot \text{cm}^{-2} \cdot \text{s}^{n_2-1}$	$3.7 \times 10^{-9}$	$3.7 \times 10^{-9}$
$n_2$	0.96	0.96



The impedance curve exhibits nearly linear behavior in the frequency range of  $2 \cdot 10^{-2}$ – $10^5$  Hz. The measured phase angle curve was also close to  $90^\circ$  across a wide frequency range. The ECM depicted in Fig. 33c was used to model the behavior of the second coating. The modeled values of  $R_c$ ,  $C_c$ , and  $n_2$  for the second coating did not change during the 24 h immersion test, which suggests that the coating is defect-free and does not degrade during that time in an aqueous chloride ion-containing medium (Table 9).

### 5.3.6. Salt spray testing of nanostructured coatings

The 1000 h ISO 9227 salt spray tests were conducted on uncoated and coated Al alloy substrates in study III [53], with the substrates being photographed before and after the experiment (Fig. 34).

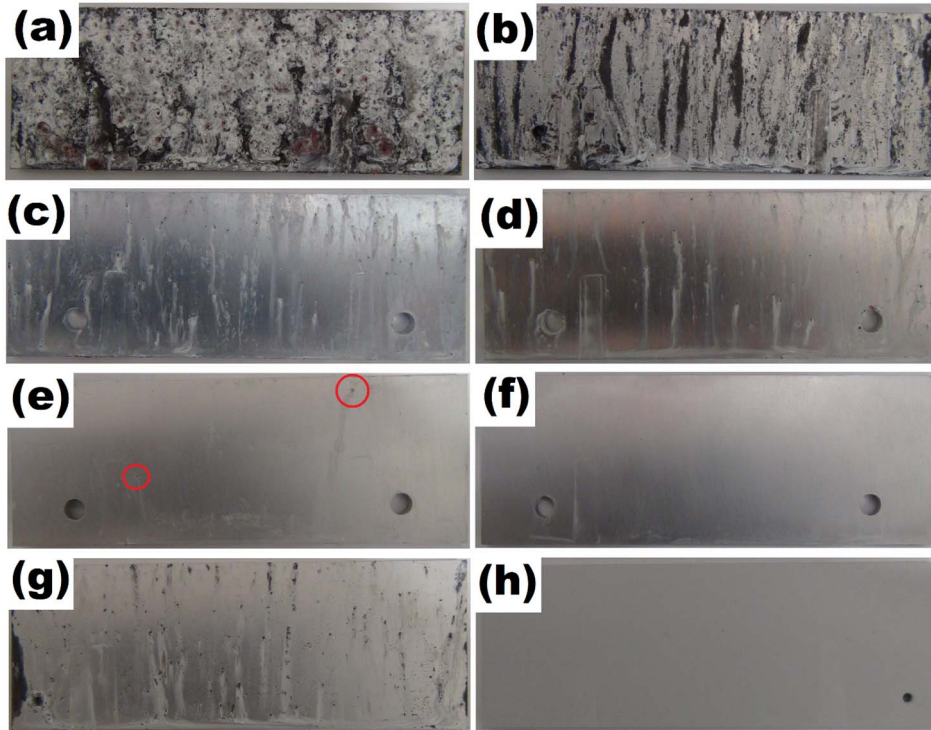


**Fig. 34.** Photos of  $40 \times 110 \text{ mm}^2$  AA2024-T3 samples after 1000 h ISO 9227 salt spray test at  $35^\circ\text{C}$  depicting a just-polished sample (a), sample just-anodized at 20 V and  $1^\circ\text{C}$  (b), sample with deposits onto the polished substrate of 50 nm nanolaminate (c) and 110 nm nanolaminate (d), sample anodized at 20 V and  $1^\circ\text{C}$  and sealed with 50 nm nanolaminate (e) and 110 nm nanolaminate (f), sample anodized at 20 V and  $1^\circ\text{C}$  following hydrothermal sealing (g), sample anodized at 20 V and  $23^\circ\text{C}$  and sealed with Rust Stop paint (h) [53].

During the 1000 h test, the **bare substrate** suffered extensive damage and was completely covered with corrosion products (Fig. 34a). The distribution of corrosion products and the presence of darker circular spots indicate that the corrosion of the alloy was more localized, as described by Boag et al. [13–15].

After the salt spray test, the **anodized substrate** (20 V and 1 °C) was also severely corroded (Fig. 34b). However, the extent of damage was smaller in comparison with the uncoated substrate (Fig. 34a) as the AAO layer hindered the corrosion process. As anticipated, the AAO layer did not provide complete corrosion protection because its pores were not sealed. This enabled corrosive species to migrate through the pores and interact with the metal substrate, accelerating the coating's deterioration.

**The nanolaminate-coated polished substrates** performed relatively well during the test, with at least 95% of the coating remaining undamaged (Fig. 34c, d). However, the coating contained numerous small corrosion sites similar in size and shape to those found on the substrate following an immersion test (Fig. 9e). After the salt spray tests, a comparison of the two substrates with 50 nm (Fig. 34c) and 110 nm (Fig. 34d) nanolaminate coatings reveals that the thicker coating exhibits slightly superior performance.

**The substrates with nanostructured coatings** obtained by anodizing at 20 V and 1 °C and sealing by ALD with 50 nm (Fig. 34e) and 110 nm (Fig. 34f) nanolaminate performed admirably in the salt spray test. In particular, the former substrate exhibited only 2 corrosion sites, whereas the latter coating was flawless. This is consistent with LSV (Fig. 30) and EIS (Fig. 33, Table 9) findings, which also indicate that the coating is defect-free and stable in a saltwater environment.

**The anodized substrate with hydrothermal sealing** showed moderate corrosion damage after the test (Fig. 34g), which is preferable to the anodized substrate without sealing (Fig. 34b). The relatively poor performance of the former substrate can be attributed to the high content of Cu in the alloy, which causes larger cavities in the AAO layer that cannot be effectively sealed by hydrothermal treatment. The distribution and number of major defects in the anodized substrate that has been hydrothermally sealed (Fig. 34g) are also comparable to those of the polished substrates with nanolaminate coatings (Fig. 34c, d).

**The anodized substrate sealed with Rust Stop paint** [62] was unaffected by the salt spray test (Fig. 34h), which is comparable to the best-performing nanostructured coating, which was made by anodizing at 20 V and 1 °C and sealing by ALD with 110 nm nanolaminate (Fig. 34f). However, the former coating has a thickness of 28 to 33 μm, whereas the thickness of the nanostructured coating, including the AAO layer, is only 2 to 4 μm.

### 5.3.7. STEM study of nanostructured coating

The STEM studies were conducted on a nanostructured coating produced by anodizing the alloy at 20 V and 1 °C, and sealing by ALD with a 110 nm nanolaminate (Fig. 35) [paper III; 53]. FIB was used to create a lamella from the

coating for this purpose. The bright field STEM image reveals the fine structure of the coating, where the pores in the AAO layer have been sealed and its surface has been covered with nanolaminate (Fig. 35a). The high-angle annular dark field image of the same region also reveals an internal nanoscale structure within the sealed AAO layer.

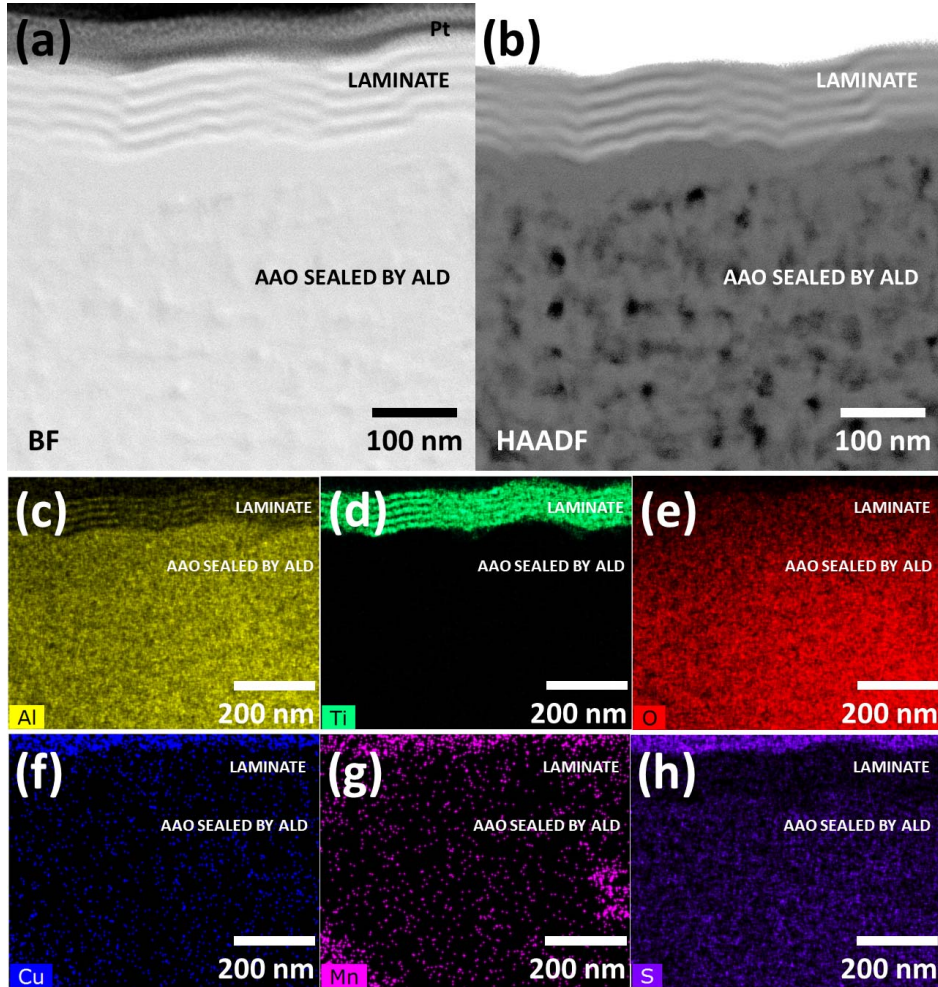


**Fig. 35.** STEM study of nanostructured coating, depicting bright field (a) and high-angle annular dark field (b) images made of a lamella prepared from the coating by FIB. STEM-EDX analysis of the same lamella indicates the distribution of Al (c), Ti (d), O (e), Cu (f), Mn (g), and S (h) in the top part of the nanostructured coating [53].

Additional studies of the lamella were conducted using STEM-EDX, which enabled mapping of the elemental distribution at the site of interest (Fig. 35c-h). Mapping the distribution of Al reveals how the AAO layer has been encapsulated by ALD with  $\text{Al}_2\text{O}_3$  and, on the coating's surface, how some of the nanolaminate's

individual layers have been formed (Fig. 35c). On the Al map, the 20 nm Al<sub>2</sub>O<sub>3</sub> first layer of the nanolaminate cannot be distinguished from the AAO. The distribution of Ti is depicted in Fig. 35d, which also demonstrates that TiO<sub>2</sub> has been mostly deposited on top of the AAO layer as part of the nanolaminate as intended. The absence of a significant Ti signal in the AAO portion of the coating confirms that the first 20 nm of Al<sub>2</sub>O<sub>3</sub> in the nanolaminate seals the majority of nano-scaled pores and prevents the entry of other species. The uniform distribution of O in the sealed AAO and nanolaminate region indicates that the nanostructured coating is devoid of significant internal cavities (Fig. 35e). The mapping of elements also provided a greater understanding of the anodization procedure (Fig. 35f–h). In particular, no Cu was detected in the AAO coating's sealed portion, indicating that Cu was successfully removed during anodization (Fig. 35f). In contrast, the higher Mn signal in certain areas of the sealed AAO layer suggests that this element is more difficult to remove via anodization (Fig. 35g). Finally, comparing the distribution of S in the nanolaminate and the sealed AAO portion of the coating demonstrates that S is introduced into the AAO layer during anodization.

### 5.3.8. ATOX testing of nanostructured coating

At the LEOX facility, the best performing nanostructured coating, which was obtained by anodizing at 20 V and 1 °C, and sealing by ALD with a 110 nm nanolaminate, was examined with energetic atomic oxygen. Visual inspection and photographs taken prior to (Fig. 36a) and subsequent to (Fig. 36b) the test did not reveal any significant changes to the nanostructured coating. Different lighting conditions were used to photograph the sample, which resulted in color variation. The only significant modification to the sample was the removal of the blue market stripe, which is essentially a thin film of organic material [63] and thus more susceptible to atomic oxygen than a ceramic coating.

In contrast to visual observation, HR-SEM studies proved to be more informative as the comparison of high-resolution secondary images of the untested (Fig. 36c) and tested (Fig. 36d) surface reveals damage caused by atomic oxygen that was invisible to the naked eye. The HR-SEM studies depicted in Fig. 36d reveal the formation of 5–10 nm microcavities on the surface of the sample during the ATOX test. In addition, note that the surface of the nanostructured coating is sufficiently conductive for HR-SEM studies owing to the presence of amorphous TiO<sub>2</sub> produced by ALD. During the HR-SEM studies, we also observed that it was much simpler to obtain a high-resolution image of the tested surface than of the untested surface. This could be explained by the increased surface conductivity observed during the ATOX examination. Because the sole conductive component of the nanostructured coating was TiO<sub>2</sub>, which was also the top layer of the nanolaminate, it was necessary to examine its evolution in greater detail.

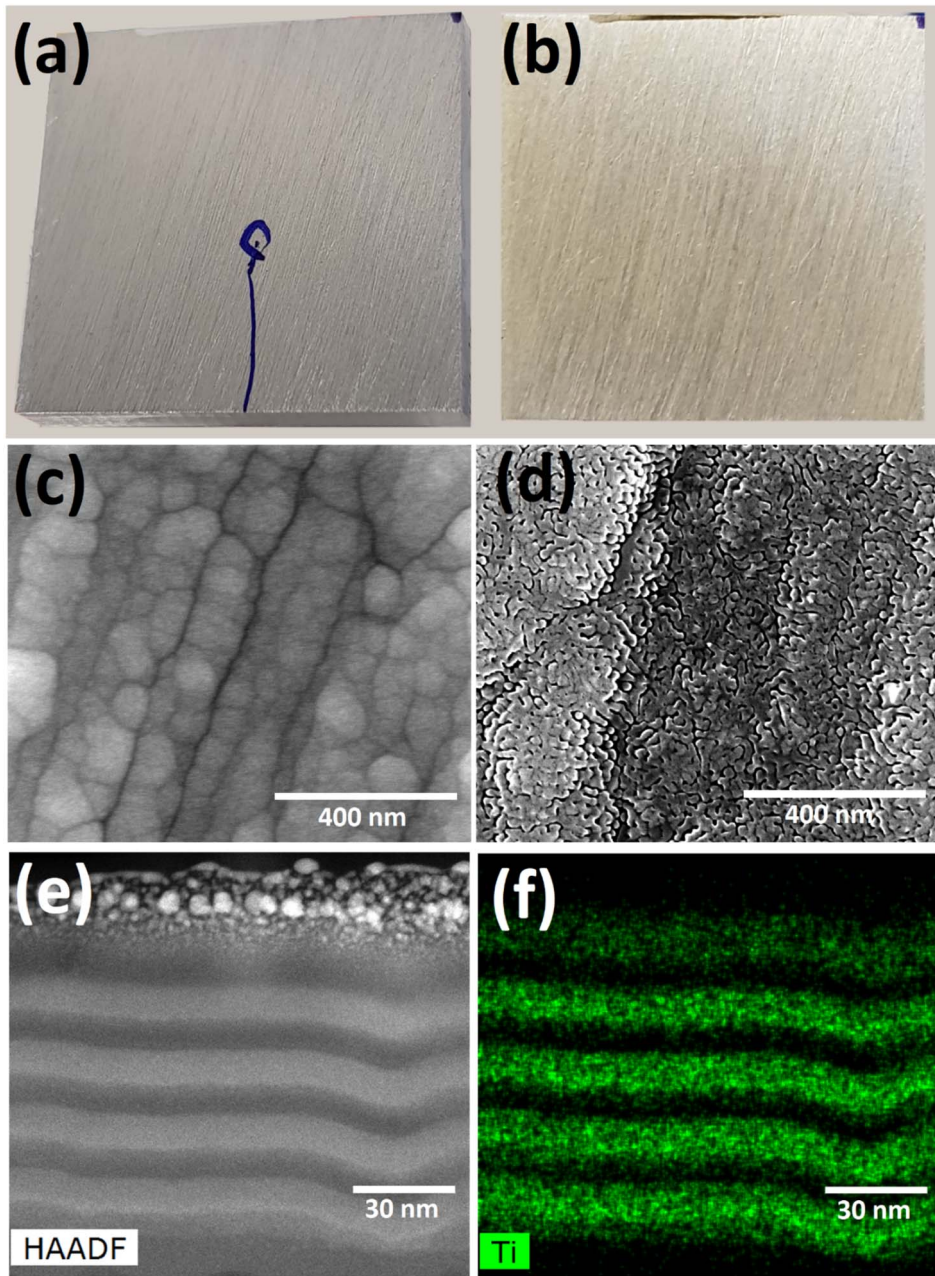


**Fig. 36.** Photos, SEM, and STEM images of an as-prepared and ATOX-tested nanostructured coating, made by anodizing at 20 V following enhancement by ALD by adding a 110 nm thick nanolaminate: a) photo of the substrate before ATOX test and b) after ATOX test, c) HR-SEM image of the nanostructured coating before ATOX test and d) after ATOX test, e) STEM high-angle annular dark field image of the lamella of the nanostructured coating after ATOX test and f) with an overlay of the Ti distribution map measured by EDX. A local Pt mask was used for surface protection during the preparation of the lamella by FIB [53].

Therefore, SEM-FIB was utilized to prepare a lamella of the examined nanostructured coating for HR-TEM research (Fig. 36e, f). These studies demonstrated that the changes caused by high-energy atomic oxygen were restricted to the very top layer of the nanolaminate on the nanostructured coating comprising TiO<sub>2</sub>. However, the precise cause of the change in the surface morphology of the tested sample is not clear. One possible explanation is the partial crystallization of the top TiO<sub>2</sub> layer due to exposure to energetic atomic oxygen. However, no nanocrystallites were detected in the surface layer using TEM. It is also possible that the mechanical properties of the TiO<sub>2</sub> top layer of the nanolaminate grown by ALD are not uniform. On a nanometric scale, this would result in softer regions being sputtered away faster than nearby regions that are harder. In any case, it is difficult to examine either of these possibilities in the TEM image because the upper portion of the top layer was obscured by platinum particles during lamella preparation.

Based on the evidence that atomic oxygen has a negligible effect on the coating and that the coating retains its conductivity, it is likely that the developed nanostructured coating can be considered for use in low Earth orbit.

### 5.3.9. Radiation behavior of the nanostructured coating

By irradiating the surface with 30 keV primary electrons and measuring the resulting spectrum, the radiation behavior of bare and coated substrates was studied (Fig. 37). These studies demonstrate that the application of a nanostructured coating to an Al alloy reduces the intensity of secondary electromagnetic radiation, particularly the bremsstrahlung portion. As the nanostructured coating has a lower average atomic number than the Al alloy, these results are in good accordance with Kramer's law (Al<sup>13</sup>, Cu<sup>29</sup>, Mg<sup>12</sup>). As the micrometric AAO layer is sealed with Al<sub>2</sub>O<sub>3</sub> by ALD, the nanostructured coating is predominantly composed of Al<sub>2</sub>O<sub>3</sub> (Al<sup>13</sup>, O<sup>8</sup>) (Fig. 29d). In contrast, the Al alloy is composed of elements with atomic numbers greater than oxygen (Table 2).

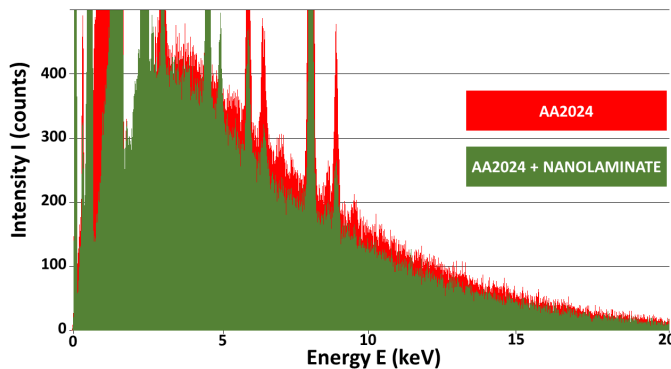


**Fig. 37.** EDX spectra of the bare substrate and the one with nanostructured coating; primary electron energy was 30 keV [53].

Owing to its low concentration, the Ti content in the nanostructured coating has a negligible effect on the spectrum. Ti is only found in the nanolaminate on the top portion of the coating, which contains approximately 50 nm of TiO<sub>2</sub>. On the basis of these findings, the use of nanostructured coatings on Al alloys may improve their radiation damage mitigation performance. This is especially useful for satellites whose missions take them through the Van Allen belts. In the actual application environment, the energies of the charged particles of cosmic radiation (protons, alpha particles, electrons, and ions) are several orders of magnitude higher than the energy of electrons (30 keV) used in SEM studies; however, Kramer's law still holds true.

### 5.3.10. Practical implementation of nano-coatings

Thin functional coatings, such as nanolaminates and nanostructured coatings, can be used to improve the properties of aluminum alloys, as demonstrated in these studies. In particular, the use of electrochemical pre-treatments and ALD enables the application of thin coatings to substrates with complex three-dimensional shapes without significantly increasing their weight or size. The selection of the precise coating depends on the application, examples of which are depicted in Fig. 38 and discussed below.

**Nanolaminates** can be applied to high-precision aluminum alloy components to significantly improve their corrosion resistance with only a mechanical surface finish and organic solvent cleaning as pretreatment (Figs. 8–11, 34). In these studies, a 50–250 nm thick nanolaminate could be grown using ALD in an industrial reactor within an 8 h workday, making it suitable for commercial applications. The nanolaminate is chemically stable in moist chloride-containing environments and suffers minimal changes when exposed to a direct flux of atomic oxygen (Fig. 36) at low Earth orbit, making it suitable for use in space and terrestrial applications requiring the preservation of high component precision. In Fig. 38a, we demonstrate how the nanolaminate was applied to a substratum of millimeter-scale precision and high precision. This component will be in direct contact with other metal parts in its actual application, which may increase the risk of galvanic corrosion. Owing to the small size of these substrates, a commercial ALD reactor can coat hundreds or even thousands of them simultaneously. This allows the performance of these high-precision parts to be improved with a negligible increase in unit cost. For example, if coating a deposition service costs 2000 € and 1000 components can be coated simultaneously, the price of each component would increase by only 2 €.

**Nanostructured coatings** can be used in high-performance applications where nanolaminates perform inadequately. The use of potentiostatic anodizing in the first step of preparing nanostructured coatings adds additional cost and effort to the overall coating process; however, it enables a much higher coating efficiency without significantly affecting the substrate dimensions. Specifically, the nanostructured coatings have a thickness of only 2 to 4 μm (Fig. 29). The

potentiostatic anodizing process is also simple and inexpensive to implement in a practical setting. Moreover, when anodizing small substrates, temperature control can be easily achieved by utilizing an external ice bath surrounding the anodizing bath to maintain the electrolyte at 1 °C. The choice of material for ALD sealing permits the modification of the properties of the nanostructured coating. By sealing AAO with Al<sub>2</sub>O<sub>3</sub>, for instance, insulating coatings can be created, which is advantageous for creating a dielectric barrier or simply a hard surface. Conversely, sealing the nanoscale pores of AAO with Al<sub>2</sub>O<sub>3</sub> and applying a nanolaminate on top will produce a nanostructured coating that benefits from its dielectric properties and hardness while also providing additional chemical stability for use in moist environments and a semiconductive surface to reduce charging in space. If it is necessary to create an overall more conductive coating, then TiO<sub>2</sub> can be used to seal the nanoscale pores in the AAO instead of Al<sub>2</sub>O<sub>3</sub>. The only potential disadvantage of using potentiostatic anodization at low temperatures as a pre-treatment is the formation of cracks in the AAO layer and the limited dissolution of IMP residues. In our study, we mitigated this potential problem by coating the AAO with 20 nm of Al<sub>2</sub>O<sub>3</sub> and then 90 nm of nanolaminate. This type of nanostructured coating was also used to cover the satellite components shown in Fig. 38b–e for a variety of purposes.

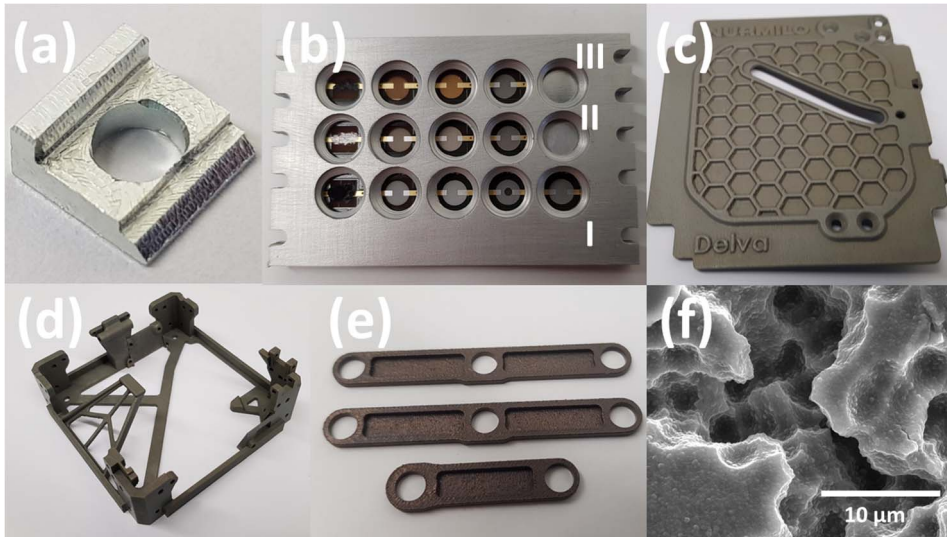


**Fig. 38.** Use of nanolaminate and nanostructured coatings in space technology. Photos of satellite components (a–e) with nanolaminate (a) and nanostructured coating (b–e) that will be used on WISA Woodsat (a,c–e) and ESTCube-2 (b). Surface of the nanostructured coating on 3D printed aluminum alloy sample is depicted in SEM image (f) [53].

On ESTCube-2, the nanostructured coating was applied to an aluminum  $65 \times 41 \times 3 \text{ mm}^3$  cover panel (Fig. 38b, I) of the materials testing module, which exposes the tested materials to atomic oxygen in a low Earth orbit through holes (such as sites II and III). In this module, the nanostructured coating on a 0.1 mm foil was



evaluated at site II and compared to the performance of an uncoated foil at [site III](#). Visual inspection of the coated cover panel revealed no flaws, and the sample in the salt spray test resembled the AA2024-T3 sample with a nanostructured coating ([Fig. 34f](#)).

On WISA Woodsat, a nanostructured coating was applied to over 50 3D-printed aluminum parts. These components consist of panels ([Fig. 38c](#)), the main frame structure of the cube satellite ([Fig. 38d](#)), and components of the mechanism ([Fig. 38e](#)) that extracts the camera from the satellite to capture images of its outer surface while in orbit. A coating is used in the extraction mechanism to prevent cold welding in space. Assembly of the coated components did not reduce mobility. Additional SEM analysis of the surface revealed that the coating was free of defects and matched the surface morphology of the 3D-printed substrate ([Fig. 38f](#)).

### 5.3.11. Optimizing the ALD process for preparing coatings on Al alloys

The possibilities of using ALD for preparing protective coatings on Al alloys is quite limited owing to various reasons:

- The temperature at which the ALD process grows the coating must be compatible with the alloy being treated. This is especially important with high-performance alloys such as AA2024-T3, for which the ALD process temperature must be  $< 150$  °C to prevent the degradation of the mechanical properties of the alloy [1–5]. In the case of certain other Al-alloys, slightly higher temperatures may be permitted for ALD.
- It is desired that the ALD-grown coating be amorphous. This is significant because the grain boundaries in crystalline films provide a pathway for corrosive species, which reduces the coating's effectiveness [31]. Therefore, the ALD temperature must be kept low to prevent the crystallization of the coating materials, particularly  $\text{TiO}_2$  (sub)layers.
- In terrestrial applications, an insulating coating is frequently preferred. This is due to the fact that aluminum alloys are particularly susceptible to corrosion in the presence of nobler substances [42]. An insulating coating would effectively prevent galvanic coupling by preventing the flow of electrons between the two alloys.
- When preparing nanostructured coatings, the precursor molecules must be as small as possible in order to diffuse rapidly in and out of the pores of the AAO layer during the ALD process, which occurs at a predetermined temperature and pressure.
- The precursors used in the ALD process must also be sufficiently reactive within the alloy-specified temperature range. At the start of the ALD process, the precursors must not cause corrosion of the substrate material.

- Only the thermal ALD process can be used to seal the narrow and long pores of the AAO and to coat substrates with intricate three-dimensional geometries. Therefore, it is not possible to boost surface reactions during ALD by employing plasma or other physical excitation mechanisms.
- For the technology to be commercially viable, the cost of the precursors utilized in the ALD process must be relatively low.

### 5.3.12. Benefits of nanostructured coating in the space industry

In the case of satellites ESTCube-2 and WISA Woodsat, the use of the novel nanostructured coating was justified owing to several reasons:

- ✓ The nanostructured coating has a low thickness of 2 to 4 μm (Fig. 29) and consequently has an insignificant effect on the dimensions of high-precision components than a thick AAO layer obtained by conventional anodizing alone.
- ✓ The nanostructured coating preparation technology permits its application to substrates with intricate three-dimensional shapes (Fig. 38d) and threaded holes. This is not possible with the majority of other coating processes, and conventional anodizing may damage the threads in the holes.
- ✓ The top layer of the nanostructured coating contains amorphous TiO<sub>2</sub>, which has a higher conductivity than Al<sub>2</sub>O<sub>3</sub> and helps to mitigate the space charging problem. Additionally, the coating retains its conductivity even after prolonged exposure to atomic oxygen (Fig. 36d).
- ✓ The coating prevents corrosion when exposed to corrosive environments (Fig. 34f) and even when anodic potentials are applied (Fig. 30d, curve 4). This is significant because satellite components are typically assembled in the open air and stored for several months before shipment to space. In addition, satellites are comprised of numerous metals and components, which may induce galvanic coupling and accelerate the corrosion of unprotected aluminum components. This corrosion may cause spacecraft components to become immobile and lose their function. Coatings can reduce the accumulation of corrosion products, which would otherwise contribute to undesirable outgassing in space.
- ✓ It is anticipated that the nanostructured coating will prevent the cold welding of moving parts, allowing them to continue functioning in space. This is possible because the coatings have sufficient hardness and adhesion to the aluminum substrate to resist wear at the joints of moving components. To compare the performance of nanostructured coatings with existing solutions, such as coatings obtained by plasmaelectrolytic oxidation, additional tests are required in this field.

- ✓ By its very nature, the nanostructured coating is suitable for use in space because it is non-toxic and does not contribute to outgassing. In particular, the preparation of the coating required the removal of a thin layer of the alloy's surface along with any contaminants. Second, the ALD process was performed in a vacuum, resulting in a high-quality ceramic external layer that sealed all pores and other surface features that could potentially contribute to outgassing in space's vacuum.

## CONCLUSIONS

In this study, technologies were developed and evaluated for the preparation of novel nanostructured coatings for the protection of Al-alloys (e.g. AA2024-T3) against corrosion for various applications in which the alloy components must operate in environments containing chloride ions or in space under intense atomic oxygen bombardment. In the first step, the surface layer of the Al-alloy was converted into nanoporous aluminum oxide or a nanometric dense aluminum oxide base layer via anodizing or low potential electrochemical treatment, respectively. In the second step, atomic layer deposition was used to seal and coat the porous anodic aluminum oxide layer; the LET-processed aluminum oxide layer was covered with an ALD top layer because the base layer does not require sealing. Systematically, the coatings were examined via immersion, salt spray tests (ISO 9227), diverse electrochemical techniques, and a stream of energetic atomic oxygen. On the basis of studies and tests, industrial technologies were developed to produce high-performance coatings for a variety of applications, including the automobile, aerospace, and space industries of the next generation.

To develop a corrosion-resistant coating for Al-alloys such as AA2024-T3, it was necessary to first evaluate the performance of various ALD coatings on polished metal substrates and determine their failure mechanism.

- The corrosion resistance of Al-alloy could be improved by applying a protective top layer of  $\text{Al}_2\text{O}_3$ ,  $\text{TiO}_2$ ,  $\text{Al}_2\text{O}_3$ - $\text{TiO}_2$  mixture, or  $\text{Al}_2\text{O}_3/\text{TiO}_2$  nanolaminate via atomic layer deposition (ALD). After undergoing corrosion tests, the nanolaminate had the lowest number of individual corrosion sites among these materials.
- Increasing the thickness of the nanolaminate coating on polished Al-alloy substrates could improve its performance. However, 250–500 nm laminate coatings are impractical for industrial applications, and even 500 nm coatings cannot provide complete protection.
- The failure of ALD coatings on polished Al-alloy substrates is dependent on the condition of the initial metal surface, which is affected by contaminants as well as the naturally occurring intermetallic particles (IMP-s) in the alloy, which can cause localized galvanic corrosion in the open air when partially exposed. To the best of our knowledge, this was demonstrated for the first time.
- The local failure of coatings at IMP-s is likely due to the IMP | coating interface, which differs from the surrounding area, has a high Al content and is therefore covered by natural aluminum oxide, and adheres well to the first layer of the laminate ( $\text{Al}_2\text{O}_3$ ). The vicinity of IMP-s may also contain corrosion products that reduce the adhesion of the substrate to the ALD-applied coatings.

Further, the impact of electrochemical pre-treatments on the Al-alloy surface and the performance of protective coatings was investigated. Al-alloy substrates were

electrochemically and potentiodynamically treated in sulfuric acid and a boric/sulfuric acid mixture for this purpose, and the current was measured during the cycling of the potential.

- The plots obtained from the electrochemical pre-treatment of the Al-alloy demonstrated that IMP-s were already eliminated at low potentials.
- In the potentiodynamic pretreatment, the AAO layer's thickness could be adjusted. A low potential treatment prevented the formation of a thick AAO layer while removing IMP-s from the surface. The aluminum oxide layer obtained through the LET process had a thickness of < 10 nm. When using higher potentials for potentiodynamic pre-treatment, the obtained AAO layer thickness was dependent on the electrolyte and was  $\leq 0.5 \mu\text{m}$  and  $\leq 2 \mu\text{m}$  for BSA and SA, respectively.
- Corrosion tests using linear sweep voltammetry and immersion demonstrated that the electrochemical pre-treatment of the Al-alloy significantly improves the performance of the final coating—the best coating withstood the immersion test for 7152 h (298 days) with no significant degradation. The increase in performance is attributable to the elimination of near-surface IMP-s, the stripping of the surface layer along with potential contaminants, and the overall transformation of the inhomogeneous surface into a homogeneous AAO.
- Using a low potential electrochemical alloy surface pre-treatment, a nanometric dense aluminum oxide base layer was formed, which was then coated by an ALD top layer, allowing for the preparation of the thinnest, submicron-thick nanostructured protective coating. This coating provided limited corrosion protection; however, it can be used in limited corrosive environments because it performed significantly better than ALD coatings alone.

For practical industrial applications, a study was conducted on how to create micrometric nanostructured coatings using the developed method. To accomplish this, the anodizing process was conducted using a potentiostatic process at lower temperatures, which was accomplished by surrounding the anodizing bath with an external ice bath. In addition, different materials were deposited onto the anodized substrates by altering the precursor pulse times in the ALD process.

- Anodizing at low temperatures in sulfuric acid effectively eliminated near-surface IMP-s and produced a less porous AAO than anodizing at room temperature.
- The thickness of the AAO layer was approximately 1  $\mu\text{m}$  for substrates anodized at 10 V and between 2 and 4  $\mu\text{m}$  for samples anodized at 20 V.
- Corrosion tests, Ag electrodeposition, and SEM-FIB studies demonstrated that anodized substrates are most susceptible to corrosion at sites where larger micrometric IMP-s were removed during the anodization process. Such locations contained extensive cracks that allowed corrosive species access to the metal substrate.

- By utilizing the proper precursor pulse times in the ALD process, it was possible to completely seal the pores in the AAO layer and produce various nanostructured coatings.
- The optimal coating was obtained by a) anodizing the Al-alloy substrate at 20 V and 1 °C, b) sealing the pores in the AAO layer with 20 nm Al<sub>2</sub>O<sub>3</sub> at long precursor pulse times, and c) applying an additional 90 nm laminate by ALD with shorter precursor pulse times to cover the surface and seal major cracks. The performance of this coating in a 1000 h ISO 9227 salt spray test was comparable to that of one of the best corrosion-resistant paints commercially available, as no corrosion occurred on the coated substrates during the test.
- The top layer of the nanostructured coating, the Al<sub>2</sub>O<sub>3</sub>/TiO<sub>2</sub> nanolaminate, is nearly impervious to atomic oxygen, as demonstrated by additional ESA tests and subsequent STEM research. Consequently, the nanostructured coating may also be effective for applications in low Earth orbit.

## SUMMARY IN ESTONIAN

### Nanostruktuursed pinnakatted auto-, lennu- ja kosmosetööstusele

Käesoleva doktoritöö raames töötati välja meetodid nanostruktuursete katete valmistamiseks, millega saab kaitsta alumiiniumsulameid (nt AA2024-T3) korrosiooni eest niisketes kloori sisaldavates kasutuskeskkondades ning atomaarse hapniku eest kosmoses. Tõhusate katete valmistamine toimub kahes etapis, kus esmalt töödeldakse pinda elektrokeemiliselt, millele järgneb katmine keraamilise materjaliga aatomkihtsadestuse meetodil. Katete arendamisel viidi läbi süsteematilised uuringud erinevate korrosioonitestidega, milleks kasutati immersiooni korrodeerivas keskkonnas, soolaudu kambrit (ISO 9227), elektrokeemilisi meetodeid ja energeetilist atomaarset hapniku. Uuringute raames arendati välja katted erinevate rakenduste jaoks auto-, lennu- ja kosmosetööstuses.

Kaitsekatete arendamiseks alumiiniumsulamitele nagu näiteks AA2024-T3 oli esmalt tarvis uurida erinevate aatomkihtsadestatud katete vastupidavust mehaaniliselt töödeldud ja seejärel puhastatud sulami pinnal ning saada aru katete lagunemine mehhanismidest;

- Aatomkihtsadestatud  $\text{Al}_2\text{O}_3$ ,  $\text{TiO}_2$ ,  $\text{Al}_2\text{O}_3\text{-TiO}_2$  segu ja  $\text{Al}_2\text{O}_3/\text{TiO}_2$  nanolaminaat tõstis oluliselt sulami vastupidavust korrosioonile. Parimaks osutus nanolaminaat, mille korral ilmsid korrosioonitestides vaid üksikud defektid.
- Aatomkihtsadestatud nanolaminaadi kaitsevõime sõltus tema paksusest. Nimelt tagasid 250–500 nm paksused katted oluliselt parema kaitse sulamile korrosiooni eest kui 50–100 nm paksused katted. Samas oli 250–500 nm paksuste katete valmistamise aeg liiga pikk praktiliseks kasutuseks tööstuses.
- Aatomkihtsadestatud katete vastupidavus sõltus sulami pinna kvaliteedist, mida mõjutas nii lokaalne mustus kui ka sulamis esinevad suuremad mikrokoopilised metallifaasid, mis paljastusid metalli pinnal. Selliste paljastunud metallifaaside juures leiti ka lokaalse galvaanilise korrosiooni poolt tekitatud korrosiooniprodukte.
- Aatomkihtsadestatud kaitsekatete lokaalne lagunemine metallifaaside piirkonnas on ilmselt seotud metallifaasi ja katte vahelise piirpinnaga, mis erineb oluliselt ümbritsevast alast. Enamus sulami maatriksist on kaetud naturaalse alumiiniumoksiidiga, millel on hea adhesioon nanolaminaadi esimese kihiga, milleks on samuti  $\text{Al}_2\text{O}_3$ . Pinnale ulatuvate metallifaaside puhul on aga tegu suurema vasesisaldusega alaga. Samuti võib metallifaaside pinnal ja ümber esineda korrosiooniprodukte õhu käes toimunud lokaalsest galvaanilisest korrosioonist, mis nõrgendab katete adhesiooni.

Järgmisena uuriti elektrokeemilise töötamise mõju sulami pinnale ning aatomkihtsadestatud kaitsekatete vastupidavusele. Selleks töödeldi alumiiniumsulamit potentsiodünaamiliselt väävelhappes ja väävelhappe/boorhappe segus, mõõtes potentsiaali muutmise vältel voolutugevust.

- Mõõdetud voltamperogrammidele selgus, et metallifaaside eemaldamine toimus juba madalate potentsiaalide juures.
- Elektrokeemilise töötlemise tulemusena saadud alumiiniumoksiidi kihi paksust saab reguleerida, kasutades sobivaid parameetreid ning lahuseid. Potentsiodünaamiline eeltöötlus madalatel potentsiaalidel oli tõhus metallifaaside eemaldamiseks kuid samas ei tekitanud paksu alumiiniumoksiidi kihti. Sellisel töötlemisel tekkinud oksiidikihi paksus oli <math><10\text{ nm}</math>. Potentsiodünaamiline eeltöötlus kõrgemal potentsiaalidel tekitas paksema oksiidikihi, mille paksus sõltus lahusest. Oksiidikihi paksus oli väävelhappe puhul  $\leq 2\ \mu\text{m}$  ja väävelhappe/boorhappe segu korral  $\leq 0.5\ \mu\text{m}$ .
- Korrosioonitestid lineaarse voltamperomeetria meetodil ja immersioonil soolalahuses näitasid, et kõrgemal potentsiaalidel läbiviidud potentsiodünaamilise eeltöötlemise kasutamine enne nanolaminaadi aatomkihtsadestamist tõstis oluliselt lõpliku katte vastupidavust korrosioonile. Parima kattega katsekeha pidas hästi vastu 7152 h (298 päeva) pikkuses immersioonitestis. Kaitsekatte hea sooritus oli ilmselt tingitud pinnalähedaste metallifaaside eemaldamisest, reostatud pinnakihi eemaldamisest ning ebahomogeense sulami pinna konverteerimisest homogeenseks anoodseks alumiiniumoksiidiks.
- Potentsiodünaamiline eeltöötlus madalatel potentsiaalidel enne katmist nanolaminaadiga aatomkihtsadestuse meetodil võimaldas saavutada oluliselt parema vastupidavusega katteid kui lihtsalt mehaaniline eeltöötlus koos puhastamisega. Sellised katted sobivad rakenduste jaoks, kus ei ole tegu väga korrodeeriva keskkonnaga.

Lõpuks uuriti võimalusi mitme mikroni paksuste nanostruktuursete katete valmistamiseks praktiliste tööstuslike rakenduste jaoks. Selleks viidi potentsiostaatiline anodeerimise protsess läbi madalal temperatuuril, mis saavutati anodeerimisvanni ümbritseva jäävanni abil. Anodeerimise teel saadud oksiidikihis olevad poorid täideti ja kaeti seejärel aatomkihtsadestuse meetodil erinevate keraamiliste materjalidega, varieerides lähteainete pulsiaegu.

- Anodeerimine madalal temperatuuril väävelhappes eemaldas tõhusalt pinnalähedased metallifaasid ning tekitas oksiidikihi, mis oli vähem poorne kui toatemperatuuril anodeeritud katsekehal.
- Saadud oksiidikihi paksus oli anodeerimise potentsiaali 10 V kasutamisel  $\sim 1\ \mu\text{m}$  ning 20 V korral 2–4  $\mu\text{m}$ .
- Korrosioonitestid, elektrokeemiline hõbeda sadestamine ning fokuseeritud ioonkiirega tekitatud ristlõigete uuringud skaneeriva elektronmikroskoobiga näitasid, et anodeeritud sulamid olid kõige tundlikumad korrosioonile kohtades, kust olid anodeerimise protsessis eemaldatud suuremad mikroskoopilised metallifaasid. Sellistes kohtades esinesid ka mikroskoopilised mõrad, mis ulatusid kuni metallini ja tagasid seeläbi vaba tee korrodeerivatele ainetele.



- Anodeeritud katsekehade oksiidikihis olevate pooride täieliku täitmisega ALD meetodil saavutati erinevad nanostruktuursed katted.
- Parim nanostruktuurne kate saavutati alumiiniumsulamile selle a) anodeerimisel 20 V, 1 °C juures, millele järgnes b) oksiidikihi pooride täitmine aatomkihtsadestuse meetodil 20 nm alumiiniumoksiidiga ning seejärel c) täiendava 90 nm nanolaminaadi aatomkihtsadestamine. Saadud kate vastupidavus 1000 h kestnud ISO 9227 soolaudu testis oli võrreldav ühe parima kommertsiaalse korrosioonivastase värviga, mis oli samuti kantud anodeeritud pinnale. Kumbki kaetud katsekeha ei korrodeerunud testis kuid uudne nanostruktuurne kate oli kümneid kordi õhem kui kommertsiaalse värviga saavutatud kate.
- Parimat nanostruktuurset katet testiti Euroopa Kosmoseagentuuris energetilise atomaarse hapniku vooga, kus simuleeriti 1 aastast kokkupuudet kosmose keskkonnaga madalal orbiidil. Testi läbinud kate ristlõike uuringud läbi- valgustava elektronmikroskoobiga näitasid, et atomaarne hapnik ei kahjusta Al<sub>2</sub>O<sub>3</sub>/TiO<sub>2</sub> nanolaminaati, mille tõttu võib nanostruktuurne kate sobida hästi ka rakenduste jaoks madalal orbiidil.

## ACKNOWLEDGEMENTS

First and foremost, I am grateful to my supervisor Prof. Väino Sammelselg for his support and guidance during my PhD studies. It has been a fascinating to see the rise and the days of glory of the Laboratory of Thin Film Technology, where the team assisted and guided me during the whole journey. For that I am very thankful to Jaan Aarik, Kaupo Kukli, Lauri Aarik, Jekaterina Kozlova, Tauno Kahro, Aivar Tarre, Peeter Ritslaid, Taivo Jõgiaas, Hugo Mändar, Harry Alles, Helle-Mai Piirsoo, Kaisa Aab, Elyne Aaviksoo, Martin Neitsov, Aleksandr Nikolajev, Mailiis Pala, Kaspar Roosalu, Margus Marandi, Raul Rammula, Alma-Asta Kiisler, Aarne Kasikov, Peep Adamson, Aleks Aidla, Tõnis Arroval, Arnold Rosental, Rando Saar, Arvo Tõnisoo, Tanel Tätte, Joonas Merisalu, Kristjan Kalam and Mihkel Rähn. For the electrodeposition of Ag onto anodized substrates, I thank Elo Kibena Põldsepp. In order to bring the results of this work closer to space, I also express my gratitude to external partners: Johanna Wessing (ESA), Andris Slavinskis and his crew (ESTCube), Samuli Nyman (WISA Woodsat) and Marko Pudas (Picosun Oy).

During the PhD studies I was introduced to science-based business, where I had the pleasure to actively collaborate with Uno Mäeorg, Sven Lilla, Siim Kinnas, Jane Luht, Meeri Visnapuu, Triinu Lööve, Aivar Pere, Kristel Reim and Toomas Noorem.

This work has been financially supported by Graduate School of Doctoral Studies in Estonia: “Functional materials and technologies” (project 1.2.0401.09-0079), the Estonian Ministry of Education and Research by granting the projects IUT2–24, TLTFY14054T, PSG448, PRG4, SLTFY16134T and by the EU through the European Regional Development Fund under project TK141 (2014–2020.4.01.15-00). The atomic oxygen testing was performed in the framework of the “Announcement of opportunity for atomic oxygen in the ESTEC Materials and Electrical Components Laboratory/ESA-TECQE-AO-013375),” through a collaboration with Picosun Oy.

## REFERENCES

- [1] C. R. Brooks, Heat Treatment, *Structure and Properties of Nonferrous Alloys*, American Society for Metals, Metals Park, Ohio, 1982. pp. 121–137.
- [2] J. R. Davis (Ed.), *ASM Specialty Handbook. Aluminum and Aluminum Alloys*. Davis & Associates, ASM International: 1993. J.R. Davis (Ed.), Corrosion of Aluminum and Aluminum Alloys. ASM International: 1999, 24 PP; and S.D. Cramer and B.S. Covino, Jr. (Eds.) ASM Handbook, Vol. 13B, Corrosion: Materials (#06508G). ASM International: 2005, PP. 651.
- [3] *Structure and properties of nonferrous alloys*, vol. ed.: K. H. Matucha, Weinheim Publ.: New York, Basel, Cambridge, Tokyo. Materials science and technology, vol. 8. VHC, 1996. PP. 213–276.
- [4] G. E. Totten, D. S. MacKenzie, *Handbook of Aluminum, volume 2, Alloy production and Materials Manufacturing* (2003).
- [5] [dataset] Material Property Data (ASM MatWeb) for 1000 – 7000 series aluminum alloys, AA2024-T3 and AISI 316. Keywords for search: 1000 Series Aluminum, 2000 Series Aluminum, 3000 Series Aluminum, 4000 Series Aluminum, 5000 Series Aluminum, 6000 Series Aluminum, 7000 Series Aluminum, AA2024-T3, AISI 316, Epoxy/Carbon Fiber Composite. <http://www.matweb.com> (last visited 19.05.2022).
- [6] B. D. Dunn, The Corrosion Properties of Spacelab Structural Alloy Aluminum 2219-T851 (ESA STR-212, 1984). ESA Communication Production Office, ESTEC, Noordwijk, The Netherlands. [http://esmat.esa.int/Publications/Published\\_papers/ESA\\_STR-212.pdf](http://esmat.esa.int/Publications/Published_papers/ESA_STR-212.pdf) (last accessed 23.03.2022).
- [7] A. M. Pereira, G. Pimenta, B. D. Dunn, Assessment of Chemical Conversion Coatings for the Protection of Aluminum Alloys A Comparison of Alodine 1200 with Chromium-Free Conversion Coatings (ESA-STM-276, 2008). *ESA Communication Production Office*, ESTEC, Noordwijk, The Netherlands. [http://esmat.esa.int/Publications/Published\\_papers/ESA-STM-276.pdf](http://esmat.esa.int/Publications/Published_papers/ESA-STM-276.pdf) (last accessed 23.03.2022).
- [8] EU hydrogen policy. Hydrogen as an energy carrier for a climate-neutral economy. [https://www.europarl.europa.eu/RegData/etudes/BRIE/2021/689332/EPRS\\_BRI\(2021\)689332\\_EN.pdf](https://www.europarl.europa.eu/RegData/etudes/BRIE/2021/689332/EPRS_BRI(2021)689332_EN.pdf) (last accessed 15.02.2022).
- [9] S. Kramer, D. Mosher, Here’s how much money it actually costs to launch stuff into space. *Tech Insider*. <https://www.businessinsider.com/spacex-rocket-cargo-price-by-weight-2016-6>.
- [10] O. Zeynali, D. Masti, S. Gandomkar, Shielding protection of electronic circuits against radiation effects of space high energy particles. *Advances in Applied Science Research* 3 (2012) 446–451. <https://www.primescholars.com/articles/shielding-protection-of-electronic-circuits-against-radiation-effects-of-spacehigh-energy-particles.pdf>.
- [11] D. P. Engelhart, E. A. Plis, D. Ferguson, W. R. Johnston, R. Cooper, R. C. Hoffmann, Space Plasma Interactions with Spacecraft Materials. *Plasma Science and Technology – Basic Fundamentals and Modern Applications* (2018). <http://dx.doi.org/10.5772/intechopen.78306>.
- [12] A. Boag, A.E. Hughes, N.C. Wilson, A. Torpy, C.M. MacRae, A.M. Glenn, T.H. Muster, How complex is the microstructure of AA2024-T3?, *Corros. Sci.* 51 (2009) 1565–1568. <https://doi.org/10.1016/j.corsci.2009.05.001>.

- [13] A. Boag, A.E. Hughes, A.M. Glenn, T.H. Muster, D. McCulloch, Corrosion of AA2024-T3 Part I: localised corrosion of isolated IM particles, *Corros. Sci.* 53 (2011) 17–26. <https://doi.org/10.1016/j.corsci.2010.09.009>.
- [14] A. E. Hughes, A. Boag, A. M. Glenn, D. McCulloch, T. J. Muster, C. Ryan, C. Luo, X. Zhou, G. E. Thompson, Corrosion of AA2024-T3 Part II: Co-operative corrosion. *Corros. Sci.* 53 (2011) 27–39. <https://doi.org/10.1016/j.corsci.2010.09.030>.
- [15] A. M. Glenn, T. H. Muster, C. Luo, X. Zhou, G. E. Thompson, A. Boag, A. E. Hughes, Corrosion of AA2024-T3 Part III: Propagation. *Corros. Sci.* 53 (2011) 40–50. <https://doi.org/10.1016/j.corsci.2010.09.035>.
- [16] A. Merstallinger, M. Sales, E. Semerad, B. D. Dunn, Assessment of Cold Welding Between Seperable Contact Surfaces Due to Impact and Fretting Under Vacuum. European Space Agency (2009). [http://esmat.esa.int/Publications/Published\\_papers/STM-279.pdf](http://esmat.esa.int/Publications/Published_papers/STM-279.pdf).
- [17] A. de Rooij, Corrosion in Space. European Space Agency. [http://esmat.esa.int/publications/published\\_papers/corrosion\\_in\\_space.pdf](http://esmat.esa.int/publications/published_papers/corrosion_in_space.pdf) (last accessed 15.02.2022).
- [18] K. K. de Groh, B. A. Banks, J. A. Dever, D. A. Jaworske, S. K. Miller, E. A. Sechkar, S. R. Panko, NASA Glenn Research Center’s Materials International Space Station Experiments (MISSE 1–7). NASA/TM–2008-215482. NASA Glenn Research Center’s Materials International Space Station Experiments (MISSE 1-7) - NASA Technical Reports Server (NTRS): Microsoft Word - E-16690TM.doc (nasa.gov) (last accessed 07.03.2022).
- [19] D. R. Gabe, Hard anodizing – what do we mean by hard? *Metal Finishing* 100 (2002) 52–58. [https://doi.org/10.1016/S0026-0576\(02\)80936-9](https://doi.org/10.1016/S0026-0576(02)80936-9).
- [20] A. D. Juhl, Overview of anodizing in the aerospace industry. *Metal Finishing* 108 (2010) 20–21. [https://doi.org/10.1016/S0026-0576\(10\)00011-5](https://doi.org/10.1016/S0026-0576(10)00011-5).
- [21] S. Shresta, B. D. Dunn, Advanced plasma electrolytic oxidation treatment for protection of light weight materials and structures in a space environment. *Advanced Surface Treatment*. European Space Agency. [http://esmat.esa.int/Publications/Published\\_papers/Keronite2007paper.pdf](http://esmat.esa.int/Publications/Published_papers/Keronite2007paper.pdf) (last accessed 15.02.2022).
- [22] M. Ritala, M. Leskelä, Atomic layer deposition. *Handbook of Thin Films 1* (2002) 103–159. <https://pubs.acs.org/doi/10.1016/B978-012512908-4/50005-9>.
- [23] J. Aarik, A. Aidla, H. Mändar, T. Uustare, Atomic layer deposition of titanium dioxide from TiCl<sub>4</sub> and H<sub>2</sub>O: investigation of growth mechanism. *App. Surf. Sci.* 172 (2001) 148–158. [https://doi.org/10.1016/S0169-4332\(00\)00842-4](https://doi.org/10.1016/S0169-4332(00)00842-4).
- [24] L. Aarik, T. Arroval, R. Rammula, H. Mändar, V. Sammelselg, J. Aarik, Atomic layer deposition of TiO<sub>2</sub> from TiCl<sub>4</sub> and O<sub>3</sub>. *Thin Solid Films* 542 (2013) 100–107. <https://doi.org/10.1016/j.tsf.2013.06.074>.
- [25] Restrictions on the use of hexavalent chromium compounds. [https://ec.europa.eu/environment/topics/waste-and-recycling/rohs-directive\\_en](https://ec.europa.eu/environment/topics/waste-and-recycling/rohs-directive_en).
- [26] MIL-DTL-5541 specification, chemical conversion coatings that form protective coatings by chemical reaction with aluminum and aluminum alloys.
- [27] E. Marin, A. Lanzutti, F. Andreatta, M. Lekka, L. Guzman, L. Fedrizzi, Atomic layer deposition: state-of-the-art and research/industrial perspectives. *Corros. Rev.* 29 (2011) 191–208. <https://doi.org/10.1515/CORRREV.2011.010>.
- [28] S.E. Potts, L. Schmalz, M. Fenker, B. Díaz, J. Światowska, V. Maurice, A. Seyeux, P. Marcus, G. Radnóczy, L. Tóth, W.M.M. Kessels, Ultra-Thin Aluminum Oxide Films Deposited by Plasma-Enhanced Atomic Layer Deposition for Corrosion Protection. *J. Electrochem. Soc.* 158 (2011) C132–C138. <https://iopscience.iop.org/article/10.1149/1.3560197>.

- [29] X. Du, K. Zhang, K. Holland, T. Tomblor, M. Moskovits, Chemical corrosion protection of optical components using atomic layer deposition. *Appl. Opt.* 48 (2009) 6470. <https://doi.org/10.1364/AO.48.006470>.
- [30] S. Mirhashemihaghighi, J. Światowska, V. Maurice, A. Seyeux, S. Zanna, E. Salmi, M. Ritala, P. Marcus, Corrosion protection of aluminum by ultra-thin atomic layer deposited alumina coatings. *Corrosion Science* 106, (2016) 16–24. <https://doi.org/10.1016/j.corsci.2016.01.021>.
- [31] R. Matero, M. Ritala, M. Leskelä, T. Salo, J. Aromaa, O. Forsen, Atomic layer deposited thin films for corrosion protection. *J. Phys. IV France* 9 (1999) 493–499. <https://doi.org/10.1051/jp4:1999862>.
- [32] C. X. Shan, X. Hou, K.L. Choy, Corrosion resistance of TiO<sub>2</sub> films grown on stainless steel by atomic layer deposition. *Surf. Coat. Technol.* 202 (2008) 2399–2402. <https://doi.org/10.1016/j.surfcoat.2007.08.066>.
- [33] E. Marin, L. Guzman, A. Lanzutti, L. Fedrizzi, M. Saikkonen, Chemical and electrochemical characterization of hybrid PVD + ALD hard coatings on tool steel. *Electrochem. Commun.* 10 (2009) 2060–2063. <https://doi.org/10.1016/j.elecom.2009.08.052>.
- [34] B. Díaz, E. Härkönen, V. Maurice, J. Światowska, A. Seyeux, M. Ritala, P. Marcus, Failure mechanism of thin Al<sub>2</sub>O<sub>3</sub> coatings grown by atomic layer deposition for corrosion protection of carbon steel. *Electrochim. Acta* 56 (2011) 9609–9618. <https://doi.org/10.1016/j.electacta.2011.07.104>.
- [35] B. Díaz, E. Härkönen, J. Światowska, V. Maurice, A. Seyeux, P. Marcus, M. Ritala, Lowtemperature atomic layer deposition of Al<sub>2</sub>O<sub>3</sub> thin coatings for corrosion protection of steel: Surface and electrochemical analysis. *Corros. Sci.* 53 (2011) 2168. <https://doi.org/10.1016/j.corsci.2011.02.036>.
- [36] E. Marin, L. Guzman, A. Lanzutti, W. Ensinger, L. Fedrizzi, Multilayer Al<sub>2</sub>O<sub>3</sub>/TiO<sub>2</sub> atomic layer deposition coatings for the corrosion protection of stainless steel. *Thin Solid Films* 522 (2012) 283–288. <https://doi.org/10.1016/j.tsf.2012.08.023>.
- [37] L. Aarik, J. Kozlova, H. Mändar, V. Sammelselg, J. Aarik, Chemical resistance and anticorrosion properties of atomic layer deposited TiO<sub>2</sub> and Al<sub>2</sub>O<sub>3</sub>. *Materials Chemistry and Physics* 228 (2019) 285–292. <https://doi.org/10.1016/j.matchemphys.2019.02.053>.
- [38] M. L. Chang, L. C. Wang, H. C. Lin, M. J. Chen, K. M. Lin, Investigation of defects in ultra-thin Al<sub>2</sub>O<sub>3</sub> films deposited on pure copper by the atomic layer deposition technique. *Applied Surface Science* 359 (2015) 533–542. <https://doi.org/10.1016/j.apsusc.2015.10.144>.
- [39] L. Paussa, L. Guzman, E. Marin, N. Isomaki, L. Fedrizzi, Protection of silver surfaces against tarnishing by means of alumina/titania-nanolayers. *Surf. Coat. Technol.* 206 (2011) 976–980. <https://doi.org/10.1016/j.surfcoat.2011.03.101>.
- [40] V. Sammelselg, I. Netšipailo, A. Aidla, A. Tarre, L. Aarik, J. Asari, P. Ritslaid, J. Aarik, Chemical resistance of thin film materials based on metal oxides grown by atomic layer deposition. *Thin Solid Films* 542 (2013) 219–224. <https://doi.org/10.1016/j.tsf.2013.06.079>.
- [41] I. Kolev, P. Peeters, R. Tap, B. Haag, Y. Musayev, S. Kursawe, T. M. Hosenfeldt, J. Gierl, J. Kostamo, A coated article of martensitic steel and a method of forming a coated article on steel. Patent application priority date: Feb. 15<sup>th</sup> 2012. European patent: EP2628817B1, 2012; USA patent: US9115426B2, 2012; Japan patent: JP6084032B2, 2012; China patent: CN103252938B, 2012.

- [42] J. R. Davis (Ed), *Corrosion: Understanding the Basics* (#6691G). Davis & Associates. ASM International (2009) 438–478.
- [43] Low Earth Orbit Facility (LEOX). [https://www.esa.int/Enabling\\_Support/Space\\_Engineering\\_Technology/Atomic\\_oxygen\\_generator\\_simulates\\_fire\\_in\\_the\\_sky](https://www.esa.int/Enabling_Support/Space_Engineering_Technology/Atomic_oxygen_generator_simulates_fire_in_the_sky) (last visited 26.04.2022).
- [44] P. Zoltowski, On the electrical capacitance of interfaces exhibiting constant phase element behavior, *J. Electroanal. Chem.* 443 (1998) 149–154. [http://dx.doi.org/10.1016/S0022-0728\(97\)00490-7](http://dx.doi.org/10.1016/S0022-0728(97)00490-7).
- [45] P. E. Flewitt, R. K. Wild, *Physical methods for materials characterization. 2-nd edition*. Institute of Physics Publishing: Bristol and Philadelphia, 2003.
- [46] P. J. Goodhew, J. Humphreys, R. Beanland, *Electron Microscopy and Analysis, Third Edition*. Taylor and Francis: London and New York, 2001, 251 PP.
- [47] M. L. B. Palacio, B. Bhushan. Depth-sensing indentation of nanomaterials and nanostructures. *Materials Characterization* 78 (2003) 1–20. <https://doi.org/10.1016/j.matchar.2013.01.009>.
- [48] Keysight Technologies Data Sheet (2014). Continuous Stiffness Measurement (CSM) Option (2014). <https://www.keysight.com/us/en/assets/7018-02197/data-sheets>.
- [49] J. Mencik, Uncertainties and Errors in Nanoindentation. Nanoindentation in Materials Science. *InTech 2012*. <http://dx.doi.org/10.5772/50002>.
- [50] V. Sammelselg, L. Aarik, M. Merisalu, world patent application: WO 2014102758 A1, priority date: Dec. 31<sup>st</sup> 2012; European patent: EP 2 938 758 B1, 2016; USA patent: US 9,834,849 B2, 2017; Japan patent: JP 63336477 B2, 2018.
- [51] M. Merisalu, L. Aarik, J. Kozlova, H. Mändar, A. Tarre, V. Sammelselg, Effective corrosion protection of aluminum alloy AA2024-T3 with novel thin nanostructured oxide coating. *Surface and Coatings Technology* 411 (2021) 126993. <https://doi.org/10.1016/j.surfcoat.2021.126993>.
- [52] M. Merisalu, L. Aarik, J. Kozlova, H. Mändar, A. Tarre, H. M. Piirsoo, V. Sammelselg, Al alloy protection via ultra-thin ceramic coatings and different surface pre-treatments. *Surface & Coatings Technology* 435 (2022) 128240. <https://doi.org/10.1016/j.surfcoat.2022.128240>.
- [53] M. Merisalu, L. Aarik, H. M. Piirsoo, J. Kozlova, A. Tarre, R. Zabels, J. Wessing, A. Brieva, V. Sammelselg, Nanostructured Coating for Aluminum Alloys Used in Aerospace Applications. *Journal of The Electrochemical Society* 169 (2022) 071503. <https://iopscience.iop.org/article/10.1149/1945-7111/ac7bb2>.
- [54] J. Aarik, A. Aidla, A. Kasikov, H. Mändar, R. Rammula, V. Sammelselg, Influence of carrier gas pressure and flow rate on atomic layer deposition of HfO<sub>2</sub> and ZrO<sub>2</sub> thin films. *App. Surf. Sci.* 252 (2006) 5723–5734. <https://doi.org/10.1016/j.apsusc.2005.07.067>.
- [55] T. Jõgiaas, Roberts Zabels, Aivar Tarre, Aile Tamm, Hardness and modulus of elasticity of atomic layer deposited Al<sub>2</sub>O<sub>3</sub>-ZrO<sub>2</sub> nanolaminates and mixtures. *Mat. Chem. And Phys.* 240 (2020) 122270. <https://doi.org/10.1016/j.matchemphys.2019.122270>.
- [56] R. Ali, M. R. Saleem, P. Pääkkönen, S. Honkanen, Thermo-Optical Properties of Thin Film TiO<sub>2</sub>-Al<sub>2</sub>O<sub>3</sub> Bilayers Fabricated by Atomic Layer Deposition. *Nanomaterials* 5 (2015) 792–803. <https://doi.org/10.3390/nano5020792>.
- [57] V. Sammelselg, J. Aarik, A. Kasikov, E. Heikinheimo, M. Peussa, L. Niinisto, Composition and thickness determination of thin oxide films: comparison of different programs and methods. *Journal of Analytical Atomic Spectrometry*, 14 (3) (1999), 523–527. <https://pubs.rsc.org/en/content/articlelanding/1999/JA/a806762g>.

- [58] V. Sammelselg, E. Rauhala, K. Arstila, A. Zakharov, J. Aarik, A. Kikas, J. Karlis, A. Tarre, A. Seppala, J. Asari, I. Martinson, Study of thin oxide films by electron, ion and synchrotron radiation beams. *Mikrochimica Acta* 139 (2002) 165–169. <https://link.springer.com/article/10.1007/s006040200056>.
- [59] M. Curioni, T. Gionfini, A. Vincenzo, P. Skeldon, G. E. Thompson, Optimization of anodizing cycles for enhanced performance. *Surface and Interface Analysis* 45 (2013). <https://onlinelibrary.wiley.com/doi/10.1002/sia.5222>.
- [60] N. Du, S. Wang, Q. Zhao, Z. Shao, Effects of boric acid on microstructure and corrosion resistance of boric/sulphuric acid anodic film on 7050 aluminum alloy. *Trans. Nonferrous. Met. Soc. China* 22 (2012) 1655–1660. [https://doi.org/10.1016/S1003-6326\(11\)61369-1](https://doi.org/10.1016/S1003-6326(11)61369-1).
- [61] L. Zhang, G. E. Thompson, M. Curioni, P. Skeldon, Anodizing in Sulfuric Acid/Boric Acid Mixed Electrolyte. *J. Electrochem. Soc.* 160 (2013) C179–C184. <https://iopscience.iop.org/article/10.1149/2.032306jes>.
- [62] Rust Stop paint. <https://www.motipdupli.com/en/products/dupli-color/rust-protection/rust-stop/ipg-1270/tm-1270.html> (last visited 09.05.2022).
- [63] Chemical Composition of Highlighter Colours. <https://www.compoundchem.com/2015/01/22/highlighters/> (last visited 09.05.2022).

## **PUBLICATIONS**



## CURRICULUM VITAE

Name:	Maido Merisalu		
Date of birth:	06.08.1984		
Citizenship:	Citizen of Estonian Republic		
Address:	Institute of Physics, University of Tartu, W. Ostwaldi 1, 50411 Tartu, Estonia		
Telephone:	+372 5559 7617		
E-mail address:	maido.merisalu@ut.ee		
Education:	2012–2022 University of Tartu, PhD student, materials science 2009–2011 University of Tartu, Master degree in materials science 2006–2009 University of Tartu, Bachelor degree in materials science		
Work:	2022	Captain Corrosion Consortium, Captain Corrosion OÜ	President
	2021–2022	Murrifier OÜ, University of Tartu spin-off company	Board member
	2019	Industrial Property Board of Appeal	Expert Member
	2016–2022	Captain Corrosion OÜ, University of Tartu spin-off company	Chief Executive Officer
	2012	University of Tartu, Institute of Physics, Laboratory of Thin Film Technology	Engineer
	2010–2011	Eesti Nanotehnoloogiate Arenduskeskuse AS	Laboratory assistant
Languages:	Estonian, native; English, good		
Science	H-Index:	19	
	Total Publications:	46	
	<a href="https://www.webofscience.com/wos/author/record/25602972">https://www.webofscience.com/wos/author/record/25602972</a>		

Intellectual Property	2021	Utility model	Ozone-based disinfection system
	2020	Patent pending	Corrosion monitoring system
	2012	Patent	Method of preparing corrosion resistant coatings
Awards and recognition	2019	Top 10 young entrepreneur. Estonian Chamber of Commerce and Industry, Swedbank	
	2018	Nominated for national science award in Estonia along with other scientists (Jaan Aarik, Väino Sammelselg, Lauri Aarik, Jekaterina Kozlova) from the Laboratory of Thin Film Technology	
	2018	Prototron Autumn 2018 Winner (Captain Corrosion OÜ). Received funding to develop a corrosion monitoring system	
	2017	National university lecturer laureate of the year in Estonia	
	2016	Tartu Raefond Award for best worker at the University of Tartu	
	2016	Garage 48 Spacetech 2016 first place. Leader of team "Spaceprot Technologies"	
	2015	Tartu Raefond Award for best worker at the University of Tartu	
	2015	Award for best collaboration project between the University of Tartu and an Estonian company at the conference "Õigel ajal õiges kohas"	

## ELULOOKIRJELDUS

Nimi:	Maido Merisalu		
Sünniaeg:	06.08.1984		
Kodakondsus:	Eesti Vabariigi kodanik		
Kontaktandmed:	Füüsika Instituut, Tartu Ülikool, W. Ostwaldi 1, 50411 Tartu, Eesti		
Telefon:	+372 5559 7617		
E-post:	maido.merisalu@ut.ee		
Haridus:	2012–2022 Tartu Ülikool, doktoriõpe, materjaliteadus 2009–2011 Tartu Ülikool, magistrikraad, materjaliteadus 2006–2009 Tartu Ülikool, bakalaureusekraad, materjaliteadus		
Töökogemus:	2022	Captain Corrosion Konsortsium, Captain Corrosion OÜ	President
	2021–2022	Murrifier OÜ, Tartu Ülikooli hargettevõtte	Juhatuse liige
	2019	Tööstusomandi appellatsioonikomisjon	Täiendav liige
	2016	Captain Corrosion OÜ, Tartu Ülikooli hargettevõtte	Juhataja
	2012	University of Tartu, Füüsika Instituut, kiletehnoloogia labor	Insener
	2010–2011	Eesti Nanotehnoloogiate Arenduskeskuse AS	Laborant
Keelteoskus:	Eesti keel, emakeel; inglise, hea		
Teadus	H-indeks:	19	
	Publikatsioonide arv:	46	
	<a href="https://www.webofscience.com/wos/author/record/25602972">https://www.webofscience.com/wos/author/record/25602972</a>		
Intellektuaal- omand	2021	Kasulik mudel	Osoonil põhinev desinfitseerimisseade
	2020	Patendi taotlus	Korrosiooni monitoorimise süsteem

	2012	Patent	Meetod kaitsekatete valmistamiseks
Tunnustused ja preemiad	2019	Top 10 noor ettevõtja. Eesti Kaubandus- ja Tööstuskoda, Swedbank	
	2018	Riikliku teaduspreemia nominent koos kolleegidega Tartu Ülikooli füüsika instituudi kiletehnoloogia laborist (Jaan Aarik, Väino Sammelseg, Lauri Aarik, Jekaterina Kozlova)	
	2018	Prototroni sügisvooru 2018 võitja (Captain Corrosion OÜ). Rahastati korrosioonisensorite arendust	
	2017	Aasta õppejõu laureaat, Haridus- ja Teadusministeerium	
	2016	Tartu Raefondi preemia parimale Tartu Ülikooli töötajale	
	2016	Garage 48 Spacetech 2016 esimene koht. Meeskonna "Spaceprot Technologies" juht	
	2015	Tartu Raefondi preemia parimale Tartu Ülikooli töötajale	
	2015	Preemia parima Tartu Ülikooli ja ettevõtte vahelise koostööprojekti eest konverentsil "Õigel ajal õiges kohas"	

## DISSERTATIONES SCIENTIAE MATERIALIS UNIVERSITATIS TARTUENSIS

1. **Martin Järvekülg.** Tubular microstructures by Hf-, Zr- and Ti-butoxide gel sheet rolling. Tartu, 2011, 112 p.
2. **Sergei Vlassov.** Investigation of nanoscale interactions and mechanical properties of nanostructures using quartz tuning fork based real-time measurements. Tartu, 2011, 171 p.
3. **Margus Kodu.** Pulsed Laser Deposition of Magnesium Oxide and Barium Ternary Oxides for Plasma Display Protective Layers. Tartu, 2011, 89 p.
4. **Rainer Pärna.** Surface studies of some oxide films. Tartu, 2011, 129 p.
5. **Jevgeni Šulga.** Self-assembly and interaction of nanostructures. Tartu, 2011, 114 p.
6. **Wojciech Kuznik.** Quantum-chemical computer simulations of the linear and non-linear optical properties of pyrazoloquinoline and dicyanopyrazine derivatives. Tartu, 2012, 89 p.
7. **Leonid Dorogin.** Structural and tribological properties of zero- and one-dimensional nanocrystals. Tartu, 2012, 193 p.
8. **Viljar Palmre.** Fabrication and characterization of microporous carbon-based electroactive polymer actuators. Tartu, 2012, 99 p.
9. **Madis Paalo.** Synthesis of CNT-metal oxide nanocomposites: sol-gel process, rheology, structural and functional properties. Tartu, 2014, 175 p.
10. **Raul Välbe.** Development of ionic liquid composites by sol-gel method for elaboration of industrial nano- and microstructures. Tartu, 2014, 97 p.
11. **Urmas Joost.** Impurity and preparation dependent properties of titania thin films. Tartu, 2014, 155 p.
12. **Madis Umalas.** Application of sol-gel technology for production of ceramic nanocomposites and functional coatings. Tartu, 2015, 136 p.
13. **Elena Samsonova.** Energy transfer probe as a tool to study morphological and structural origins of fluorescence quenching in rare-earth doped nanophosphors. Tartu, 2015, 114 p.
14. **Jay Mondal.** Novel Corrosion Protective Nanostructured Composite Coatings. Tartu, 2016, 104 p.
15. **Kathriin Utt.** Metal oxide mesostructures for optical applications. Tartu, 2016, 88 p.
16. **Kaido Siimon.** Electrospun gelatin cross-linked by glucose. Tartu, 2016, 84 p.
17. **Marko Part.** Combined three-dimensional sol-gel structures and atomic layer deposited thin films. Tartu, 2017, 162 p.
18. **Pejman Rasti.** Analysis of Remote Sensing Image Super Resolution using Fluid Lenses. Tartu, 2017, 188 p.
19. **Ivo Romet.** Recombination luminescence of doped borates: origin and application prospects in dosimetry. Tartu, 2017, 111 p.

20. **Vladimir I. Kondratiev.** Processing and characterization of transparent electrode materials. Tartu, 2017, 111 p.
21. **Taivo Jõgiaas.** Mechanical properties of atomic layer deposited thin films and nanocomposites. Tartu, 2017, 125 p.
22. **Lauri Aarik.** Atomic layer deposition and characterization of thin oxide films for application in protective coatings. Tartu, 2017, 180 p.
23. **Triin Kangur.** Preparation and functional properties of stochastic microstructured sol-gel silica materials. Tartu, 2018, 96 p.
24. **Marta Berholts.** Fragmentation of ionic and hydrogen-bonded molecules induced by synchrotron radiation. Tartu, 2018, 126 p.
25. **Priit Priimägi.** Development and optimization of 3D-microbatteries. Tartu, 2018, 118 p.
26. **Siim Hödemann.** Residual stress determination in chemically strengthened and thermally tempered glass plates using scattered light method. Tartu, 2019, 146 p.
27. **Jekaterina Kozlova.** Complex characterization of graphene structures on nanometer level. Tartu, 2019, 206 p.
28. **Kristjan Kalam.** Magnetic, electric and structural properties of atomic layer deposited zirconia-based nanolaminates and mixtures. Tartu, 2020, 94 p.
29. **Triinu Vihmann.** Ionic liquids: synthesis and application in lubrication and lithography. Tartu, 2020, 102 p.
30. **Helina Seemen.** Atomic layer deposition and microscopic analysis of magnetically and electrically polarizable thin solid films. Tartu, 2021, 126 p.
31. **Ekaterina Vagapova.** Fluorescence quenching in inorganic crystalline solids activated by neodymium ions; from bulk to micro- and nanocrystals. Tartu, 2021, 116 p.
32. **Evgenii Strugovshchikov.** First-principles studies on rare-earth metal-hydride-based smart materials. Tartu, 2021, 166 p.